UNIVERSITÀ
DEGLI STUDI
FIRENZE

2D Forward Looking SONAR in Navigation Aiding: Development and Testing of Strategies for Autonomous Underwater Vehicles

A dissertation submitted in partial fulfillment of the requirements for the Degree of Doctor of Philosophy in

INDUSTRIAL ENGINEERING
Scientific Disciplinary Sector ING-IND/13

Candidate
Matteo Franchi

Advisor
Prof. Benedetto Allotta

Co-advisor
Dr. Alessandro Ridolfi

Coordinator
Prof. Maurizio De Lucia

Department of Industrial Engineering
University of Florence
Florence, Italy

XXXII Ph.D. Cycle - Years 2016/2019

To my family

Abstract

This work collects the results of the research activity on marine robotics carried out at the Mechatronics and Dynamic Modeling Laboratory (MDM Lab) of the Department of Industrial Engineering of the University of Florence (UNIFI DIEF) during the years 2014-2017. Reliable navigation systems are fundamental for Autonomous Underwater Vehicles (AUVs) to perform complex tasks and missions. It is well known that the Global Positioning System (GPS) cannot be employed in underwater scenarios; thus, during missions below the sea's surface the real-time position is usually obtained with expensive sensors, such as the Doppler Velocity Log (DVL), integrated within a navigation filter such as an Extended Kalman Filter (EKF), Unscented Kalman Filter (UKF), or Dead Reckoning (DR) strategies. The main goal of this work is to develop and test a framework able to integrate a Forward-Looking SONAR (FLS), by means of linear speed estimations, into an underwater navigation system. On the one hand, the proposed solution can work together with a standard navigation sensors set (comprising, for example, a DVL), and thus leading to a greater number of linear speed measurements. On the other hand, employing an FLS to aid navigation could potentially outline other advantages. Using an augmented set of devices able to provide navigation information represents an intrinsic boost in redundancy; DVL-denied scenarios, such as very close to the seafloor or other surfaces or when a substantial number of gaseous bubbles is present, could be managed. Indeed, as opposed to the DVL, the FLS possesses much more beams that are spread into a broader area, thus improving reliability. DVL failings in the presence of bubbles are well-documented in the current literature and have been experienced during several tests at sea performed by UNIFI DIEF.

Conversely, the presence of bubbles, which can be noticed within FLS images as strong return echoes spots, is usually tolerable and not capable of jeopardizing FLS operations.

Moreover, although bigger AUVs enable the use of more sophisticated instrumentation and can carry a heavy payload, smaller AUVs are constrained to limited payload carrying capabilities. Hence, in addition to constituting a valuable research interest, multitasking onboard sensors represent a solution

that offers compactness and avoids the use of some instruments.
Besides this, to better the dynamic modeling of the AUV, a light-weight online estimator for the longitudinal dynamics and a more realistic propulsion model are developed. Lastly, an Adaptive Unscented Kalman Filter (AUKF)-based navigation solution is proposed.
Offline validation, through the use of navigation data obtained during sea trials undertaken in La Spezia (Italy) at the NATO STO Centre for Maritime Research and Experimentation (CMRE), is presented. Afterward the results of real autonomous underwater missions performed in La Spezia (Italy) within the activities of the SEALab, the joint research laboratory between the Naval Experimentation and Support Center (Centro di Supporto e Sperimentazione Navale) (CSSN) of the Italian Navy and the Interuniversity Center of Integrated Systems for the Marine Environment (ISME), and at Vulcano Island, Messina (Italy) are reported.

Acknowledgments

First and foremost, I would like to thank my advisor, Prof. Benedetto Allotta, which allowed me to work in the field of robotics for three years, making a long-lasting wish come true. These very few lines will never be enough to express my gratitude. Special thanks go to my co-advisor, Dr. Alessandro Ridolfi; he has been supportive since the days I began working in the Mechatronics and Dynamic Modeling Laboratory of the Department of Industrial Engineering of the University of Florence.

A special acknowledgment goes to my colleagues, which eventually have become friends. I have spent only a little time with some of them, while others have mentored me throughout this whole journey, being an inspiration in many ways.

For their loyalty, I am grateful to my lifetime friends; times may change, but the trust I have in them will always be the same.

I want to thank all my family; their support and love, during the highs and lows of these years, has been unconditional and total. My aunts, uncles, and cousins who have always been proud of my "Ph.D. choice". I am especially grateful to my parents, who have been taking care of me emotionally and financially. I have always known that you believe in me and want the best for me; without their support, this journey would not have been possible.

Last but not least, I would like to thank Sara; she has encouraged me and loved from the beginning of this journey, tolerating the frustration of failed attempts and celebrating my achievements. We have grown together during these three years; she has always been by my side, and this journey would not have been the same without her.

To all the people mentioned here goes my sincere gratitude, for they have contributed to shaping the person I am and the one that I want to be.

Matteo Franchi

2020

Contents

List of Figures

List of Tables

Acronyms

AHRS Attitude and Heading Reference System

AI Artificial Intelligence

AKF Adaptive Kalman Filter

ATR Automatic Target Recognition

AUKF Adaptive Unscented Kalman Filter

AUV Autonomous Underwater Vehicle

BA Bundle Adjustment

CB Center of Buoyancy

CFD Computational Fluid Dynamics

CG Center of Gravity

CKF Cubature Kalman Filter

CLAHE Contrast Limited Adaptive Histogram Equalization

DC Direct Current

DOF Degree of Freedom

DR Dead Reckoning

DS Depth Sensor

DVL Doppler Velocity Log

EKF Extended Kalman Filter

FLS Forward-Looking SONAR

FOG Fiber Optic Gyroscope

FOV Field Of View

FT Fourier Transform

GNSS Global Navigation Satellite System

GPS Global Positioning System

HW HardWare

IMU Inertial Measurement Unit

INS Inertial Navigation Systems

KF Kalman Filter

LBL Long BaseLine

LP Low Pass

LS Least Squares

MLBL Moving Long BaseLine

MLE Maximum Likelihood Estimation

MMAKF Multiple Model Adaptive Kalman Filter

MMSE Minimum Mean Square Error

MSIS Mechanically Scanned Imaging SONAR

NED North, East, Down

NIS Normalized Innovation Squared

OA Obstacle Avoidance

RLS Recursive Least Squares

ROV Remotely Underwater Vehicle

RPY Roll, Pitch and Yaw

RV Random Variable

SLAM Simultaneous Localization and Mapping

SNAME Society of Naval Architects and Marine Engineers

SONAR SOund NAvigation and Ranging

SSS SideScan SONAR

SVM Support Vector Machines

TM Template Matching

TUKF Transformed Unscented Kalman Filter

UKF Unscented Kalman Filter

USBL UltraShort BaseLine

UT Unscented Transform

UUV Unmanned Underwater Vehicle

Nomenclature

Measurement units for non-uniform quantities are not reported. A 1 in the units field denotes an unitless quantity.

A_{FS}	Body-fixed frame to FLS-fixed one homogeneous transformation matrix	
A_f	Frontal area of an underwater vehicle	m^2
B	The matrix that maps the thrusts carried out by the motors to the body-fixed vector of forces and torques	
B_1	The matrix that stores the unit vector of the motor directions	1
B_2	The matrix that stores the 3D distances of each motor from the body-fixed frame	m
$C(\boldsymbol{\nu})$	Centripetal and Coriolis effects matrix	
$C(m, n)$	Normalized cross-power spectrum in the Fourier domain	1
$C_a(\boldsymbol{\nu})$	Added centripetal and Coriolis effects matrix	
C_u	Drag coefficient along the surge axis	1
$D(\boldsymbol{\nu})$	Hydrodynamic damping effects matrix	
D_0	Cut-off frequency of the Butterworth LP filter for FLS images	pixel
$E(\boldsymbol{\lambda})$	Error metrics for surge drag estimator	N^2
$E[\bullet]$	Expectation operator	
$F_1(\boldsymbol{\nu})$	Surge-axis damping force (based on the quadratic damping model)	N

$H(m,n)$ Transfer function of the Butterworth LP filter for FLS images in the frequency domain 1

$I(m,n)$ Image in the Fourier domain 1

$I(m,n)_{t_i}$ Image in the Fourier domain at a certain instant time t_i 1

$J(\boldsymbol{\eta})$ Matrix that maps kinematic quantities from body-fixed frame to Earth-fixed one

K Body-fixed x-axis torque Nm

$K_{\dot{p}}, M_{\dot{q}}, N_{\dot{r}}$ The hydrodynamic added mass torque about the X, Y, Z axes, respectively and generated by an acceleration indicated in subscript Nm

$K_{p|p|}$ X-axis quadratic damping coefficient (torque) according to [Fossen et al., 1994] kg/s

L Kalman gain

M Body-fixed y-axis torque Nm

$M(m,n)$ Magnitude of the image spectrum in the Fourier domain 1

M_a Added mass matrix

M_m Mass and inertia matrix

$M_{q|q|}$ Y-axis quadratic damping coefficient (torque) according to [Fossen et al., 1994] kg/s

N Body-fixed z-axis torque Nm

N_{Q_w} Moving window size for process noise Q estimation

$N^{\star}_{Q_w}$ Matrix that takes into account the history of the past measurements in a certain window of size N_{Q_w}

N_{R_w} Moving window size for measurement noise R estimation

$N^{\star}_{R_w}$ Matrix that takes into account the history of the past measurements in a certain window N_{R_w}

$N_{r\|r\|}$	Z-axis quadratic damping coefficient (torque) according to [Fossen et al., 1994]	kg/s
P	State covariance	
Q	Process noise	
R^2	Coefficient of determination	1
R	Measurement noise	
$R_{\rightarrow_{MAX}}$	Maximum delivering range of the FLS	m
$R_{\rightarrow}$	Delivering range of the FLS	m
SS_{res}	Sum of squares of residuals	N^2
SS_{tot}	Total sum of squares	N^2
$T_b^N(\boldsymbol{\eta}_2)$	Euler matrix	1
V	Volume	m^3
$V_{a,i}$	Advance speed of the i-th motor	m/s
$Var[\bullet]$	Variance operator	
W	Magnetometer Soft Iron, Scale Factor, and Misalignment effect	1
$W_i^{(c)}$	The i-th weight to compute the variance in the Unscented Transform	
$W_i^{(m)}$	The i-th weight to compute the mean in the Unscented Transform	
X	Body-fixed x-axis force	N
$X_{\dot{u}}, Y_{\dot{v}}, Z_{\dot{w}}$	The hydrodynamic added mass force along the X, Y, Z axes, respectively and generated by the acceleration indicated in subscript	N
$X_{u\|u\|}$	X-axis axis quadratic damping coefficient (force) according to [Fossen et al., 1994]	kg/s
Y	Body-fixed y-axis force	N
$Y_{v\|v\|}$	Y-axis quadratic damping coefficient (force) according to [Fossen et al., 1994]	kg/s

Z	Body-fixed z-axis force	N
$Z_{w\|w\|}$	Z-axis quadratic damping coefficient (force) according to [Fossen et al., 1994]	kg/s
ΔT	Fixed sampling time of the filter	s
α	Elevation angle of the FLS	rad
β	Azimuth angle of the FLS	rad
$\boldsymbol{P}_{GPS}$	GPS fix	
$\boldsymbol{f}(\bullet)$	Nonlinear state function	
$\boldsymbol{h}(\bullet)$	Nonlinear measurement function	
$\boldsymbol{u}$	Control input vector	
$\boldsymbol{v}$	Measurement noise	
$\boldsymbol{w}$	Process noise	
$\boldsymbol{x}$	State vector	
$\boldsymbol{y}$	Measurements vector	
$\boldsymbol{g}_{\boldsymbol{\eta}}(\boldsymbol{\eta})$	Gravitational and buoyancy effects vector	
$\boldsymbol{I}_{yi}$	Column vector that takes into account the current number of available measurements	
$\boldsymbol{S}$	Retrieved translation motion of the FLS	m
$\boldsymbol{T}(\boldsymbol{\nu}, \boldsymbol{u})$	Vector of thrusts carried out by the motors of the vehicle	N
$\boldsymbol{\epsilon}_P$	GPS measurement noise	
$\boldsymbol{\epsilon}_a$	IMU measurement noise	m/s^2
$\boldsymbol{\epsilon}_g$	Gyroscope measurement noise	rad/s
$\boldsymbol{\epsilon}_m$	Magnetometer bias	T
$\boldsymbol{\epsilon}_{s1}$	FLS range and azimuth measurement noise	
$\boldsymbol{\epsilon}_v$	DVL measurement noise	m/s

$\boldsymbol{\eta}$	Earth-fixed pose	
$\boldsymbol{\eta}_1$	Earth-fixed position	m
$\boldsymbol{\eta}_2$	Earth-fixed orientation	rad
$\hat{\boldsymbol{u}}_{rpm}$	Vector that stores the reference rotational speeds of the motors	rad/s
$\boldsymbol{\mathcal{H}}_i$	i-th σ-points column propagated through the measurement function	
$\boldsymbol{\mathcal{X}}_i$	The i-th column of the matrix that collects all the σ-points	
$\boldsymbol{\mu}$	Innovation vector	
$\boldsymbol{\mu}_i^\star$	Innovation vector modified for the UKF adaptation at the instant i	
$\boldsymbol{\nu}$	Body-fixed velocity	
$\boldsymbol{\nu}_1$	Body-fixed linear velocity	m/s
$\boldsymbol{\nu}_2$	Body-fixed angular velocity	rad/s
$\boldsymbol{\tau}$	Body-fixed vector of forces and torques	
$\boldsymbol{\tau}(\boldsymbol{\nu}, \boldsymbol{u}_{rpm})$	The modeled action (forces and torques) on the vehicle	
$\boldsymbol{\tau}_1$	Body-fixed force	N
$\boldsymbol{\tau}_2$	Body-fixed torque	Nm
$\tilde{\boldsymbol{\epsilon}}_P$	Earth-fixed frame GPS measurement noise fix	m
$\boldsymbol{\upsilon}$	Residual vector	
$\boldsymbol{\upsilon}_i^\star$	Residual vector modified for the UKF adaptation at the instant i	
$\boldsymbol{b}_a$	IMU bias	m/s^2
$\boldsymbol{b}_g$	Gyroscope bias	rad/s
$\boldsymbol{b}_{s1}$	FLS range and azimuth bias	
$\boldsymbol{b}_v$	DVL bias	m/s
$\boldsymbol{s}$	Retrieved translation motion of the FLS	pixel
$\boldsymbol{u}_{rpm}$	Vector that stores the rotational speeds of the motors	rad/s

δ_{Lx}	Drag damping coefficient (linear damping model)	kg/s
δ_{Qx}	Drag damping coefficient (quadratic damping model)	kg/m
ϵ_f	FOG measurement noise	rad/s
ϵ_p	Pressure measurement noise	N/m^2
ϵd	DS measurement noise	m
η^k	Rate parameter for surge estimator at instant k	s^2/m
$\hat{u}_{rpm_i}$	Reference rotational speeds of the i-th motor	rad/s
$\wedge$	AND logical operator	1
$\left\{O^{FS}x^{FS}y^{FS}z^{FS}\right\}$	FLS -fixed reference frame	
$\left\{O^{N}x^{N}y^{N}z^{N}\right\}$	Earth-fixed reference frame	
$\left\{O^{b}x^{b}y^{b}z^{b}\right\}$	Body-fixed reference frame	
$\vee$	OR logical operator	1
$\mathcal{F}\{\bullet\}$	FT operator	
$\mathcal{O}$	Set of functions to investigate the observability rank condition	
$\mathcal{V}$	Voltage supply	Volt
$\mathcal{X}$	The matrix that collects all the σ-points	
$\mu_i^{j^\star}$	j-th row of the innovation vector modified for the UKF adaptation at the instant i	
$\text{diag}\{I_x, I_y, I_z\}$	Principal inertia matrix	kgm^2
$\overline{e}_k$	Average of the (current and past) navigation errors at the instant k between two underwater navigation algorithm	m
$\overline{\chi}^2_{\varsigma,\varrho}$	Acceptance threshold for the NIS test	1
$\overline{c(x,y)}$	Average value of the normalized cross-power spectrum	1
$\overline{c_r}$	The threshold value for the binary acceptance law of the phase-correlate algorithm	1

ϕ	Roll angle	rad
ψ	Yaw angle	rad
ρ	Water density	kg/m^3
τ_{1x}	Surge-axis modeled thrust action	N
θ	Pitch angle	rad
$\tilde{C}(\boldsymbol{\nu})$	Rigid body centripetal and Coriolis effects matrix	
$\tilde{M}_m$	Rigid body mass and inertia matrix	
$\tilde{\boldsymbol{\epsilon}}_{s1}$	FLS estimated velocity measurement noise	m/s
$\tilde{\boldsymbol{b}}_{s1}$	FLS estimated velocity bias	m/s
$\upsilon_i^{j\star}$	j-th row of the residual vector modified for the UKF adaptation at the instant i	
φ_χ	Measure of consistence of the NIS test	1
ϱ	NIS test reliability	1
ς	Deegres of freedom of the χ^2_ς distribution	1
${}^N R_b^N(\boldsymbol{\eta}_2)$	Earth-fixed frame to body-fixed frame rotation matrix	1
${}^N\boldsymbol{P}_{GPS}$	Earth-fixed frame GPS measured position	m
${}^N\boldsymbol{B}$	Fixed frame buoyancy force	N
${}^N\boldsymbol{H}$	Earth's magnetic field	T
${}^N\boldsymbol{W}$	Fixed frame gravitational force	N
${}^N d_{DS}$	DS measured depth	m
${}^b R_{FS}^b$	Body-fixed frame to FLS-fixed one rotation matrix	1
${}^b\boldsymbol{p_{FS}}$	Position of the FLS in the body-fixed frame	m
${}^b\boldsymbol{B}$	Body frame buoyancy force	N
${}^b\boldsymbol{W}$	Body frame gravitational force	N

${}^b\boldsymbol{\omega}_{IMU}$	Gyroscope measured rotational velocity	rad/s
${}^b\boldsymbol{a}_{IMU}$	IMU measured acceleration	m/s^2
${}^b\boldsymbol{v}_{DVL}$	DVL measured velocity	m/s
${}^b\boldsymbol{v}_{FLS}$	FLS estimated velocity	m/s
${}^b\mathbf{P}_{mi} \times {}^b\mathbf{n}_{mi}$	The arm of the i-th motor center with respect to the CG (expressed in the body-fixed frame)	m
${}^b\mathbf{P}_{mi}$	The center of the i-th motor center with respect to the CG (expressed in the body-fixed frame)	m
${}^b\mathbf{n}_{mi}$	The unit vector that represents the axis of the i-th motor (expressed in the body-fixed frame)	1
${}^mR_{\rightarrow}$	FLS measured range	m
${}^m\omega_{FOG}$	FOG measured rotational velocity	rad/s
b_e	FOG bias due to Earth's rotation	rad/s
b_f	FOG bias	rad/s
b_p	Pressure bias	N/m^2
$c(x, y)$	Normalized cross-power spectrum in the spatial domain	1
c_p	Peak of the normalized cross-power spectrum	1
c_r	Variable to state the acceptance of the registration with Forward-Looking SONAR (FLS) images	1
$d\mathcal{O}$	Coodistribution of $\mathcal{O}$	
e_k	Navigation error at the instant k between two underwater navigation algorithm	m
g	Gravitational acceleration	m/s^2
h	Maximum delivering range of the FLS expressed as number of rows	pixel
$i(x, y)$	Image in the spatial domain	1

$i(x,y)_{t_i}$	Image in the spatial domain at a certain time instant t_i	1
$i_{adding}(x,y)$	The adding applied to FLS images after the acoustic insonification pattern removal	1
$i_{mean}(x,y)$	The mean of of FLS images within a moving window	1
$i_{post}(x,y)$	The FLS image after the acoustic insonification pattern removal	1
$i_{pre}(x,y)$	The FLS image before the acoustic insonification pattern removal	1
k	Coefficient of the quadratic relation between motor thrust and motor rotational speed (bollard coefficient)	Ns^2/rad
k_{mean}	The coefficient to be multiplied with the acoustic insonification pattern of FLS images	1
l	Filter order of the Butterworth LP for FLS images	1
m	Dry mass of the vehicle	kg
p	Body-fixed x-axis angular velocity	rad/s
p_0	Initial measured pressure	N/m^2
p_{DS}	Measured pressure	N/m^2
p_p	Propeller pitch	m
q	Body-fixed y-axis angular velocity	rad/s
r	Body-fixed z-axis angular velocity	rad/s
t	Time	s
u_{rpm_i}	Rotational speed of the i-th motor	rad/s
u	Body-fixed x-axis linear velocity	m/s
u^-_{rpm}	Lower boundary for the dead-zone of the motor	rad/s
u^-_{rpm}	Upper boundary for the dead-zone of the motor	rad/s
v	Body-fixed y-axis linear velocity	m/s

w	Body-fixed z-axis linear velocity	m/s
x	Earth-fixed x-axis position	m
y	Earth-fixed y-axis position	m
z	Earth-fixed z-axis position	m
${}^{m}\alpha$	FLS measurement azimuth	rad

Chapter 1

Introduction

The vast majority of the Earth's surface is covered by water. From geology to exploration and surveillance of archaeological sites and from Oil & Gas (O&G) industry to reconnaissance for military purposes, exploring and understanding seas and oceans is a matter of the primary importance. Because of their human's hostile nature, since the 1960s, seas and oceans have been explored with the aiding of robots.
Historically, immediately, reducing if not avoiding risks to human lives has been a particularly sensed subject, paving the way towards unmanned robots. The first Unmanned Underwater Vehicles (UUVs) were teleoperated ones and are referred in the technical literature as Remotely Underwater Vehicles (ROVs). A cable, usually called *umbilical cable*, acts as a constant connection providing power and communications, and specific operators are thus able to control the vehicle using the feedback forwarded by the onboard sensors. On the one hand, ROVs can be operated over a long time, enabling long-term missions. On the other hand, both costs and infrastructure demands are high. Therefore, considerable efforts and resources have been spent in the last decades in order to provide a certain autonomy to UUVs. Both to reduce operational costs and enhance the vehicle's motion limitations, the objective was to reduce human intervention.
Historically born to satisfy military requests, Autonomous Underwater Vehicles (AUVs) (Autonomous Underwater Vehicles) have gained interest with respect to ROVs during the years. Nowadays, many applications involve the use of such vehicles: O&G industries, marine biology, archaeology, and geology are just a few examples of current applications.

The development of AUVs has presented (and presents) several challenges. Arguably, one of the most significant is to retrieve the vehicle's position within the surrounding environment, making use of precise and reliable navigation and localization systems, which are necessary regardless of the kind of mission or task the underwater vehicle is required to perform. In addition to this, *perceptual* devices (such as optical cameras and SOund NAvigation and Rangings (SONARs)) able to sense the surrounding environment have been earning attention throughout the last decades; Automatic Target Recognition (ATR), mapping, Obstacle Avoidance (OA) are the main subjects that have been tackled. Afterward, the use of this equipment to aid navigation has emerged as a relevant alternative, but in the world of *perceptual* devices, the contribution of SONARs and especially FLSs (Forward-Looking Sonars) is less common.
As a consequence, the research activity carried out during the Ph.D. period aimed at pushing forward the use of FLSs in underwater navigation-aiding, developing, and validating a novel solution tailored to the underwater environment.
The remainder of this chapter is organized as follows: Section 1.1 concerns the framework in which the research activity was conducted. Since this thesis represents an intersection between underwater navigation and localization and acoustic payload (especially FLSs), a separate literature review is proposed. In particular, a discussion about the former is presented in Section 1.2, whereas FLS images and their applications to navigation-aiding are described in Section 1.3. Section 1.4 treats the main contributions and motivations that have steered this research activity. Lastly, Section 1.5 illustrates the structure of the thesis.

1.1 Overall framework

The research activity described in this work was conducted at the Mechatronics and Dynamic Modeling Laboratory (MDM Lab) of the Department of Industrial Engineering of the University of Florence (UNIFI DIEF). Thanks to the participation in the Tuscany-funded project TecnicHe per l'Esplorazione Sottomarina Archeologica mediante l'Utilizzo di Robot aUtonomi in Sciami (THESAURUS), the MDM Lab has been active in the underwater robotics fields since 2010 [THESAURUS, 2019].

Figure 1.1: The logo of the THESAURUS project [THESAURUS, 2019].

The creation of a swarm of AUVs to perform cooperative autonomous surveys of areas, where archaeological interest is high in the Tuscan Archipelago, was one of the targets of the above-mentioned project. The identification and geolocalization of potential objects of interest were meant to be performed with acoustical and optical payload. In addition to this, in order to create an underwater communication network for planning, monitoring and cooperation purposes, the AUVs of the swarm would be able to exchange information acoustically, both among themselves and with possible fixed stations. For the project sake, the Typhoon class AUVs was built by MDM Lab (for further information, the interested reader can refer to [Allotta et al., 2013]).
Afterwards, just before the end of the THESAURUS project (that was deemed successfully concluded in 2013), the MDM Lab assumed the role of coordinating partner of the European FP7 project ARcheological RObot systems for the Worlds Seas (ARROWS) [ARROWS, 2019].

Figure 1.2: The logo of the ARROWS project [ARROWS, 2019].

The main goal of the ARROWS project was the development of underwater vehicles able to offer safe and reliable undersea archaeological operations at the expense of a reduced cost. During the course of the project, the needs of underwater archaeologists acted as guidelines, leading to the development of mutable robotic tools with the ability to adapt themselves in response to the always different necessities of an archaeological campaign. The final product was a modular AUV named MArine Robotic Tool for Archaeology (MARTA), and more information can be found in [Allotta et al., 2014] and [Allotta et al., 2015b].

Since 2014, the University of Florence has joined the Interuniversity Center of Integrated Systems for the Marine Environment (ISME) [ISME, 2019], which gathers research institutions from all over Italy and whose main goal is to act as a common platform for joint operations for what concerns marine robotics and, generally speaking, marine field. As a result of the support of the Naval Experimentation and Support Center (Centro di Supporto e Sperimentazione Navale) (CSSN) of the Italian Navy (formalized as the SEALab joint laboratory), several tests at sea, with the aiming of trying out the vehicles of the UNIFI DIEF MDM Lab fleet, have been performed during the Ph.D. in the Ligurian Sea.

Figure 1.3: The logo of the ISME [ISME, 2019].

In 2016, the University of Florence took part in the Bridging Robots for Underwater Communication Enrichment (BRUCE) project, subproject of the European FP7-funded project Sensing, monitoring and actuating on the UNderwater world through a federated Research InfraStructure Extending the future Internet (SUNRISE) [SUNRISE, 2019].

Figure 1.4: The logo of the SUNRISE project [SUNRISE, 2019].

The main BRUCE objective was to use underwater vehicles to bridge underwater networks composed of multi-vendor acoustic modems (more information can be found in [Ridolfi et al., 2018]). To do so, MARTA AUV was equipped with two heterogeneous acoustic modems from two different manufacturers, and its main task was to act as an "interpreter". It is worth noting that, since two heterogeneous acoustic modems, which did not present a common communication protocol was involved, data exchange was possible only thanks to the bridging capability of MARTA AUV.
In 2018, the University of Florence together with Mechatronics and Dynamic

Modeling Team (MDM Team S.r.l.), an official spin-off company of UNIFI DIEF, joined Autonomous underwater Robotic and sensing systems for Cultural HEritage discovery COnservation and in sitU valorization (ARCHEOSUb) European project [ARCHEOSUb, 2019].

Figure 1.5: The logo of the ARCHEOSUb project [ARCHEOSUb, 2019].

According to the project targets, namely surveying, conservation, protection, and valorization of new and existing underwater Underwater Cultural Heritage (UCH) sites as well as developing products and services in support of them, a new light-weight, low-cost AUV, called Zeno Environment Nautical Operator (Zeno), was designed and developed by the consortium. Real-time monitoring, surveillance, and communication of multimedia data using an underwater sensors network (that includes Zeno AUV to be sent to sites of interest) has been one of the outcomes of this project and several underwater missions were performed in Italy and Israel.
In 2019, the University of Florence took part in the EUMarineRobots (EUMR) project [EUMR, 2019] as a node of ISME.

Figure 1.6: The logo of the EUMR project [EUMR, 2019].

The EUMR consortium (15 partners from 10 countries) is constituted of a network of distinguished European key players with diverse expertise across marine robotics sectors. According to the project objectives, the main target is to open up key national and regional marine robotics research infrastructures to all European researchers from both academia and industry.

In the framework of the EUMR project, underwater missions were performed by UNIFI DIEF at Vulcano Island, Messina (Italy) with MARTA AUV and FeelHippo AUV. The main goal was to "map" carbon dioxide bubbles in the sea, responsible for negative effects on underwater fauna and flora. In addition to the participation in regional, national, and European projects, UNIFI DIEF took part in many non-student and student robotics competitions during the last years. Just to name a few examples, a team of UNIFI DIEF participated to Student Autonomous Underwater Vehicles Challenge -Europe (SAUC-E) competition in 2012, 2013, 2016, and European Robotics League Student Autonomous Underwater Vehicles Challenge -Europe (ERL SAUC-E) in 2018, and 2019. Furthermore, in 2015 euRathlon competition was joined, whereas a team took part in European Robotics League (ERL) in 2017.
Throughout the years, the teams of UNIFI DIEF have gained expertise and proficiency. In 2013 and 2016, the third place was obtained, while in 2017, the participating team was awarded Second-in-Class in "Pipe inspection and search for search for missing workers (Sea+Air) during ERL Emergency Robots 2017. In 2018 and 2019, the team won the competition in the sea domain, and it was awarded "Best Marine Team during ERL SAUC-E 2018, and ERL SAUC-E 2019. More information concerning these competitions can be found in [Ferri et al., 2015] and [Ferri et al., 2017].ing these competitions can be found in [Ferri et al., 2015] and [Ferri et al., 2017].

1.2 State-of-the-art of underwater navigation

Since the beginning of marine robotics, the underwater localization problem has always been a sensed subject. Due to the high level of accuracy required and the well-known physical limitations of radio-frequency signal in the underwater environment [Barclay, 2003], scientists and researchers have resorted to different solutions. From this point of view, the problem is similar to the localization of land and air robots in an indoor environment or, generally speaking, in every Global Positioning System (GPS)-denied scenario.
Considering the general problem of pose estimation (attitude estimation and position estimation), a first rough classification can be made basing on how the vehicle attitude is estimated. As reported by [Paull et al., 2014] and

[Fanelli, 2019], regardless of the specific estimator involved, two different approaches can be pursued. On the one side, position with attitude estimation are tackled together, leading to a complete pose estimation algorithm. On the other side, attitude is separately estimated and its output is used as input to the position estimation filter. It is worth underlying that the UNIFI DIEF MDM Lab vehicle fleet resorts to the latter option.

As the simplest solution, despite their straightforward philosophy, Dead Reckoning (DR) strategies have proven satisfyingly reliable if the available sensors are sufficiently accurate. A well-accepted approach is to integrate over time measurements from a Doppler Velocity Log (DVL) combined with an attitude reference (obtained, *e.g.*, from an Inertial Navigation Systems (INS) together with a Fiber Optic Gyroscope (FOG)), often leading to good navigational accuracy [Miller et al., 2010].

A more elaborate approach for both position and attitude estimation, usually exploited in marine robotics, is based on the Kalman Filter (KF) [Kalman, 1960], on the Extended Kalman Filter (EKF) [Bar-Shalom et al., 2004], [Hong et al., 1996], and [Mallios et al., 2010] or the Unscented Kalman Filter (UKF) [Julier and Uhlmann, 2004],[Allotta et al., 2016b], and [Costanzi et al., 2019] typically employed when non-linearities in the dynamic description of the system arise.

Generally speaking, all require knowledge of the linear speed of the AUV, which is (for the majority of times) obtained using specialized and *ad'hoc* underwater sensors, such as the DVL.

Unfortunately, due to the presence of noise and bias on the employed navigation sensors, the above-mentioned strategies usually fails in terms of position accuracy when the vehicle is required to perform long underwater missions. To overcome this issue, periodic GPS resets with the aim of bounding unwanted position estimation drifts [Leonard and Bahr, 2016] are often performed, leading to a time- and power-consuming solution, especially if missions at high depths are considered.

Alternatively, absolute underwater position information can be obtained using beacons, with two types of systems most commonly employed being the Long BaseLine (LBL) and the UltraShort BaseLine (USBL) [Leonard and Bahr, 2016]. To ease the localization problem, static and/or dynamic local sensors networks composed of localizing acoustic devices have gained attention [Yoerger et al., 2007] and [Bahr et al., 2009]. Single beacon localization

has been proposed, whereby a vehicle (usually known as *beacon vehicle*) with good quality positioning information is able to transmit range information acoustically to one or more underwater vehicles, as described in [Tan et al., 2014] and [Webster et al., 2013]. In addition, Moving Long BaseLine (MLBL) systems—that are a generalization of LBL—have been suggested. Here, as stated in [Yan et al., 2015], the arrays of transponders are fully mobile and self-calibrating; thus, they do not constrain the operating site to a fixed area. Contributions can be found for example in [Curcio et al., 2005] and [Bishop et al., 2010]. As stated in [Melo and Matos, 2017], the main disadvantages are the total cost, the deployment, and recovery time (especially for the LBL and the MLBL), and a detailed calibration process, which is necessary to obtain optimal positioning accuracy (especially for the USBL).

Over the last two decades, several strategies exploiting optical or acoustic payload to solve localization problems have been proposed. In particular, Simultaneous Localization and Mapping (SLAM) techniques have been successfully applied in [Dissanayake et al., 2000], [Williams et al., 2000], [Mahon and Williams, 2004], and [Mallios et al., 2010], and [Norgren and Skjetne, 2018] and are often favored to terrain-based ones [Kullander, 1989], [Nygren and Jansson, 2004] because they offer, as usually referred, a "self-contained" solution [Ribas et al., 2010]. As a consequence, historically, the vast majority contributions concerning optical and acoustic payload in navigation-aiding have been focused on constraining the navigational drift of the AUV; thus, particular emphasis has been paid to the use of these devices complementary to a standard navigation sensors set.

1.3 State-of-the-art of FLS

2D FLSs are a class of SONAR whose first real-time version was introduced (and patented) by [EchoPilot, 2019] (now [Daniamant A/S, 2019]) in 1992 with the model called "FLS 1". This kind of device has been gaining interest in the last years, and, at the time of writing, several of them with different technological peculiarities are present in the market, see Tab.1.1. Generally speaking, their main characteristics are high resolution and high refresh rate; when compared with Mechanically Scanned Imaging SONARs

Principal FLSs	
Vendor	**Model**
Teledyne Technologies Incorporated	BlueView P900-130, BlueView P900-45
IMAGENEX TECHNOLOGY CORP.	965A 1100
Tritech International Ltd	Gemini 720ik, Gemini 720im, Gemini 720is
Kongsberg Maritime	M3
Blueprint Design Engineering Ltd.	Oculus M370s, Oculus M750d, Oculus M1200d
Sound Metrics Corp	DIDSON, Aris Voyager, Aris Explorer

Table 1.1: Principal FLSs present in the market at the time of writing.

(MSISs), because of their high refresh rate, distortions related to the vehicle motion are in fact not present. In addition to this, when compared with SideScan SONARs (SSSs), combining returned acoustic echoes in order to produce an artifact of the insonified scene is not necessary, since this class of devices can directly render a 2D image.

Their principal usage is for OA, acoustic mosaicing (2D or 3D), ATR (especially mine detection), and navigation-aiding. It is worth noting that OA and ATR are often proposed with suitable re-planning or tracking solutions.

The typical approach in OA is based on segmenting and extracting relevant features from acoustic images; examples can be found in [Petillot et al., 2001], [Karoui et al., 2015], and author's work work in [Ridolfi et al., 2020].

For what concerns ATR, different and diverse methods can be found in the current literature. Some are known as Template Matching (TM) techniques, where small parts of the image to be investigated are cross-correlated with template images [Hurtos et al., 2014] and [Wenwu et al., 2017]. Other solutions try to locate echos that are locally higher than their background, fusing this information with a priori knowledge of the target geometry [Galceran et al., 2012], [Gu et al., 2015]. In the last years machine learning-based solutions are gaining interest and contributions can be found in [Kim et al., 2016], [Kim and Yu, 2016], [Valdenegro-Toro, 2016], [Valdenegro-Toro, 2017], [Dos Santos et al., 2017], and [Rixon Fuchs et al., 2018].

For what concerns acoustic mosaicing (tackled in the first months of the

Ph.D. period, see Appendix B), remarkable contributions can be found in [Kim et al., 2005], [Nicosevici et al., 2009], [Negahdaripour et al., 2011], [Hurtós et al., 2015], and [Ferreira et al., 2015] for the 2D version and in [Ozog et al., 2015] for the 3D one. Regardless of the final use (mosaicing, structure from motion or navigation-aiding), one of the main topics of interest has always been to understand how to find the transformation that puts in relation two images acquired from two different points. This kind of problem, widely known in the computer vision community, is called *registration*.

Historically, researches tried to extend the achievement obtained in terms of images registration of optical images to acoustic ones. In particular, the first attempts applied feature-based methods to FLS images. In this sense, contributions can be found in [Negahdaripour et al., 2005], [Kim et al., 2005], [Kim et al., 2006], [Fallon et al., 2013], [Li et al., 2014], [Huang and Kaess, 2015], [Shin et al., 2015], and [Li et al., 2018]. On the one hand, feature-based approaches can handle complex transformation models between the images. On the other hand, generally speaking, this kind of methods applied to FLS images suffer from wrong matches and feature instability, causing an incorrect registration estimation, as pointed out by [Hurtós Vilarnau, 2014] and [Hurtós et al., 2013b]. As a consequence, with the aim of increasing image registration robustness, researches tried to extrapolate features at greater scale [Johannsson et al., 2010a], [Aykin and Negahdaripour, 2012], [Hover et al., 2012], and [Aykin and Negahdaripour, 2013]. Although the above-mentioned methods are unquestionably worth, the presence of stable and conspicuous features is necessary for a correct registration process. Thus, following the above-mentioned approach, but taking it towards a larger scale, [Hurtós et al., 2015], [Hurtós et al., 2013b], [Zhang et al., 2016], and [Franchi et al., 2019a] proposed registration techniques that work in the image frequency domain considering the whole image content.

To the author's best opinion, the current state-of-the-art for what concerns FLS images registration is mature, and future developments will be influenced more by the raw quality of the acoustic image than by the particular techniques employed.

For what concerns FLSs in navigation-aiding, the vast majority contributions are focused on constraining the navigational drift of the AUV, giving a complementary role to a standard navigation sensors set. Accordingly, as

stated by [Durrant-Whyte and Bailey, 2006], and [Li et al., 2018], navigation can be adjusted, for example, by means of self-correction using environmental landmarks, whereby observations of features or landmarks (assumed time-invariant) and re-observation of the landmarks are crucial [Hidalgo and Bräunl, 2015]. Therefore, FLSs are usually included in a SLAM framework. A concise overview of the main contributions for navigation purposes is reported here, and for further information, the interested reader is encouraged to read [Ribas et al., 2010], and [Valencia and Andrade-Cetto, 2018].
In [Walter et al., 2008] an FLS-based SLAM for performing a ship's hull inspection is shown. Here, FLS images are related using features extracted from different frames. In [Hover et al., 2012], a feature-based navigation approach is used to complement a dead-reckoning sensor stream for ship's hull inspections, both an FLS and an optical camera are employed. In [Johannsson et al., 2010b], a drift-free navigation solution during harbor surveillance and ship's hull inspection employing an FLS is proposed. Another feature-based solution is presented in [Li et al., 2018], where a ship's hull inspection is undertaken. A SLAM algorithm that makes use of an FLS as the sole perceptual sensor to perform navigational drift correction of a DVL/Inertial Measurement Unit (IMU)-based odometry navigation framework is outlined. A study by [Aykin and Negahdaripour, 2012] describes a technique implemented on FLS images able to detect stable and reliable features located at the region level rather than at the pixel level. However, although the proposed solution is considered to be able to improve the precision of AUV navigation, no specific result was outlined. In [Hurtós et al., 2015], a mosaicing framework is presented, able to create acoustic maps along various vehicle track-lines, where both translational and rotational 2D motions can be handled. However, the authors state that the proposed framework is tailored for an offline approach, where the trajectory followed by the vehicle is computed a posteriori, and integration in an online navigation system is only hypothesized. In [White et al., 2010], six SLAM techniques have been applied to the exploration and mapping of ancient cisterns (where it is much easier to retrieve information from the surrounding environment); however, the open sea navigation problem is not tackled. In [Shin et al., 2015], an imaging FLS-based SLAM is proposed; a two-view Bundle Adjustment (BA) [Triggs et al., 1999] algorithm is employed to enhance pose estimations and a tank test with DVL measurements is presented. An attitude and trajectory

estimation of a moving underwater platform by processing acoustic data from an FLS is proposed in [Henson and Zakharov, 2018]. Together with providing navigation information, it is shown that the solution can also be used to build a mosaic of the underwater scene. The algorithm works in post-processing, and data sets from feature reach environment (ships hull inspection and debris field) are used.
To the author's best knowledge, few proposals focused on effectively substituting a DVL in favor of an FLS for underwater navigation are present. In addition to this, the proposed solutions are always validated offline. In [Yang and Huang, 2017], an acoustic-inertial navigation system that fuses acoustic measurements from an FLS and inertial ones from an IMU within a tightly-coupled, stochastic cloning-based EKF framework is proposed. The solution is validated through Monte-Carlo simulations under various conditions, but any evaluation with real-acoustic images is presented. In [Song et al., 2018], a method is presented that relies on optical and acoustic images. A mixed approach that uses an FLS, a standard camera, or a DR is proposed. Although the solution is tested using data gathered from experimental tests, the navigation performance of the technique is not thoroughly investigated. In the context of FLS-based speed estimation, it is worth citing the author's contribution in [Franchi et al., 2019a].

1.4 Motivation

The main contribution of the work presented here focuses on promoting the use of FLS to aid underwater navigation, proposing a solution able to estimate linear speed without exploiting DVL measurements (but not obstructing cooperation). Working on FLS images, a Fourier-based registration method is employed, and the results are shown to be comparable with the ones obtained with a DVL-based navigation system. The author is aware that the achieved performance is unlikely to be better with respect to a DVL-based navigation system, even in the near future; indeed, the author wishes to point out that even if the proposed solution is shown to work without exploiting any DVL measurement, cooperation with the DVL is possible. This way, more linear speed measurements could be obtained. In addition to this, using FLS to aid navigation could potentially outline other advantages. Using an augmented set of devices able to provide

navigation information represents an intrinsic boost in redundancy, preventing failures due, for example, to underwater sensor-denied scenarios (such as DVL-denied scenarios when proximity to the seafloor or other surfaces takes place [Miller et al., 2010] or when a substantial number of gaseous bubbles is present). Indeed, as opposed to the DVL, the FLS possesses more beams (for example, the Nortek DVL1000 DVL has 4 beams, whereas the Teledyne BlueView M900-130 2D FLS 768) that are spread into a broader area, thus improving reliability. DVL failings in the presence of bubbles are well-documented in the current literature (see, for example, [Groves, 2015]) and have been experienced during several tests at sea performed by UNIFI DIEF [Franchi et al., 2019a]. Conversely, the presence of bubbles, which can be noticed within FLS images as strong return echoes spots, is usually tolerable and not capable of jeopardizing FLS operations. Moreover, although bigger AUVs enable the use of more sophisticated instrumentation and are able to carry a heavy payload, smaller AUVs are constrained to limited payload carrying capabilities. Hence, in addition to constituting a valuable research interest, multitasking onboard sensors represent a solution that offers compactness and avoids the use of some instruments. Besides this, to better the dynamic modeling of the AUV, a light-weight online estimator for the longitudinal dynamics and a more realistic propulsion model are developed. Lastly, an Adaptive Unscented Kalman Filter (AUKF)-based navigation solution is proposed. Its employment, in favor of a simple UKF, is justified for two reasons. First, it answers to the typical limitation of Bayesian estimators, namely the knowledge of the a priori information about the process noise and the measurement noise. Here, the problem is solved by continuously exploiting the filter learning history, thus evolving dynamically. Second, it permits to characterize (intrinsically) FLS estimations in a statistic way. To the author's best knowledge, the typical approach is to employ heuristic methods that consider some metrics related to the goodness of the registration process [Pfingsthorn et al., 2010], and [Hurtós et al., 2015]. However, these techniques are strongly dependent on the metrics used and on the particular heuristic employed. The proposed solution instead bypasses this issue, relying on an adaptation that continuously exploits the filter learning history.

1.5 Thesis structure

The research activity carried out during the Ph.D. period started with analyzing the current development in FLS operations in an underwater environment for acoustic mosaicing purposes. This task was satisfyingly addressed during the first months of the Ph.D. period, and an online framework for underwater mosaicing tailored to the characteristics of FLS imagery was proposed in [Franchi et al., 2018] (see Appendix B). Afterward, how to suitably fuse the research background of the UNIFI DIEF in underwater navigation with the above-mentioned research activity, was pursued. In this sense, first, an intense review of the current state-of-the-art in underwater navigation and localization was accomplished, trying to analyze the current and future trends. Second, following the encouraging results presented in [Franchi et al., 2018], [Franchi et al., 2019b], and [Franchi et al., 2019a] the joining link was identified in trying to mimic DVL behavior with an FLS device in terms of linear speed estimations or, generally speaking, translational motions (see Section 4.1). Following the current state-of-the-art in underwater navigation at UNIFI DIEF, where attitude is separately estimated and its output are used as input to the position estimator (see [Allotta et al., 2016c] and [Costanzi et al., 2016]), the latter both in its DR or UKF version was augmented in order to manage estimations from FLS. Afterward, the development followed two parallel paths. On the one hand, the dynamic model of the vehicle, with respect to state-of-the-art in underwater navigation at UNIFI DIEF, was further developed; the propulsion model was further investigated [Franchi et al., 2019a] (see Section 4.2.1) and an online estimator for the longitudinal drag of the vehicle, which could be easily applied to the other Degree of Freedom (DOF) of the vehicle, was proposed (see Section 4.2.2). On the other hand, the UKF estimator was improved, and an AUKF-based solution was developed (see Section 4.3).
Finally, the last part of the Ph.D. period was aimed to test the above-mentioned navigation solutions both during simulations ([Franchi et al., 2019a]) and tests at sea, whose results are presented in this work (see Chapter 5).
The main result of the Ph.D. period is thus the development of a complete position estimation algorithm (both in dead-reckoning, UKF, and AUKF version) that can exploit, among other devices, data from an FLS.

Chapter 2

Description of the Involved Vehicles

This chapter introduces the AUVs developed during the past eight years by the UNIFI DIEF MDM Lab. Although the UNIFI DIEF MDM Lab fleet is capable of performing diverse and heterogeneous underwater tasks, each vehicle was developed for a specific purpose, from research projects-related subjects (Typhoon class AUVs, MARTA AUV, and Zeno AUV) to student robotics competitions (FeelHippo AUV). The goal of this chapter is to provide a glance (giving the proper references), to each of the above-mentioned vehicles. In particular, the navigation sensor-set as well the payload present on board, the materials description, and the main design characteristics will be covered. Since Typhoon class AUVs finished to be developed before the Ph.D. period, its description will be omitted. Lastly, it is worth highlighting that, although equipped with different payloads, the UNIFI DIEF MDM Lab fleet always presents the following navigation sensors (or a subset of them)[1]:

- GPS, used to initialize the vehicle position while on surface or to reset it after an underwater mission;
- IMU and triaxial compass, used to measure vehicle attitude;
- Depth Sensor (DS), employed to retrieve the depth of the vehicle;
- DVL, used to measure the linear velocity;
- FOG, employed to improve of the vehicle's heading;

[1]What is reported in the following descriptions is considered at the time of writing.

- acosutic localization systems, used to retrieve the position of the vehicle during underwater operations;

2.1 MARTA AUV

MARTA AUV, a torpedo-shaped vehicle developed and built during the European project ARROWS by the MDM Lab presents a remarkable modularity. Indeed, throughout ARROWS, following archaeologists' guidelines, a flexible platform capable of easing activities at sea was developed.
The vehicle is composed of different modules, where each of them addresses to a particular function or task. Therefore, its final structure can vary and thus tailored to the particular user's request. In Table 2.1, the physical characteristic related for its standard configuration are reported.

MARTA AUV main characteristics	
Dimensions [mm]	approx. 3500×180
Dry mass [kg]	85
Max longitudinal speed [m/s] (kn)	approx. 2 (4)
Max lateral speed [m/s] (kn)	approx. 0.3 (0.6)
Max depth [m]	150
Autonomy [h]	4-5 (per battery module and standard operations)

Table 2.1: MARTA AUV physical data and performance.

The modules of the vehicle are composed of anticorodal aluminum type 6082-T6, constituting a smart trade-off between lightness and mechanical strength. With the aim of gaining resistance against saltwater corrosion, a hard anodizing process was carried out. Two O-rings, placed at the end of each module in order to provide a watertight connection. Moreover, before operations at sea, an internal depressurization of 0.3 bar is performed to improve stiffness and alignment among modules.
It is worth noting that an electrical modularity is present as well: in fact, the electrical interfaces of each module of the vehicle are identical on both sides. Two thrusters by BlueRobotics [Blue Robotics Inc., 2019] are paired with four custom-made fixed pitch propellers and used to control five DOFs. In particular, the yaw angle can be controlled in ∞^1 ways; instead, the roll cannot be actively handled, and its stability is ensured by proper positioning of the Center of Gravity (CG) and the Center of Buoyancy (CB). For what

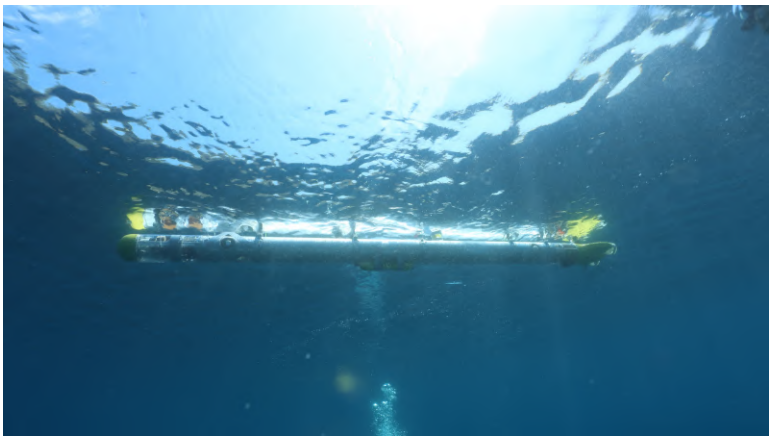

Figure 2.1: MARTA AUV during a test at sea.

concerns navigation sensors, payload and HardWare (HW) devices, MARTA AUV complete set is reported below:

- Xsens MTi-G-710 IMU-enhanced Global Navigation Satellite System (GNSS)-INS and Attitude and Heading Reference System (AHRS);
- First Sensor SSI series DS;
- LinkQuest NavQuest 600 Micro DVL;
- KVH DSP 1760 single-axis FOG;
- SeaKing Tritech SSS;
- WiFi access point;
- 868+ RFDesign radio modem;
- EvoLogics S2CR 18/34 acoustic modem;
- a Basler ace camera;
- one ODROID-XU board;
- one Intel i-7 Mobile CPU.

2.2 FeelHippo AUV

FeelHippo AUV has been designed and developed both for the participation in student robotics competitions and for undertaking research topics.

Indeed, during the last few years the vehicle participated at SAUC-E 2013, euRathlon 2015, ERL Emergency Robots in 2017, ERL SAUC-E 2018, and ERL SAUC-E 2019. Starting from the first low-budget prototype, which dates back to 2013, to the final 2019 version, FeelHippo AUV has undergone several overhauls throughout the years.
The last FeelHippo AUV version, visible in Fig.2.2, is described in the following.

Figure 2.2: FeelHippo AUV at Vulcano Island, Messina (Italy) in 2019.

The main features of the vehicle are reduced dimensions and weight, together with the presence of top-of-the-line sensors, making it a compact and reliable underwater platform.
A Plexiglass® hull with an internal diameter of 200 mm and 5 mm thickness constitutes the central body of the vehicle, where the non-watertight hardware and electronics are housed. The connection between the central part of the vehicle and the two outermost domes is provided by two metal flanges; moreover, two O-rings that guarantee a watertight connection. In addition, six metal bars act as tie rods, increasing the overall stiffness results.

FeelHippo AUV main characteristics	
Dimensions [mm]	approx. 600×640×500
Dry mass [kg]	35
Max longitudinal speed [m/s] (kn)	approx. 1 (2)
Max lateral speed [m/s] (kn)	approx. 0.2 (0.4)
Max depth [m]	30
Autonomy [h]	2-3

Table 2.2: FeelHippo AUV physical data and performance.

Four thrusters by BlueRobotics [Blue Robotics Inc., 2019] arranged in a vectored configuration (two on the stern and one each on both lateral sides tilted at 45°) are connected to FeelHippo AUV using custom-made (3D-printed) plastic parts. Except for the roll and pitch motion (that are limited by hydrostatic stability), all the DOFs of the vehicle (translational motion and yaw) can be controlled.
A list of all the electronic devices and the sensor sets with which FeelHippo AUV is equipped is listed as follows:

- Intel i-7-based LP-175-Commel motherboard (used for onboard processing);
- U-blox 7P precision GPS;
- Orientus Advanced Navigation AHRS;
- KVH DSP 1760 single-axis high precision FOG;
- Nortek DVL1000 DVL, measuring linear velocity and acting as DS;
- EvoLogics S2CR 18/34 acoustic modem;
- Teledyne BlueView M900 2D FLS;
- Ubiquiti Bullet M2 WiFi access point;
- 868+ RFDesign radio modem;
- one bottom-looking ELP 720p MINI IP camera;
- one Microsoft Lifecam Cinema forward-looking camera;
- two lateral ELP 1080p MINI IP cameras;
- two Intel Neural Compute Stick 2 for Artificial Intelligence for Artificial Intelligence (AI) applications.

2.3 Zeno AUV

Zeno AUV is a vehicle developed during the European Project ARCHEOSUb, thanks to the collaboration between the University of Florence and MDM Team S.r.l.. Its propulsion system was meant to control all the six

DOFs actively, and it is composed of eight thrusters by [Blue Robotics Inc., 2019] in vectored configuration. Therefore, redundancy with respect to the DOFs of the vehicle guarantees hovering capability and smooths the system maneuverability. Its main features are compact design and high portability, together with a rapid battery replacement, useful when, for example, battery change on board of a boat becomes necessary.

Figure 2.3: Zeno AUV at Gallipoli, Lecce (Italy) in 2018.

The complete description of HW, sensors, and payload is reported below:

- Advantech MIO-3260 Intel i-7 as main computer;
- UDOO x86 as slave computer;
- U-blox Neo-7P precision GPS;
- Orientus Advanced Navigation AHRS;
- KVH DSP 1760 single-axis high precision FOG;
- Nortek DVL1000 DVL, measuring linear velocity and also acting as DS;
- EvoLogics S2CR 18/34 acoustic mode;
- Ubiquiti Bullet M2 WiFi access point;

- 868+ RFDesign radio modem;
- one bottom-looking ELP 720p MINI IP camera;
- one Microsoft Lifecam Cinema bottom-looking camera;
- one ELP 1080p MINI IP forward-looking camera;
- DeepVision DE3468D SSS.

Its physical characteristics are summarized in Table 2.3.

Zeno AUV main characteristics	
Dimensions [mm]	approx. 1000×800×200 mm
Dry mass [kg]	40
Max longitudinal speed [m/s] (kn)	approx. 2 (4)
Max depth [m]	120
Autonomy [h]	4 (in standard operations)

Table 2.3: Zeno AUV physical data and performance.

Chapter 3

Preliminaries and notation

This chapter covers the notation employed in the rest of the work and gives a complete review of the fundamental theoretical and mathematical concepts used throughout this thesis.
First, the kinematic and dynamic modeling of an AUVs is treated. Second, the principles of Kalman filtering are described, with particular emphasis on the UKF. Finally, the imaging geometry model of an FLS and the critical concepts of the registration methods in the spectral domain are reported.

3.1 Kinematic and dynamic modeling of the AUV

The equations that describe the motion of a general rigid body freely moving within a fluid are discussed in this section, and further information can be found in [Fossen et al., 1994]. The main assumptions, which are the foundations of the following treatment, consider any frame located on the Earth's surface as *inertial* (the Earth rotation is thus neglected) and any involved vehicles as a *rigid body*. The Society of Naval Architects and Marine Engineers (SNAME) notation, commonly adopted for marine vehicles, is used throughout this thesis (see [Fossen et al., 1994]).
The pose of the AUV (in terms of position and attitude) is retrieved with respect to two reference frames. The first one is a local Earth-fixed reference frame whose axes point, respectively, North, East, and Down (*North, East, Down (NED) frame*) $\left\{O^N x^N y^N z^N\right\}$, whereas the second one, namely the *body frame*, usually centered on the CG of the vehicle, with the forward motion direction represented by the x-axis (*surge*) and the z-axis (*heave*)

pointing down. Lastly, the y-axis (*sway*) completes a right-handed reference frame $\{O^b x^b y^b z^b\}$. In the rest of the thesis, the following notation is employed: a generic vector $\boldsymbol{p} \in \mathbb{R}^3$ expressed in a particular $\{O^0 x^0 y^0 z^0\}$ frame is denoted with ${}^0\boldsymbol{p}$, whereas, if it is convenient to define vectors without an explicit reference to a specific coordinate frame (coordinate free vector), it will be simply indicated with $\boldsymbol{p}$. A generic rotation matrix $R \in \mathbb{SO}(3)$ is indicated with three indices ${}^kR_i^j$, where ${}^kR_i^j$ is an operator that maps (rotates) unit vectors of the frame j ($\{O^j x^j y^j z^j\}$) in unit vectors of the frame i ($\{O^i x^i y^i z^i\}$, both expressed in the frame k ($\{O^k x^k y^k z^k\}$). The situation is depicted in compact form as:

$$ {}^kR_i^k = ({}^kR_i^j)({}^kR_j^k), \tag{3.1} $$

where the columns of ${}^kR_i^k$ and ${}^kR_j^k$ are the projections of the unit vectors of the frame i in the frame k and of the frame j in the frame k, respectively. Given a generic ${}^kR_i^j$, if $k = j$, the three-indexes notation could not be employed; however, for the sake of completeness, the full notation will be used in the rest of the thesis. In the following, superscript ^{N} will denote a quantity in the NED frame, whereas ^{b} will describe a quantity in the body one.

The AUV pose with respect to the NED frame is represented with $\boldsymbol{\eta} = \left[{}^N\boldsymbol{\eta}_1^\top \ \boldsymbol{\eta}_2^\top\right]^\top \in \mathbb{R}^6$, where ${}^N\boldsymbol{\eta}_1$ indicates the position of the CG of the vehicle with respect to the NED frame and $\boldsymbol{\eta}_2$ its orientation. In particular, a triplet of Euler angles expressed with respect to the fixed NED, namely roll (ϕ), pitch (θ), and yaw (ψ), is used (Roll, Pitch and Yaw (RPY)). Moreover, the linear and angular velocities of the vehicle with respect to a body-fixed reference frame is denoted with ${}^b\boldsymbol{\nu} = \left[{}^b\boldsymbol{\nu}_1^\top \ {}^b\boldsymbol{\nu}_2^\top\right]^\top$, where u, v, and w are the linear velocities along the axes of the body frame (*surge*, *sway*, and *heave*), whereas p, q, and r are the angular counterparts about the above-mentioned axes.

$$ \begin{aligned} \boldsymbol{\eta} &= [\ {}^{\boldsymbol{N}}\boldsymbol{\eta}_1^\top \quad \boldsymbol{\eta}_2^\top\ ]^\top, \quad {}^N\boldsymbol{\eta}_1 = [x \quad y \quad z]^\top, \\ \boldsymbol{\eta}_2 &= [\phi \quad \theta \quad \psi]^\top, \ {}^b\boldsymbol{\nu} = [\ {}^{\boldsymbol{b}}\boldsymbol{\nu}_1^\top \quad {}^{\boldsymbol{b}}\boldsymbol{\nu}_2^\top\ ]^\top, \\ {}^{\boldsymbol{b}}\boldsymbol{\nu}_1 &= [u \quad v \quad w]^\top, \quad {}^{\boldsymbol{b}}\boldsymbol{\nu}_2 = [p \quad q \quad r]^\top \end{aligned} \tag{3.2} $$

The situation is depicted in Fig.3.1 and the complete kinematic model of the vehicle is reported in Eq.3.3.

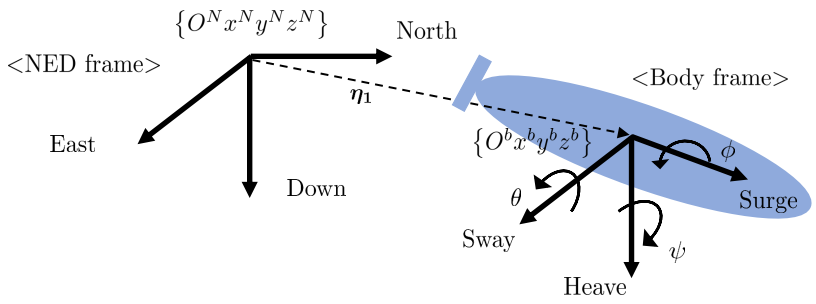

Figure 3.1: The SNAME notation.

$$\begin{pmatrix} {}^N\dot{\boldsymbol{\eta}}_1 \\ \dot{\boldsymbol{\eta}}_2 \end{pmatrix} = \begin{bmatrix} {}^N R_b^N(\boldsymbol{\eta}_2) & 0_{3\times3} \\ 0_{3\times3} & T_b^N(\boldsymbol{\eta}_2) \end{bmatrix} \begin{pmatrix} {}^b\boldsymbol{\nu}_1 \\ {}^b\boldsymbol{\nu}_2 \end{pmatrix} \tag{3.3}$$

where ${}^N R_b^N$ represents the rotation matrix between the body and the fixed reference system and $T_b^N(\boldsymbol{\eta}_2)$ is the Euler matrix (see Eq.3.4).

$$T_b^N(\boldsymbol{\eta}_2) = \begin{bmatrix} 1 & \mathrm{s}\phi\mathrm{t}\theta & \mathrm{c}\phi\mathrm{t}\theta \\ 0 & \mathrm{c}\phi & -\mathrm{s}\phi \\ 0 & \mathrm{s}\phi/\mathrm{c}\theta & \mathrm{c}\phi/\mathrm{c}\theta \end{bmatrix} \tag{3.4}$$

It can be noted that T_b^N is not defined for $\theta = \pm 90°$; however, the majority of AUVs does not operate close to this singularity. The compact form of Eq.3.3 is visible in Eq.3.5, where the definition of $J(\boldsymbol{\eta})$ is trivial.

$$\dot{\boldsymbol{\eta}} = J(\boldsymbol{\eta})\boldsymbol{\nu} \tag{3.5}$$

Additionally, the vector of forces and moments acting on the vehicle ${}^{\boldsymbol{b}}\boldsymbol{\tau} \in \mathbb{R}^6$ (usually referred in the body-fixed frame) can be represented as:

$${}^b\boldsymbol{\tau} = [\ {}^b\boldsymbol{\tau}_1^\top \quad {}^b\boldsymbol{\tau}_2^\top\ ]^\top, \quad {}^b\boldsymbol{\tau}_1 = [X \quad Y \quad Z]^\top, \quad {}^b\boldsymbol{\tau}_2 = [K \quad M \quad N]^\top \tag{3.6}$$

The generalized forces ${}^b\boldsymbol{\tau}$, the thrusts carried out by the motors $\boldsymbol{T} \in \mathbb{R}^m$ ($\boldsymbol{T}$ is a vector that collects the thrusts exerted by the the m motors), and the rotational speed of the motors $\boldsymbol{u}_{rpm} \in \mathbb{R}^m$, are linked using the following relation:

$${}^b\boldsymbol{\tau}(\boldsymbol{\nu}, \boldsymbol{u}_{rpm}) = B\mathbf{T}(\boldsymbol{\nu}, \boldsymbol{u}_{rpm}) \tag{3.7}$$

where B is a constant matrix $\in \mathbb{R}^{6\times m}$ (assuming the vehicle and the thrusters are not reconfigurable) that depends upon the thruster poses with respect the CG. Its expression is reported in Eq.3.8 and Eq.3.9.

$$B = \begin{bmatrix} B_1 \\ B_2 \end{bmatrix}, \tag{3.8}$$

with

$$\begin{aligned} B_1 &= \left[\cdots {}^b\mathbf{n}_{mi} \cdots \right], \\ B_2 &= \left[\cdots ({}^b\mathbf{P}_{mi} \times {}^b\mathbf{n}_{mi}) \cdots \right], \end{aligned} \tag{3.9}$$

where ${}^b\mathbf{n}_{mi}$ is the axis of the i-th motor expressed in the body frame $\left\{O^b x^b y^b z^b\right\}$ and ${}^b\mathbf{P}_{mi}$ is the thruster center of the i-th motor with respect to the CG expressed in the body frame.
According to [Fossen et al., 1994], the vehicle dynamics is governed by the following (vector) equation:

$$M_m\dot{\boldsymbol{\nu}} + C(\boldsymbol{\nu})\boldsymbol{\nu} + D(\boldsymbol{\nu})\boldsymbol{\nu} + \boldsymbol{g}_{\boldsymbol{\eta}}(\boldsymbol{\eta}) = \boldsymbol{\tau}(\boldsymbol{\nu}, \boldsymbol{u}_{rpm}) \tag{3.10}$$

M_m is the mass matrix, $C(\boldsymbol{\nu})$ is the centripetal and Coriolis matrix, $D(\boldsymbol{\nu})$ is the damping matrix, $\boldsymbol{g}_{\boldsymbol{\eta}}(\boldsymbol{\eta})$ takes into account the effects of gravity and buoyancy, and $\boldsymbol{\tau}(\boldsymbol{\nu}, \boldsymbol{u}_{rpm})$ describes the map between the vehicle speed ($\boldsymbol{\nu}$) and the rotational speed of the motors ($\boldsymbol{u}_{rpm}$), which is the vector of *control inputs*, to the resultant thrust action on the vehicle.

For the sake of clarity, each term in Eq.3.10 is briefly described.

Mass and inertia matrix M_m

M_m is constituted of two terms:

$$M_m = \tilde{M}_m + M_a, \tag{3.11}$$

where $\tilde{M}_m$ depends upon vehicle geometry and material (with $\tilde{M}_m = \tilde{M}_m^\top$, $\dot{\tilde{M}}_m = 0$) and M_a (*added mass matrix*). The general expression of $\tilde{M}_m$ might be complicated, but assuming that body frame is centered on the CG of the vehicle and that the body-fixed frame axes coincide with the principal axes

of inertia, $\tilde{M}_m$ becomes:

$$\tilde{M}_m = \begin{bmatrix} \text{diag}\{m, m, m\} & 0_{3\times3} \\ 0_{3\times3} & \text{diag}\{I_x, I_y, I_z\} \end{bmatrix}, \tag{3.12}$$

where the operator diag$\{\bullet\}$ denotes a diagonal whose diagonal elements are the terms inside the braces (obviously the matrix dimension is $i \times i$ with i is the total number of items enclosed in braces), m is the mass of the vehicle, and I_x, I_y, I_z are the principal moments of inertia (respectively about surge, sway, and heave axes).

According to [Fossen et al., 1994], added mass can be understood as forces and moments induced by the motion of the vessel body proportional to its acceleration. Briefly speaking, any motion of the AUV will produce motion in the surrounding fluid; hence, the fluid motion possesses kinetic energy that it would lack otherwise. This phenomenon is experienced as an additional inertia when the vehicle, and therefore the surrounding fluid, accelerates. A generic added mass force (torque) A along (about) a generic a-axis generated by an acceleration $\dot{b}$ along (about) the respective axis is $-A_{\dot{b}}\dot{b}$, where $A_{\dot{b}} = \frac{\partial A}{\partial \dot{b}}$. The general expression of M_a presents 36 parameters but, as stated in [Newman, 2018], for a rigid-body at rest approximately at rest condition and under the assumption of an ideal fluid, no incident waves, no sea currents, and zero frequency, the hydrodynamic system $M_a = M_a^\top > 0$ holds, where with > 0 is indicated a positive definite matrix. Moreover, for an underwater vehicle moving at low speed and with three planes of symmetry, the contribution from the off-diagonal elements can be often neglected. As a consequence, M_a becomes:

$$M_a = -\,\text{diag}\left\{X_{\dot{u}}, Y_{\dot{v}}, Z_{\dot{w}}, K_{\dot{p}}, M_{\dot{q}}, N_{\dot{r}}\right\}, \tag{3.13}$$

where the SNAME notation is employed for forces, torques, and accelerations. To clarify, $X_{\dot{u}}$ is a force experienced along the body x-axis due to an acceleration $\dot{u}$ that, according to SNAME notation, is the acceleration along the body x-axis. The minus sign is related to the fact that $A_{\dot{b}}$ is defined with A as the action on the vehicle produced by the fluid. Let us consider $X_{\dot{u}} = \frac{\partial X}{\partial \dot{u}}$, for positive values of $\dot{u}$, the fluid interaction increases in absolute value with an action opposite to the motion of the vehicle (for almost all applications). Hence, $X_{\dot{u}}$ will be negative and the final action $-X_{\dot{u}}\dot{u}$,

experienced as added mass, will be positive.

Centripetal and Coriolis effects matrix $C(\boldsymbol{\nu})$

$C(\boldsymbol{\nu})$ is constituted of two terms:

$$C(\boldsymbol{\nu}) = \tilde{C}(\boldsymbol{\nu}) + C_a(\boldsymbol{\nu}), \tag{3.14}$$

where $\tilde{C}(\boldsymbol{\nu})$ is due to centripetal and Coriolis effects and $C_a(\boldsymbol{\nu})$ takes into account the motion of the vehicle within the fluid. Under the same hypotheses made for M_m, it can be shown that, contrary to $\tilde{M}_m$, $\tilde{C}(\boldsymbol{\nu})$ posses a large number of representations, for example see Eq.3.15.

$$\tilde{C}(\boldsymbol{\nu}) = \begin{bmatrix} 0 & -mr & mq & 0 & 0 & 0 \\ mr & 0 & -mp & 0 & 0 & 0 \\ -mq & mp & 0 & 0 & 0 & 0 \\ 0 & 0 & 0 & 0 & I_z r & -I_y q \\ 0 & 0 & 0 & -I_z r & 0 & I_x p \\ 0 & 0 & 0 & I_y q & -I_x p & 0 \end{bmatrix} \tag{3.15}$$

Moreover, $C_a(\boldsymbol{\nu})$ can be expressed as follows:

$$C_a(\boldsymbol{\nu}) = \begin{bmatrix} 0 & 0 & 0 & 0 & -Z_{\dot{w}} w & -Z_{\dot{w}} w \\ 0 & 0 & 0 & Z_{\dot{w}} w & 0 & 0 \\ 0 & 0 & 0 & 0 & 0 & 0 \\ 0 & -Z_{\dot{w}} w & 0 & 0 & I_z r & -I_y q \\ Z_{\dot{w}} w & 0 & 0 & -I_z r & 0 & I_x p \\ 0 & 0 & 0 & I_y q & -I_x p & 0 \end{bmatrix} \tag{3.16}$$

Hydrodynamic damping effects matrix $D(\boldsymbol{\nu})$

For what concerns underwater vehicles, $D(\boldsymbol{\nu})$ is mainly due to vortex shedding and to the so-called skin friction that depends upon laminar and/or turbulent boundary layer. For a generic rigid-body moving through an ideal fluid $D(\boldsymbol{\nu})$ is real non-symmetric and

$$D(\boldsymbol{\nu}) > 0, \forall \boldsymbol{\nu} \in \mathbb{R}^6 \tag{3.17}$$

holds true. Moreover, $D(\boldsymbol{\nu})$ can be highly nonlinear. For an underwater vehicle moving at low speed, $D(\boldsymbol{\nu})$ is often assumed as diagonal with quadratic damping terms only (see Eq.3.18). More information concerning its estimation, as well as a mixed linear-quadratic damping model, is presented in Section 4.2.2.

$$D(\boldsymbol{\nu}) = -\operatorname{diag}\left\{X_{u|u|}|u|Y_{v|v|}|v|Z_{w|w|}|w|K_{p|p|}|p|M_{q|q|}|q|N_{r|r|}|r|\right\} \tag{3.18}$$

For the sake of clarity, it is worth noting that at very low speed linear damping brings instead the major contribution.

Gravitational and buoyancy effects vector $\boldsymbol{g_\eta}(\boldsymbol{\eta})$

In addition to damping forces, gravitational and buoyancy effects act on underwater vehicles. In particular,

$$^N\boldsymbol{W} = \begin{bmatrix} 0 \\ 0 \\ mg \end{bmatrix}, \tag{3.19}$$

where m is the dry mass of the vehicle, $g = 9.806$ m/s^2 is the gravitational acceleration and it is worth noting that the gravitational effects act through the CG.

$$^N\boldsymbol{B} = -\begin{bmatrix} 0 \\ 0 \\ \rho g V \end{bmatrix}, \tag{3.20}$$

where V denote the total volume of the vehicle, ρ is the water density and it is worth noting that the buoyancy effects act through the CB that usually does not coincide with the CG. Reporting the quantities in the body-fixed frame:

$$^b\boldsymbol{W} = (^N R_b^N)^\top (^N\boldsymbol{W}) \tag{3.21}$$

$$^b\boldsymbol{B} = (^N R_b^N)^\top (^N\boldsymbol{B}) \tag{3.22}$$

Let us suppose that $^b\boldsymbol{r}_b$ is the position of the CB, so the vector $\boldsymbol{g_\eta}(\boldsymbol{\eta})$ can be expressed as follows ($\times$ is the cross product and it is assumed again that

the body frame is centered in the CG):

$$ {}^{b}\boldsymbol{g}_{\boldsymbol{\eta}}(\boldsymbol{\eta}) = - \begin{bmatrix} {}^{b}\boldsymbol{W} + {}^{b}\boldsymbol{B} \\ {}^{b}\boldsymbol{r}_{b} \times {}^{b}\boldsymbol{B} \end{bmatrix}, \tag{3.23} $$

3.2 The Unscented Kalman Filter

It is well known that a dynamical system can be described by means of a set of variables that completely characterize its *state*. Knowing the components of this state means a complete description of the system. It is worth noting that the definition of the system *state* is not unique, usually suggested from basic physical hypotheses. Generally speaking, the evolution of a system is described by a nonlinear time-varying equation of the form:

$$ \dot{\boldsymbol{x}}(t) = \boldsymbol{f}(t, \boldsymbol{x}(t), \boldsymbol{u}(t)), \tag{3.24} $$

where $\boldsymbol{x}(t) \in \mathbb{R}^n$ is the state vector, $\boldsymbol{f}(\bullet)$ a generic nonlinear, time-varying function, and $\boldsymbol{u}(t) \in \mathbb{R}^m$ is a vector of controlled inputs.

Generally speaking, the physical laws that describe the process are partially known, or a full description might be too complicated, and thus $\boldsymbol{f}(\bullet)$ only tries to give a model for the system behavior. As a consequence, a vector $\boldsymbol{w}(t) \in \mathbb{R}^n$ is used to consider system uncertainty. Hence, Eq.3.24 becomes Eq.3.25.

$$ \dot{\boldsymbol{x}}(t) = \boldsymbol{f}(t, \boldsymbol{x}(t), \boldsymbol{u}(t), \boldsymbol{w}(t)), \tag{3.25} $$

The direct knowledge of the system state might be unavailable and, a set of measurements, usually called *observations* are usually present. A generic *measurement equation* can be described with the following vector equation:

$$ \boldsymbol{y}(t) = \boldsymbol{h}(t, \boldsymbol{x}(t), \boldsymbol{u}(t)), \tag{3.26} $$

where $\boldsymbol{y}(t) \in \mathbb{R}^p$ is the state vector, and $\boldsymbol{h}(\bullet)$ a generic nonlinear, time-varying function, and $\boldsymbol{u}(t) \in \mathbb{R}^m$ is a vector of controlled inputs. As before, a vector $\boldsymbol{v}(t) \in \mathbb{R}^p$ is used with the aim of considering uncertainties. Hence, Eq.3.26 becomes Eq.3.27.

$$ \boldsymbol{y}(t) = \boldsymbol{h}(t, \boldsymbol{x}(t), \boldsymbol{u}(t), \boldsymbol{v}(t)), \tag{3.27} $$

The dependence upon the input is possible but rarely verified in real applications. For example, a real resistor modeled with a pure resistance falls in this case, but it is well known that modeling a real resistor with only resistance is a rough assumption. In the following, strictly casual systems will be considered.
For the ease of reading, explicit dependence on time t of the function arguments will be omitted in the following.
The above treatment is true for *continuous systems* (the time $t \in \mathbb{R}$), so it is useful to introduce a discrete-time representation of Eq.3.25 and Eq.3.27. In the following, a treatment valid for a uniform sampling with respect to time (*sampling time*), which will be employed in the rest of the thesis, is proposed.

$$\begin{cases} \boldsymbol{x}_k = \boldsymbol{f}_{k-1}\left(\boldsymbol{x}_{k-1}, \boldsymbol{u}_{k-1}, \boldsymbol{w}_{k-1}\right) \\ \boldsymbol{y}_k = \boldsymbol{h}_k\left(\boldsymbol{x}_k, \boldsymbol{v}_k\right) \end{cases} \tag{3.28}$$

where k denotes the iteration number.
Suitable estimators of the system state are thus required to obtain a reliable estimation of the system behavior (the system state). The majority are based on the Bayesian statistics and in particular on the KF [Kalman, 1960] or its extension EKF [Bar-Shalom et al., 2004] or UKF [Julier and Uhlmann, 2004], usually employed when system non-linearities arise.
The basic idea behind the KF or its variants lies on two steps:

- *prediction*: where the behavior of the system at the subsequent iteration is predicted exploiting the current estimate and the model;
- *update*, also called *correction*: where, to improve the state estimate, the predicted state is corrected using available measurements.

During the Ph.D. period, the UKF-based navigation filter position estimation of an AUV, already developed and validated by the UNIFI DIEF, has been further enhanced to manage speed measurements from the FLS and to adapt on line its noise statistics. Therefore, its structure and main features are described here below.
The Unscented Transform (UT), a deterministic sampling technique that allows the computation of the mean and the covariance matrix of a Random Variable (RV) that propagates through a generic nonlinear transformation, is the foundation of the UKF. In particular, according to [Uhlmann, 1994],

the UT is based on the following idea: *it is easier to approximate a probability distribution than it is to approximate an arbitrary nonlinear function or transformation.* Let us suppose that $\boldsymbol{a} \in \mathbb{R}^{n_a}$ is a RV with mean $\overline{\boldsymbol{a}} \in \mathbb{R}^{n_a}$ and covariance $P_a \in \mathbb{R}^{n_a \times n_a}$, and let us suppose that $\boldsymbol{b} = \boldsymbol{g}(\boldsymbol{a}) \in \mathbb{R}^{n_b}$ denote the RV obtained propagating through the nonlinear function $\boldsymbol{g}(\bullet) : \mathbb{R}^{n_a} \rightarrow \mathbb{R}^{n_b}$. It is well known that, by definition of mean and covariance of a RV with probability distribution $p(\bullet)$ that undergoes a generic nonlinear transformation $\boldsymbol{g}(\bullet)$ is:

$$E[\boldsymbol{g}(\boldsymbol{x})] = \int_{\mathcal{X}} \boldsymbol{g}(\boldsymbol{x}) p(\boldsymbol{x}) d\boldsymbol{x}, \tag{3.29}$$

$$Var[\boldsymbol{g}(\boldsymbol{x})] = \int_{\mathcal{X}} [\boldsymbol{g}(\boldsymbol{x}) - E[\boldsymbol{g}(\boldsymbol{x})]][\boldsymbol{g}(\boldsymbol{x}) - E[\boldsymbol{g}(\boldsymbol{x})]]^{\top} p(\boldsymbol{x}) d\boldsymbol{x}, \tag{3.30}$$

where $E[\bullet]$ is the expectation, and $\mathcal{X}$ is the domain of $\boldsymbol{x}$. Unfortunately, generally speaking, solving Eq.3.29 and Eq.3.30 is not always feasible. The UT of the RV $\boldsymbol{a}$ is indicated with $UT(\overline{\boldsymbol{a}}, P_a, \boldsymbol{g}(\bullet))$ and it can be obtained as follows:

- first of all, it is worth noting that the minimum number of samples required to produce the mean $\overline{\boldsymbol{a}}$ and the covariance P_a (and therefore used to approximate the distribution of $\boldsymbol{a}$) is $n_a + 1$ ([Julier and Uhlmann, 2004]). In the following, the samples are called σ-points, each one with the dimension of $\in \mathbb{R}^{n_a}$. The choice of the σ-points is not unique and a quite general form, as proposed in [Wan et al., 2001], is presented.
  According to [Wan et al., 2001], $2n_a + 1$ σ-points $\boldsymbol{\mathcal{X}}_i$, each one $\in \mathbb{R}^{n_a}$ (column vectors), with $i = 0, ..., 2n_a$ are generated. These σ-points are put together in the matrix $\mathcal{X} \in \mathbb{R}^{n_a \times 2n_a + 1}$ as follows:

$$\begin{aligned} \boldsymbol{\mathcal{X}}_0 &= \overline{\boldsymbol{a}} \\ \boldsymbol{\mathcal{X}}_i &= \overline{\boldsymbol{a}} + \left(\sqrt{(n_a + \lambda) P_a}\right)_i, \qquad i = 1, \ldots, n_a \\ \boldsymbol{\mathcal{X}}_i &= \overline{\boldsymbol{a}} - \left(\sqrt{(n_a + \lambda) P_a}\right)_{i - n_a}, \quad i = n_a + 1, \ldots, 2n_a \end{aligned} \tag{3.31}$$

  where $\lambda = \alpha^2 (n_a + \kappa) - n_a \in \mathbb{R}$ is a scaling parameter. According to [Wan et al., 2001], $\alpha \in \mathbb{R}$ regulates the spread of the sigma points around $\overline{\boldsymbol{a}}$ and its standard values are in the interval $10^{-4} \leq \alpha \leq 1$.

$\kappa \in \mathbb{R}$ is another parameter, often set to $3 - n_a$ (see [Julier et al., 1995]).

- σ-points are propagated through the function $\boldsymbol{g}(\bullet)$

$$\boldsymbol{\mathcal{G}}_i = \boldsymbol{g}\left(\boldsymbol{\mathcal{X}}_i\right) \in \mathbb{R}^{n_b} i = 0, \ldots, 2n_a \tag{3.32}$$

- the mean $\boldsymbol{b}$, the covariance P_a and the cross-covariance P_{ab} are obtained as follows:

$$\overline{\boldsymbol{b}} = \sum_{i=0}^{2n_a} W_i^{(m)} \boldsymbol{\mathcal{G}}_i \tag{3.33}$$

$$P_b = \sum_{i=0}^{2n_a} W_i^{(c)} (\boldsymbol{\mathcal{G}}_i - \overline{\boldsymbol{b}})(\boldsymbol{\mathcal{G}}_i - \overline{\boldsymbol{b}})^\top, \tag{3.34}$$

where $W_i^{(m)} \in \mathbb{R}$ and $W_i^{(c)} \in \mathbb{R}$ are the weights to compute the mean and the variance, respectively. In particular, according to [Wan et al., 2001],

$$W_0^{(m)} = \frac{\lambda}{n_a + \lambda} \tag{3.35}$$

$$W_0^{(c)} = \frac{\lambda}{n_a + \lambda} + 1 - \alpha^2 + \beta, \tag{3.36}$$

$$W_i^{(m)} = W_i^{(c)} = \frac{1}{2(n_a + \lambda)}, \tag{3.37}$$

where for Gaussian distributions $\beta = 2$ is optimal. The solution used in the rest of the work employs $\alpha = 1$, $\kappa = 0$ (and thus $\lambda = 0$), and $\beta = 2$.

The UT is the foundation of the UKF. When nonlinearities arise in the state evolution and/or in the measurement function, UT is used to propagate a RV through a generic nonlinear transformation. Assuming additive noise ($\boldsymbol{w}$ and $\boldsymbol{v}$) with zero-mean, white Gaussian distribution, an implementation of the UKF algorithm is presented in Algorithm 1: $\hat{\boldsymbol{x}}$ is an estimate, P is the state covariance, Q is the process noise and R is the measurement noise, and $\left(\hat{\boldsymbol{x}}_{0|0}, P_{0|0}\right)$ is the initial guess for the state and state covariance, where the subscript $_{j|k}$ stands for "at iteration j given information up to the k-th iteration."

A brief discussion on the mathematical modeling of sensors and instruments

Algorithm 1 UKF Algorithm

Algorithm:

Function `UKF() /* Algorithm implementation */`

  Step `Prediction() /* Prediction step */`

    Input : $\hat{\boldsymbol{x}}_{k-1|k-1}, P_{k-1|k-1}, \boldsymbol{f}(\bullet)_{k-1}$

    Output: $\hat{\boldsymbol{x}}_{k|k-1}, P_{k|k-1}$

    $(\hat{\boldsymbol{x}}_{k|k-1}, \overline{P}_{k|k-1}) = UT(\hat{\boldsymbol{x}}_{k-1|k-1}, P_{k-1|k-1}, \boldsymbol{f}(\bullet)_{k-1})$

    $P_{k|k-1} = \overline{P}_{k|k-1} + Q_{k-1}$

  end

  Step `Correction() /* Correction step */`

    Input : $\hat{\boldsymbol{x}}_{k|k-1}, P_{k|k-1}, \boldsymbol{h}(\bullet)_k$

    Output: $\hat{\boldsymbol{x}}_{k|k}, P_{k|k}$

    $(\hat{\boldsymbol{y}}_{k|k-1}, \overline{S}_k, P_k^{xy}) = UT(\hat{\boldsymbol{x}}_{k|k-1}, P_{k|k-1}, \boldsymbol{h}(\bullet)_k)$

    $S_k = \overline{S}_k + R_k$

    $L_k = P_k^{xy} S_k^{-1}$

    $\boldsymbol{\mu}_k = \boldsymbol{y}_k - \hat{\boldsymbol{y}}_{k|k-1}$

    $\hat{\boldsymbol{x}}_{k|k} = \hat{\boldsymbol{x}}_{k|k-1} + L_k \boldsymbol{e}_k$

    $P_{k|k} = P_{k|k-1} - L_k S_k L_k^\top$

  end

end

that are typically employed in marine robotics for autonomous navigation is presented in Appendix A.

3.3 2D FLS imaging model and phase correlation technique

The acoustic insonification of the scene can be summarized upon three parameters: the azimuth angle (α), the elevation angle (β), and the delivering range ($R_\rightarrow$). The return of acoustic waves continuously spanned along the FLS Field Of View (FOV) is acquired by an array of transducers. The physics of the transducers, given a particular range and bearing value, does not permit to retrieve where, along the elevation angle, the acoustic return comes from. In other words, the 3D information of the insonificated scene is lost [Hurtós Vilarnau, 2014].

The area covered by an FLS that insonifies the sea bottom can be described using spherical coordinates $(R_\rightarrow, \alpha, \beta)$. Let us assume a reference frame $\left\{O^{FS} x^{FS} y^{FS} z^{FS}\right\}$ centered on the FLS center with the x-axis pointing for-

ward, the z-axis pointing down and the y-axis that completes a right-handed reference frame.
Obviously, the position and orientation of the FLS with respect to the $\{O^b x^b y^b z^b\}$ frame can be represented as follows (see Eq.3.38).

$$A_{FS} = \begin{pmatrix} {}^b R^b_{FS} & {}^b\boldsymbol{p_{FS}} \\ \boldsymbol{O}^\top & 1 \end{pmatrix}, \tag{3.38}$$

where ${}^b R^b_{FS}$ is the matrix between the FLS and the body reference system and ${}^b\boldsymbol{p_{FS}}$ is the position of the FLS with respect to the CG expressed in the $\{O^b x^b y^b z^b\}$ frame. In the following, with the uppercase will be indicated a 3D point, whereas with the lowercase the same 3D point is projected on the image plane. The coordinates of a generic 3D point ${}^{FS}\boldsymbol{P} \in \mathbb{R}^3$ in the $\{O^{FS} x^{FS} y^{FS} z^{FS}\}$ reference system, expressed in spherical coordinates, are (see Fig.3.2):

$${}^{FS}\boldsymbol{P} = \begin{bmatrix} X \\ Y \\ Z \end{bmatrix} = \begin{bmatrix} R_{\rightarrow} \cos\alpha \cos\beta \\ R_{\rightarrow} \sin\alpha \cos\beta \\ R_{\rightarrow} \sin\beta \end{bmatrix} \tag{3.39}$$

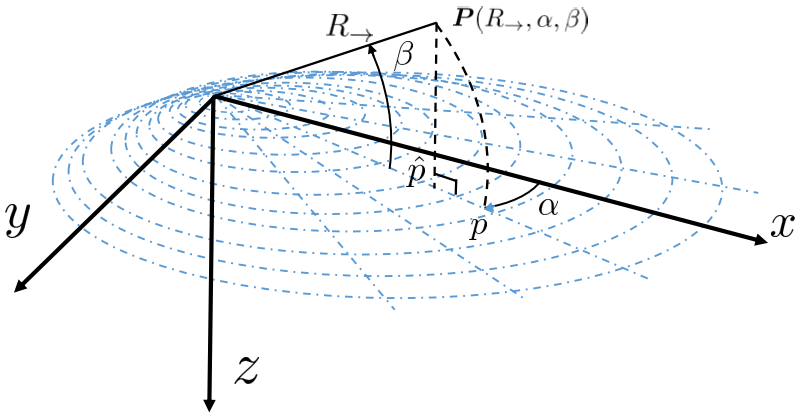

Figure 3.2: The imaging model of an FLS.

The nonlinear model that projects a 3D point ${}^{FS}\boldsymbol{P}$ on the point ${}^{FS}\boldsymbol{p}$ belonging to the image plane is:

$${}^{FS}\boldsymbol{p} = \begin{bmatrix} x \\ y \end{bmatrix} = \begin{bmatrix} R_{\rightarrow} \cos\alpha \\ R_{\rightarrow} \sin\alpha \end{bmatrix} = \frac{1}{\cos\beta} \begin{bmatrix} X \\ Y \end{bmatrix}. \tag{3.40}$$

More information can be found in [Walter, 2008] and [Negaharipour, 2012]. An image in the spatial domain is indicated with the lowercase $i(x, y)$, whereas an image in the Fourier domain is expressed with the uppercase $I(m, n)$. An image collected at a certain absolute time $t_i \in \mathbb{R}$ is defined as $i_{t_i}(x, y)$ or $I_{t_i}(m, n)$ in the spatial and the Fourier domains, respectively, where $I_{t_i}(m, n) = \mathcal{F}\{i_{t_i}(x, y)\}$ and with $\mathcal{F}$ is denoted the Fourier Transform (FT).

The phase correlation algorithm (or its variants), which is a Fourier-based method, ([De Castro and Morandi, 1987] and [Reddy and Chatterji, 1996]), has been widely use for registration of roto-translated optical images over the years, such as in [Ojansivu and Heikkila, 2007], [Li et al., 2007] [Tzimiropoulos et al., 2010] or [Eustice et al., 2002], [Bulow et al., 2009], and [Pfingsthorn et al., 2010] in the underwater domain; differently, its use in SONAR imagery is less prevalent. In [Bülow et al., 2010] the phase correlation method has been used with 2D SONAR range scans, whereas, with regard to FLS applications, remarkable contribution can be found in [Hurtós et al., 2015], and in the author's work [Franchi et al., 2019a]. The key concept is based on the so-called Fourier shift property. In the Fourier domain, a shift between two functions (*e.g.*, images) appears as a linear phase shift. Given two images $i_{t_1}(x, y)$ and $i_{t_2}(x, y)$ with $t_1 < t_2$, let us suppose that $i_{t_2}(x, y)$ is a translated and rotated replica of $i_{t_1}(x, y)$

$$\begin{aligned} i_{t_1}(x, y) = i_{t_2}(&x \cos\theta_0 + y \sin\theta_0 - s_x, \\ &- x \sin\theta_0 + y \cos\theta_0 - s_y), \end{aligned} \tag{3.41}$$

where $s_x \in \mathbb{R}$ and $s_y \in \mathbb{R}$ are the translation, which can be put together in $\boldsymbol{s} = \begin{bmatrix} s_x \\ s_y \end{bmatrix} \in \mathbb{R}^2$ and $\theta_0 \in \mathbb{R}$ is the rotation angle.
Their FT is

$$\begin{aligned} I_{t_1}(m, n) = &e^{-j2\pi(ms_x + ns_y)} I_{t_2}(m \cos\theta_0 + n \sin\theta_0, \\ &- m \sin\theta_0 + n \cos\theta_0). \end{aligned} \tag{3.42}$$

When pure translations are considered ($\theta_0 = 0$, see Eq.3.43), Eq.3.42 becomes Eq.3.44.

$$i_{t_1}(x, y) = i_{t_2}(x - s_x, y - s_y), \tag{3.43}$$

$$I_{t_1}(m,n) = e^{-j2\pi(ms_x+ns_y)} I_{t_2}(m,n). \tag{3.44}$$

In this case, from Eq.3.44, the normalized cross-power spectrum is

$$C(m,n) = \frac{I_{t_1}(m,n) I^*_{t_2}(m,n)}{\left| I_{t_1}(m,n) I^*_{t_2}(m,n) \right|} = e^{-j2\pi(ms_x+ns_y)}, \tag{3.45}$$

where * denotes the complex conjugate. It is easy to note that the inverse FT of Eq.3.45 (reported in Eq.3.46) is a 2D Dirac function centered on $\boldsymbol{s}$ and its location can be found with Eq.3.47.

$$c(x,y) = \mathcal{F}^{-1}\{C(m,n)\} \tag{3.46}$$

$$\boldsymbol{s} = \begin{bmatrix} s_x \\ s_y \end{bmatrix} = \arg\max_{(x,y)}\{c(x,y)\} \tag{3.47}$$

In conclusion, by solving Eq.3.47, the location of the peak of the cross-power spectrum in Eq.3.45 can be obtained, and therefore the translation $\boldsymbol{s}$ between $i_{t_1}(x,y)$ and $i_{t_2}(x,y)$ found (see Eq.3.43).
With regard to rotation estimation, one of the most popular methods is the so-called Fourier-Mellin transform [Chen et al., 1994], and [Reddy and Chatterji, 1996], which is employed to estimate both rotations and scale changes; in the following, because the absence of scale ambiguities in FLS images, rotation estimations only are described. Eq.3.42 can be rewritten in terms of magnitude as:

$$M_{t_1}(m,n) = M_{t_2}(m\cos\theta_0 + n\sin\theta_0, -m\sin\theta_0 + n\cos\theta_0), \tag{3.48}$$

where M denotes the magnitude of I. It is trivial to note that one magnitude is a rotated replica of the other. Eq.3.48 can be represented using polar coordinates as:

$$M_{t_1}(r,\theta) = M_{t_2}(r,\theta-\theta_0), \tag{3.49}$$

Similarly to translation estimations, rotational movements can be therefore retrieved by employing the phase correlation algorithm to the polar representation of the Fourier transform magnitudes. Rotation estimation is then converted to a shift estimation problem.

In the rest of the thesis, because of the digital nature of the images involved, the discrete case of the FT is employed. More information regarding phase correlation applied to discrete case with subpixel translation estimation can be found in [Foroosh et al., 2002], and [Alba et al., 2015].

Chapter 4

Main contributions

This chapter concerns the navigation framework developed during the Ph.D. period. Exploiting the research background of the UNIFI DIEF in underwater navigation, the same filter architecture proposed in [Costanzi et al., 2016] and [Fanelli, 2019] where attitude is estimated independently by means of IMU, compass, and FOG data, is adopted. Here, the output of the attitude estimator (namely roll, pitch, yaw angle, and their derivatives) is used as input for the position estimation filter. If, on the one hand, it was decided not to spoil the above-mentioned structure that has proven to be satisfyingly reliable, on the other hand, the "old" solution has been augmented in order to embed, within the position filter estimator, FLS measurements. This is clearly shown in Fig.4.1.
In addition to this, the dynamic description of an AUV has been enhanced: the surge damping model has been made suitable for an online estimation, and the propulsion system model has been further investigated. Moreover, in order to better the performance of the navigation filter, the UKF-based estimator proposed by UNIFI DIEF research group (see [Allotta et al., 2016b], [Costanzi et al., 2019], and [Fanelli, 2019],) has been improved, proposing an AUKF solution.
The overall situation is depicted in Fig.4.2.

In conclusion, this work is proposed to cover heterogeneous fields: from how to retrieve the vehicle motion from an FLS (for navigation-aiding purposes Section 4.1 or for 2D acoustic mapping Appendix A), to how to identify some of the parameters involved in the AUV dynamics (see Section 4.2.2)

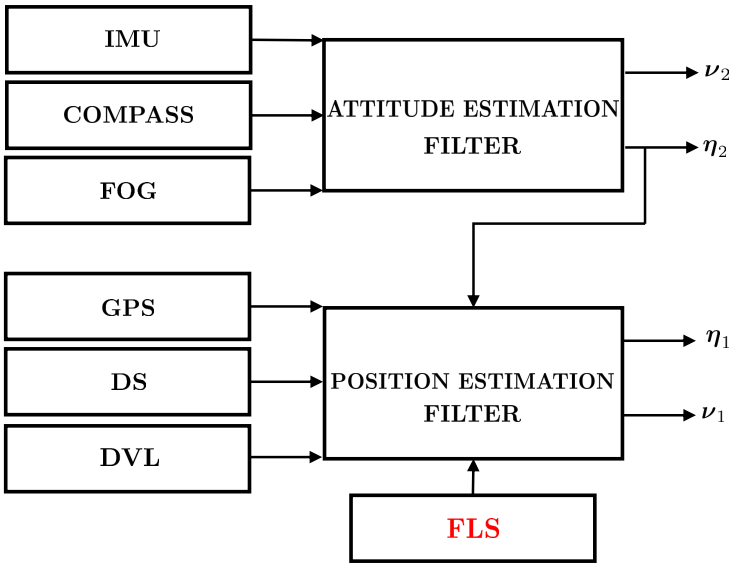

Figure 4.1: Block scheme of the proposed navigation strategy. The attitude estimation filter can be found in [Costanzi et al., 2016] and [Fanelli, 2019].

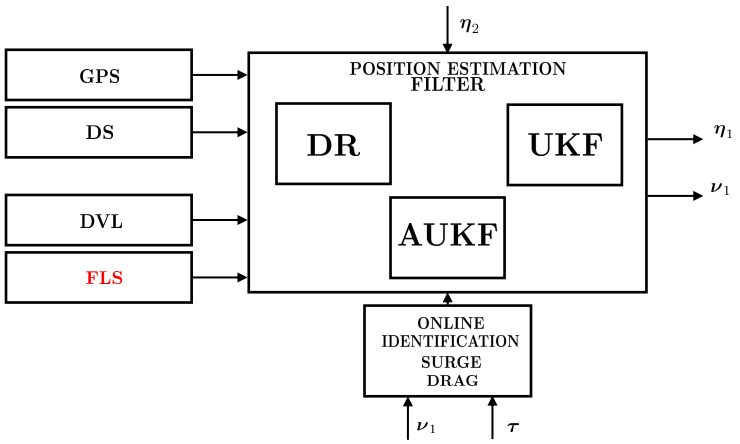

Figure 4.2: Block scheme of the proposed position estimation filter. It can be a DR version, an UKF, or an AUKF one. The drag can be identified online.

as well as to deal with a propulsion model when the knowledge of the rotational speed of the motor is limited to the command drive (see Section 4.2.1). Lastly, the proposed AUKF estimator is described in Section 4.3. In a few words, the intent was to enhance the state-of-the-art in underwater navigation and mapping at the UNIFI DIEF, integrating an FLS as percep-

tual sensor.
Before starting, it is worth describing the principal assumptions on which this work is based. Most of them concern approximations in the dynamic description of the AUV (assumptions 1 - 5), which ultimately affect the modeling part of the estimator proposed in Section 4.3, whereas others are related to FLS operations (assumption 6 - 8).

Assumption 1. *Most of the dynamics of the AUV take place in the longitudinal direction. In fact, the longitudinal direction is still that of minimal resistance. In order to reduce battery consumption, AUVs usually performs missions along the longitudinal direction.*

Assumption 2. *The body reference frame* $\{O^b x^b y^b z^b\}$ *is supposed to be centered on the CG and aligned with the vehicle principal axes of inertia. Hence, the mass matrix* M_m *can be considered as diagonal.*

Assumption 3. *The maximum speed of the vehicles of the UNIFI DIEF MDM Lab fleet is not too high— around 1 m/s—thus, the coupling between the dissipative effects can be neglected, leading to a diagonal damping matrix* $D(\boldsymbol{\nu})$.

Assumption 4. *Gravitational* $\boldsymbol{g_\eta}(\boldsymbol{\eta})$*, centripetal and Coriolis effects* $C(\boldsymbol{\nu})$ *have been neglected, added masses are not considered. Sea currents are hypothesized to be small.*

The vehicle is supposed approximately neutrally buoyant with CG and CB roughly located vertically on the z^b axis. In such a situation, $\boldsymbol{g_\eta}(\boldsymbol{\eta})$ is approximated to the null vector. Underwater missions, for the most part, are composed of phases within which the vehicle moves forward at an approximately constant speed (or at least rotations and jerky motions are minor). As a consequence, under this assumption, centripetal and Coriolis contribution is usually numerically negligible (the rotational speed of an AUV is typically very low), and added masses do not produce any sensible effect. In addition to this, generally, *i.e.* to correctly perform autonomous missions, the absolute speed of the viscous fluid is much smaller than the speed of the AUV relative to the viscous fluid. Therefore, the former can be neglected. Assumptions 1 - 4 are similar to the ones made by the authors in [Allotta et al., 2016b].

Hence, the classic dynamic description of [Fossen et al., 1994] and reported in Eq.3.10 can be simplified, for the longitudinal motion, with Eq.4.1.

$$m\dot{\nu}_{1x} = m\dot{u} = \tau_{1x}(\boldsymbol{\nu}, \boldsymbol{u}_{rpm}) + F_1(\boldsymbol{\nu}). \tag{4.1}$$

In the case of quadratic damping model, $F_1(\boldsymbol{\nu})$, obtained from the dynamic model in [Fossen et al., 1994], can be further simplified with the aim of reducing the number of parameters:

$$F_1(\boldsymbol{\nu}) = -\frac{A_f C_u \rho \nu_{1x}^2 \operatorname{sgn}(\nu_{1x})}{2}, \tag{4.2}$$

where m is the mass of the vehicle, ρ is the density of the water, A_f is the frontal area of the vehicle, and C_u is the drag along the surge axis.

Assumption 5. *The four-quadrant motor characteristic is approximated with*

$$\begin{aligned} T_i(\boldsymbol{\nu}, u_{rpm_i}) = \\ = \operatorname{sgn}(u_{rpm_i})(k u_{rpm_i}^2 - \frac{k|u_{rpm_i}| g(\operatorname{sgn}(u_{rpm_i}) V_{a,i})}{p_p}), \end{aligned} \tag{4.3}$$

where i refers to the $i-th$ motor and

$$g(x) = \begin{cases} 0 & \text{for } x \leq 0 \\ x & \text{for } 0 < x \leq |u_{rpm_i}|\, p_p \\ |u_{rpm_i}|\, p_p & \text{for } x > |u_{rpm_i}|\, p_p \end{cases} \tag{4.4}$$

, and where p_p is the propeller pitch (a construction parameter), k is a coefficient that relates motor thrust and propeller speed at bollard conditions (i.e. when the advance speed $V_{a,i} = 0$), see Eq.4.6, and $V_{a,i}$, which is the speed of the $i-th$ motor, can be expressed as a function of the speed vector $\boldsymbol{\nu}$:

$$V_{a,i} = {}^b\boldsymbol{n}_{mi}^T \left[{}^b\boldsymbol{\nu_1} + {}^b\boldsymbol{\nu_2} \times \left({}^b\boldsymbol{P}_{mi} - {}^b\mathbf{0} \right) \right] \tag{4.5}$$

$$k = \left. \frac{T(\boldsymbol{\nu}, u_{rpm})}{u_{rpm}^2} \right|_{V_{a,i}=0} \tag{4.6}$$

It is worth noting that when the propeller pitch $p_p \to 0$, Eq.4.3 is not defined. However, such propellers are not present in the market; indeed, the

linear momentum of the fluid would not be modified, thus not producing a motion. Assumption 5 has been already exploited by the authors in [Allotta et al., 2016a] and further information can be found in [Pivano et al., 2009], and [Carlton, 2012]. A more sophisticated description is presented in Section 4.2.1.

Assumption 6. *Roll and pitch variations are limited and can be neglected.*

For vehicles such as FeelHippo AUV, roll and pitch dynamics cannot be actively controlled, but their variations are limited by hydrostatic stability. However, when roll and pitch can be controlled, such as for Zeno AUV, typical autonomous missions do not excite these DOFs. Indeed, significant roll changes might show instability, whereas pitch ones are usually not necessary. Assumption 6 is used to take advantage of a simpler projection model for the FLS, as it can be shown in the following. If roll and pitch variations are consistent, a tilt unit can be employed to maintain the FLS to an approximately desired configuration.

Assumption 7. *The FLS, which is mounted on the bow of the vehicle, is positioned approximately parallel with respect to the sea bottom that is supposed not to change abruptly in order to insonify wider areas.*

Assumption 8. *The elevation angle β (around 7°-10° for most of the typical FLS devices) can be considered small.*

Assumptions 7 and 8 make possible to take advantage of a 2D approximated model instead of a complete non-linear projection model (see Eq.3.40). In other words, the projection ${}^{FS}\boldsymbol{p}$ is substituted with the orthogonal projection ${}^{FS}\hat{\boldsymbol{p}}$ as reported in Fig.3.2; thus, Eq.3.40 becomes Eq.4.7.

$$ {}^{FS}\hat{\boldsymbol{p}} \approx \begin{bmatrix} 1 & 0 & 0 \\ 0 & 1 & 0 \end{bmatrix} \begin{bmatrix} \mathrm{X} \\ \mathrm{Y} \\ \mathrm{Z} \end{bmatrix} \tag{4.7} $$

A similar proposal can be found, in [Ferreira et al., 2014], [Ferreira et al., 2015], [Hurtós et al., 2015] and has been already exploited by the author in [Franchi et al., 2018], and [Franchi et al., 2019a].
In light of the proposed imaging model, and neglecting roll and pitch variations (see Assumption 6), it can be seen that a 3-parameters Euclidean

transformation (plane roto-translation) puts two different FLS views of the same object in relation (a demonstration can be found for example in [Walter, 2008]). Hence, Fourier-based methods (see Section 4.1) that are known to manage up to similarity transformations [De Castro and Morandi, 1987] can be employed.

4.1 Linear speed estimation from FLS

The critical process through which a pair of overlapped images, obtained from different viewpoints (namely two images that insonify a common region), are related to each other is called registration or, more specifically, pairwise registration. In the last decade, researches have tried to use feature detection methods both at pixel and region. However, the presence of stable and conspicuous features is necessary. Although computationally heavy, a phase correlation method (see Section 3.3), is the most suitable to face mutable underwater scenarios. To make this method work (it is worth noting that this consideration is not limited to phase correlation), it is necessary for an overlap between the images. Nevertheless, the magnitude of the minimum overlapping area cannot be known a priori. Indeed, it can depend upon the informative content of the insonified area. For example, an overlapping close to 100% can produce incorrect results if the sea bottom in uninformative; on the other hand, an overlap of about 50% can be sufficient if a rich environment is present. For FLS applications, remarkable contributions can be found in [Hurtós et al., 2013b], [Hurtós et al., 2015], where this method is employed in 2D acoustic mosaicing, and author's work in [Franchi et al., 2019a], which represents the foundation of the following treatment.

Here, the proposed solution is the core of the FLS-based linear speed estimation, and it can be divided into three steps. In the first step, raw FLS images are filtered and rotated in order to be pairwise aligned (Section 4.1.1). In the second, the linear translation between two subsequent FLS images is retrieved (Section 4.1.2). In the third step, the linear speed estimation is computed (Section 4.1.3).

4.1.1 Pre-filtering and alignment

For each step two subsequent raw FLS images (*e.g.* i_{t_1} and i_{t_2}) are collected together with their absolute acquisition times (*e.g.* t_1 and t_2).
The FLS is a device that intrinsically operates with polar variables (namely range $R_{\rightarrow}$ and bearing angle α in Fig.3.2), but when the raw acoustic image is created, it is usually represented in the Cartesian space. Therefore, a fan shape, clearly visible in Fig.4.3, arises. This particular fan-shaped image presents an abrupt transition between the actual image content (inside the fan) and the background (outside the fan). Thus, when the FT is applied to all the image content, frequency components not related to the real image content are inevitably introduced. To overcome this issue, the fan-shaped contour of FLS images is typically smoothed performing a windowing operation (see the right FLS image in Fig.4.3) before applying the FT. More information about windows function in the Fourier domain is presented, for example, in [Harris, 1978]. Smoothing the raw FLS image implies a slight loss in the image content (see the right FLS image in Fig.4.3). However, this seems not to have negatively affected the speed estimation method. From

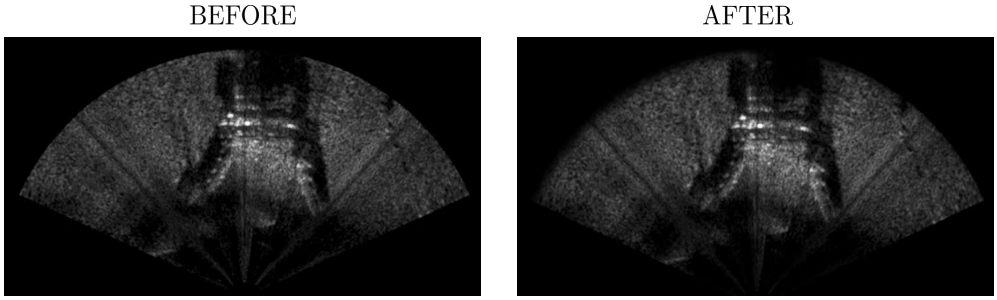

Figure 4.3: Image windowing procedure. Note the smooth contours on the second image, especially on the top arc.

Eq.3.41, it can be noted that rotations and translations (if both present) are coupled. Generally, it is well known that when quantities are coupled, it might be difficult to estimate them separately. In the current literature, several methods to address rotations between two images in the Fourier domain have been presented. Arguably, one of the most popular is the so-called Fourier-Mellin transform [Chen et al., 1994] and [Reddy and Chatterji, 1996], where rotational movement can be obtained using the phase correla-

tion on the magnitude spectrum of the Fourier transform (represented with polar coordinates). Although, this method has been extensively employed with optical images (see for example [Bulow et al., 2009], and [Pfingsthorn et al., 2010]) and with 2D SONAR range scans [Bülow et al., 2010], the conversion to polar coordinates of the magnitude spectrum of the FT is a non trivial problem [Averbuch et al., 2006], which can be further worsen from the typical noise present in FLS images [Hurtós et al., 2015]. When dealing with FLSs, other authors, such as [Hurtós et al., 2015], at the expense of a coupling between rotations and translational displacements, computed rotation estimation using the phase correlation in the spatial domain data represented in polar coordinates. Because of the importance of rotation evaluation, the author has decided to retrieve them not working on images but relying on specialized sensors and algorithms. That proposed by past Ph.D. students of the MDM Lab in [Costanzi et al., 2016], thoroughly explained in [Fanelli, 2019], and widely employed as the standard attitude estimator on board the AUVs of the UNIFI DIEF MDM Lab fleet has been used (see Fig.4.1). By knowing the location of the FLS, ${}^{b}\boldsymbol{p_{FS}}$ in Eq.3.38, the rotation center position of the AUV and the output of the above-mentioned attitude estimation filter, i_{t_1} can be rotated to be aligned with i_{t_2}. The situation is clearly depicted in Fig.4.4. It is worth highlighting that because the acoustic insonification of a scene can produce different results according to the relative attitude between the source (the FLS) and the target, the proposed method may lead to registration issues when rotations are not small. Conversely, given the FLS acquisition rate (usually more than 1 Hz) and the relatively slow dynamics of the underwater vehicle, this phenomenon can usually be neglected.

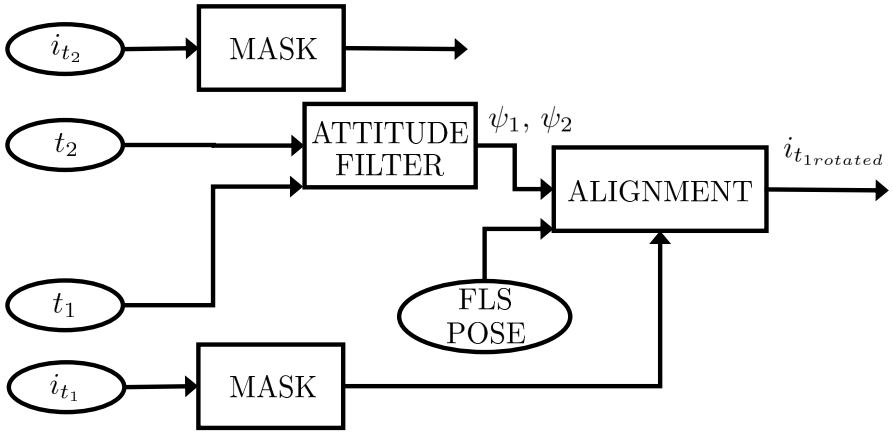

Figure 4.4: Images alignment.

4.1.2 Phase correlation for linear translation

The phase correlation technique is performed, and the translation $\boldsymbol{s}$ (see Eq.3.47) between the two subsequent FLS images i_{t_1} and i_{t_2} is computed from the peak on the normalized cross-power spectrum (Eq.3.45, Eq.3.46, and Eq.3.47).
The typical noise present in FLS images leads to a cross-power spectrum $c(x, y)$ with several peaks in the spatial domain, and to overcome this issue, filtering operations are necessary before applying Eq.3.46. Different approaches can be pursued to accomplish such a task:

- apply a filtering action directly on the noisy FLS images. Unfortunately, a rough knowledge of the image spectra might put in jeopardy the success of phase correlation, eliding frequency components that carry information. Indeed, a wrong filter choice could promote low frequencies due for example to reflectivity transition from a sandy area to vegetation and bury high ones that depend upon, for example, object edges;

- apply a filter in the spatial domain after computing the inverse FT; in this case, for example, a simple mean filter, which promotes high peaks surrounded by peaks of smaller amplitude, might be a robust solution. On the other hand, to the best author's experience, working on the

spatial domain performs, generally speaking, worse. Furthermore, the bigger the size of the kernel is, the higher the computational burden;

- apply a filter in the frequency domain after computing the normalized cross-power spectrum Eq.3.45 and before applying the inverse FT. Hence, this way, the original image content is preserved, and filtering operations take place after, leading to a much manageable surface of $c(x, y)$. It is worth highlighting that, in this case, the computational burden remains the same by changing the filter parameters (such as the cut-off frequency).

The latter option has been followed in the development of this work. With the aim of maintaining the computational burden as low as possible, a non-adaptive Low Pass (LP) Butterworth filter (a commonly used filter in image processing), defined in Eq.4.8 and visible in Fig.4.5, has been tested, and further references can be found in [Weeks, 1996]. The final tuning parameters have been obtained after testing different combinations. A fourth-order Butterworth filter with a cut-off frequency of 60 pixels (the image resolution is 894x477 pixels) has been found to be the best solution in terms of overall behavior. Because the choice of the cut-off frequency (as well as the filter order) is not adaptive, its performance might have issues when different kinds of sea bottom (*e.g.* sandy, rocky or when feature-rich environments are present) are encountered. On the other hand, the achieved results seem not to be significantly affected by this fact, at the same time keeping the complexity low.

$$H(m,n) = \frac{1}{1 + (\frac{D(m,n)}{D_0})^{2l}}, \tag{4.8}$$

where $H(m, n)$ is the transfer function, D_0 is the cutoff frequency, l is the filter order, and $D(m, n) = \left[(m - M/2)^2 + (n - N/2)^2\right]^{1/2}$, where M is the number of columns and N is the number of rows. Regardless of the specific filtering approach, the amplitude of the normalized cross-power spectrum gives a measure of the goodness of the obtained translation and a binary

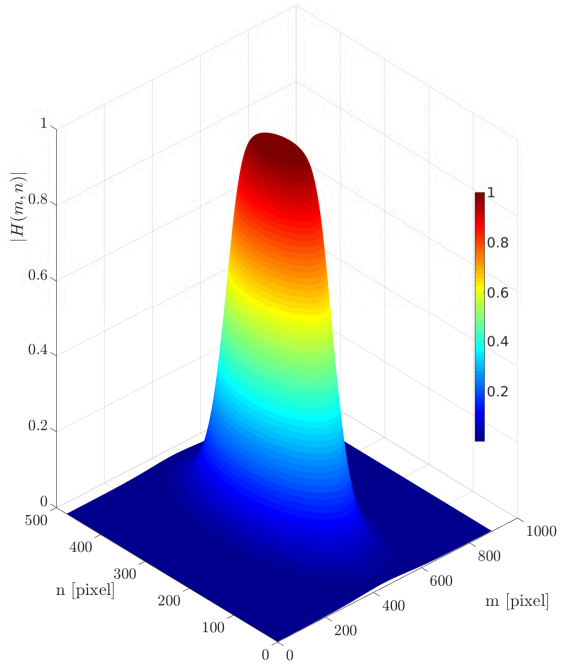

Figure 4.5: The module of a LP Butterworth filter. The filter order is 4 and D_0 is 110.

acceptance law, based on the value of c_r in Eq.4.9 is performed.

$$\begin{aligned} c_p &= \max\{c(x,y)\} \\ c_r &= 1 - \frac{\overline{c(x,y)}}{c_p}, \end{aligned} \tag{4.9}$$

where $\overline{c(x,y)}$ is the average value of the normalized cross-power spectrum and c_p is its actual peak. In Fig.4.6 and Fig.4.7, the normalized cross-power spectrum $c(x,y)$ is shown both without and with the above-mentioned LP filtering action to $C(m,n)$, respectively. The presence of the LP filter leads to a surface where the peak is clearly visible and thus simpler to detect (see Fig.4.7).

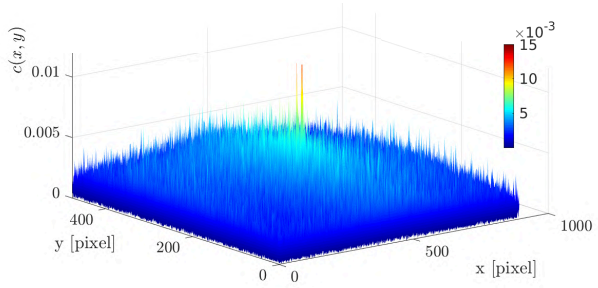

(a)

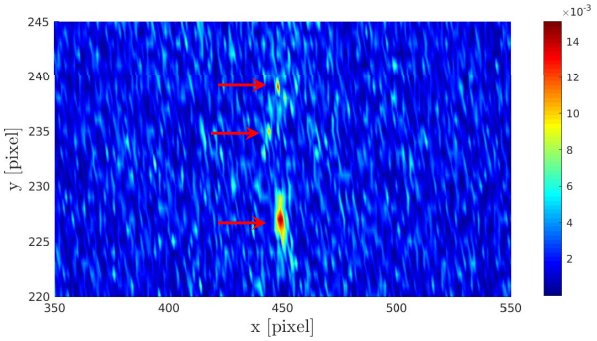

(b)

Figure 4.6: The spatial domain representation of the normalized cross-power spectrum $c(x, y)$. 3D (a) and 2D (b) version. (b) is zoomed in on the peaks. Note the presence of several peaks close to the right one that could negatively affect the peak detection procedure.

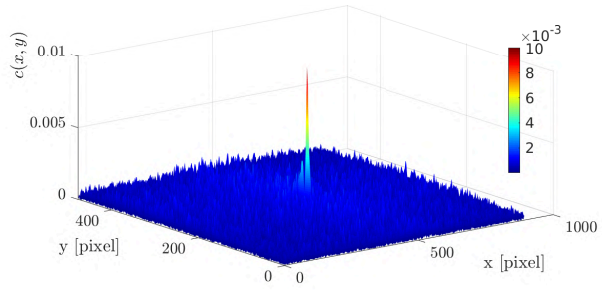

(a)

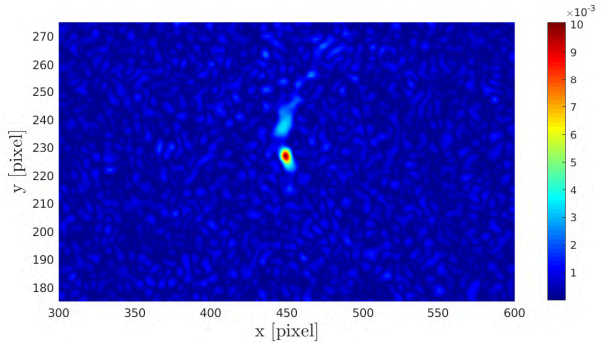

(b)

Figure 4.7: The spatial domain representation of the normalized cross-power spectrum after the application of an LP Butterworth filter. 3D (a) and 2D (b) version. (b) is zoomed in on the main peak. Note the presence of a unique and recognizable peak.

4.1.3 Body speed estimation

Given the exact (absolute) arrival time of the two FLS images t_1 and t_2 and the retrieved translation $\boldsymbol{s}$ (see Eq.3.46), the latter is mapped from *pixel* to *meters* (or another similar physical quantity) by taking advantage of the following (linear) transformation:

$$\mathbf{S} = R_{\rightarrow MAX} \frac{\mathbf{s}}{h}, \tag{4.10}$$

where $\mathbf{s} = \begin{bmatrix} s_x \\ s_y \end{bmatrix} \in \mathbb{R}^2$ is a distance in *pixel*, $\mathbf{S} = \begin{bmatrix} S_x \\ S_y \end{bmatrix} \in \mathbb{R}^2$ is the same physical quantity expressed in *meters*, $R_{\rightarrow MAX}$ is the maximum range delivered by the FLS, and h is the maximum FLS range expressed as number of rows (pixel) in the FLS image (see Fig.4.8). The conversion factor $\frac{R_{\rightarrow MAX}}{h}$ in Eq.4.10 is true for displacement along the rows of the image, but it is an approximation for those along the columns. Exploiting Assumption 1 (most of the AUV's motion takes place along the surge axis) and given the placement of the FLS (usually mounted at the bow of the vehicle pointing forward), the majority of the displacements takes place along the row of the images, and the approximation can be sufficient. At this point, the body

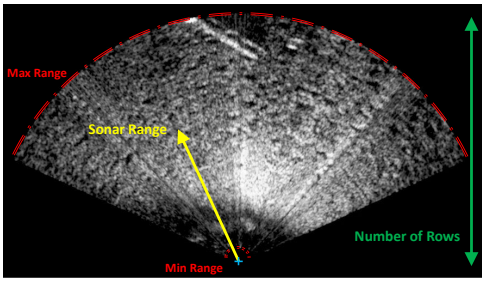

Figure 4.8: Conversion from pixel to meters (or another similar physical quantity).

speed estimation can be easily computed.

$$^b\boldsymbol{\nu}_1 = \frac{^b\boldsymbol{S}}{t_2 - t_1}. \tag{4.11}$$

It should be stressed that in light of the proposed method, only the speed in the plane $x^b y^b$ can be obtained. Nevertheless, the speed along the z^b-axis can be estimated using the DS. Before using the retrieved speed as input for the

navigation filter, its value is checked with the maximum performance that the AUV is able to carry out. In particular, if the longitudinal and lateral speeds do not fall inside specific ranges, the retrieved velocity is discarded; the oldest image, namely i_{t_1}, is deleted, and a new one is acquired. A complete overview of the proposed method is depicted in Fig.4.9.

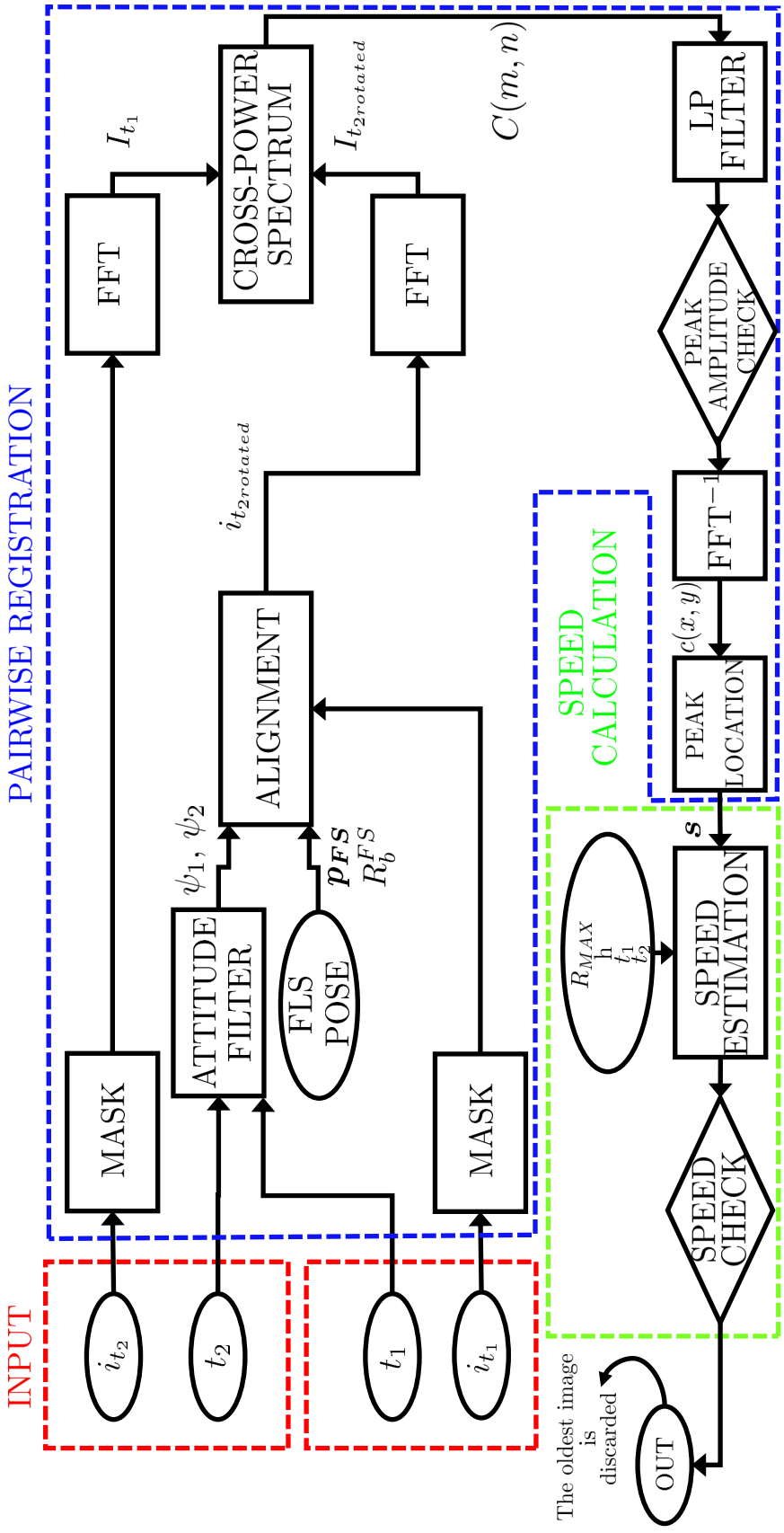

Figure 4.9: The workflow of the speed estimation method exploiting FLS images.

A first offline evaluation of the proposed solution is depicted in Fig.4.10. Here, a comparison between data gathered from a Nortek DVL1000 DVL and linear speed estimation obtained with a Teledyne BlueView M900 2D FLS is presented (for the interested reader more comparisons can be found in [Franchi et al., 2018], and [Franchi et al., 2019b]). In particular, an underwater mission, performed at the ERL SAUC-E 2018 competition held in La Spezia (Italy) in July 2018 with FeelHippo AUV at a depth of 2 m with a reference longitudinal cruise speed of 0.5 m/s, is used. The total mission lasted around 960 s covering approximately 220 m with a maximum range ($R_{\rightarrow_{MAX}}$) of 10 m for the FLS. For the sake of clarity, only a portion of the complete underwater mission is shown. It is worth noting that the underwater scenario presented both areas where the seafloor contained a high informative content (two underwater structures approximately 2.2×3.2×1.2 m were located on the seafloor, see Fig.4.11) and regions where seafloor was uninformative (in other words unaltered and flat). Due to this, looking at Fig.4.10, it is clear that a gap between subsequent FLS-based speed estimations is present. A navigation filter must work continuously, so these "blind spots" are not allowed. Since FLS-based speed estimations are affected by the underwater scenario, which is an unpredictable condition, relying on different sources becomes necessary. If cooperation between the FLS and the DVL occurs and standard sea bottom scenarios are present, the solution can work safely. Otherwise, if the DVL contribution lacks, a model-based navigation approach is proposed. In other words, some underwater sea bottoms do not present any informative content, and therefore it is not possible to understand the vehicle motion from the FLS images. In such situations, linear speed estimation must be obtained from other sources, for example, the DVL if present and works correctly and/or a dynamic model of the vehicle. How the dynamic model of the vehicle has been enhanced and improved in the framework of this work is discussed in Section 4.2.

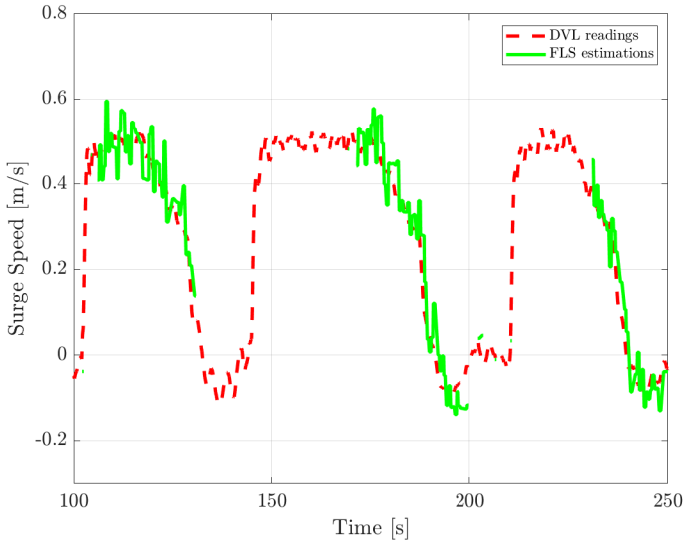

Figure 4.10: Body-speed comparison along surge axis: readings from Nortek DVL1000 are depicted in red, whereas the FLS-based estimations are in green.

Figure 4.11: One of the two underwater structures at the ERL SAUC-E 2018 challange.

4.2 AUV dynamic model

4.2.1 Propulsion model

With regard to the propulsion model presented in Eq.4.3, new tests with the aim of obtaining a complete characterization of the propulsion system BlueRobotics T200 [Blue Robotics Inc., 2019] have been conducted [Franchi et al., 2019a], and the experimental work presented by the authors in [Allotta et al., 2017] has been improved. In particular, new tests have been performed

with different voltage supplies to gain more insight into the propulsion system. To this end, a new test rig has been designed and developed, see Fig.4.12. Furthermore, taking into account dead-zones between the command drive and the motor thrust, the propulsion model presented in Eq.4.3 and proposed in [Allotta et al., 2017] has been enhanced, and the final result is shown in Eq.4.13. More information concerning the test rig design and the new tests can be found in [Pagliai, 2019].

A quantitative evaluation of the analytical expression in Eq.4.3 requires the knowledge of the propeller pitch p_p, which is a construction parameter (usually provided by the manufacturer), and of the coefficient k. This relates motor thrust and propeller speed at bollard conditions (*i.e.* when the advance speed $V_{a,i} = 0$), see Eq.4.6. Bollard thrust tests have been performed in a testing pool, and the thrust-propeller rotational speed-voltage supply triad has been measured in several working conditions.

Voltage supply has been increased at discrete steps: 12.0, 14.0, 16.0, 22.0, and 25.2 V, and for each value, the thrust has been measured varying the propeller rotational speed. Because of the asymmetry of the BlueRobotics T200 propeller, both forward (first quadrant motor operation) and backward (third quadrant motor operation) tests have been conducted. The complete results are presented in Fig.4.13 and Fig.4.14, where the bollard coefficients are 0.0128 Ns^2 and -0.008753 Ns^2 for the forward motion and the backward one, respectively. In the first case, the coefficient of determination R^2 defined in Eq.4.12 is 0.9922, whereas in the second it is 0.9639.

$$R^2 = 1 - \frac{SS_{\text{res}}}{SS_{\text{tot}}}, \tag{4.12}$$

where SS_{res} is the sum of squares of residuals and SS_{tot} is the total sum of squares. At bollard conditions, given a specific command drive, the more the voltage level, the more the absorbed current and, therefore, the greater the rotational speed and the exerted thrust. However, the relationship between the rotational speed and the respective thrust remains always the same (see Fig.4.13 and Fig.4.14). This is not surprising, as, at bollard conditions, the relationship is only affected by the propeller and nozzle geometry. The results presented in Fig.4.14 (backward motion) are slightly worse because of the compression localized on the load cell, leading to small skids. This is due to the connection clearance between the load cell and the

test rig bar, which adversely affects the measurements, see Fig.4.12.
The experimental test rig set-up was composed of a TAS510 load cell by HT Sensor Technology CO., LTD [HT Sensor Technology CO.,LTD, 2019], and a CF350-FFT spectrum analyzer by ONO SOKKI CO., LTD [ONO SOKKI CO.,LTD, 2019] for precise rotational speed measurements for the propeller. To amplifying the thrust exerted by the motors mechanically, a leverage system composed of standard aluminum profiles was designed. More specifically, the thrust measurement is obtained as the result of the ratio between the thruster arm and the cell arm, and their lengths can be easily regulated by a screw. A schematic representation is visible in Fig.4.12b).

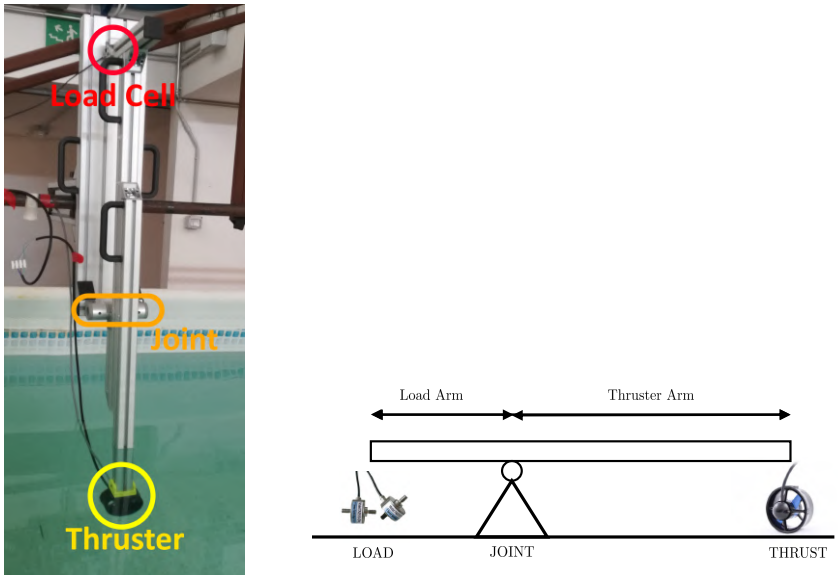

(a) Physical system. (b) Schematic representation.

Figure 4.12: The experimental test rig set-up. a) the physical system, whereas b) a schematic representation.

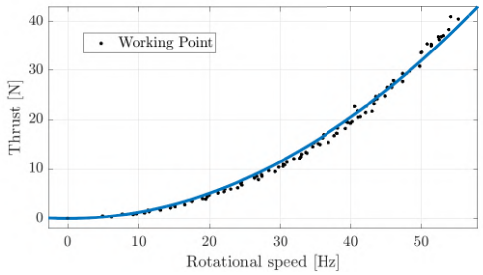

(a) Thrust-rotational speed

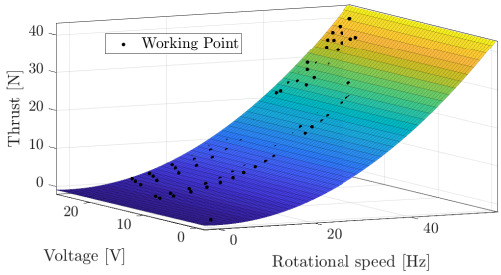

(b) Thrust-rotational speed-voltage

Figure 4.13: Bollard thrust tests for the forward motion (first quadrant motor operation).

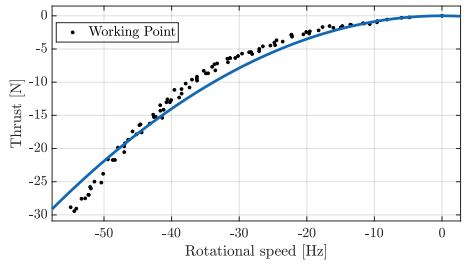

(a) Thrust-Rotational speed

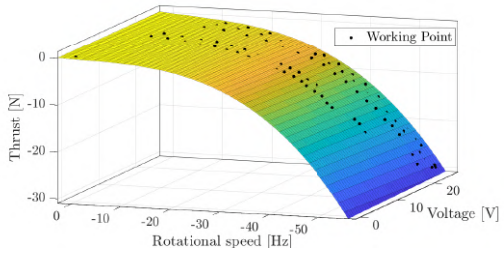

(b) Thrust-Rotational speed-voltage

Figure 4.14: Bollard thrust tests for the backward motion (third quadrant motor operation).

Currently, during underwater operations, FeelHippo AUV, MARTA AUV, and Zeno AUV are not equipped with a sensor able to measure the actual propeller rotational speed, such as Hall effect-based speed sensors (see Section 2); but only its reference value is available. Conversely, exploiting Assumption 4 and noting that the propulsion system normally presents fast dynamics with respect to the relatively slow dynamics of the vehicle counterpart, the committed error can be considered a further approximation with respect to the one already introduced by the four-quadrant motor characteristic in Eq.4.3 and Eq.4.13 such that, even if it represents a satisfying description, it inevitably introduces unknown model errors. Briefly, reference values for the rotational speed below a certain threshold are not followed, where the drive command signal is not sufficient to produce a rotational movement for the thruster.
In Fig.4.15, it can be noted that the minimum rotational speed that can be obtained depends on the voltage supply. Indeed, given a certain command drive logic, the lower the supply voltage, the less the output voltage. Furthermore, the resulting behavior is not affected by the direction of motion.

To prove this, the slopes of the lines depicted in Fig.4.15 are almost the same (in absolute value), at -0.5974 and 0.5866. This is not surprising, as it is known that a linear relation between rotational speed and voltage supply holds for a Direct Current (DC) motor.
The point to highlight from the above treatment is that in case of the unavailability of direct speed measurements, the relationship between thrust and command driver needs to be thoroughly investigated.

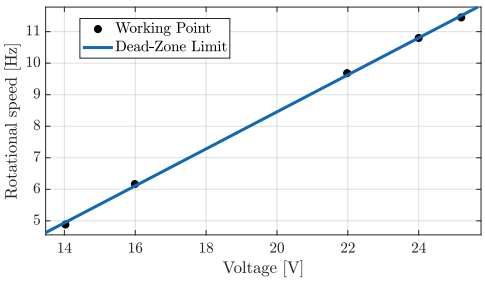

(a) Forward motion

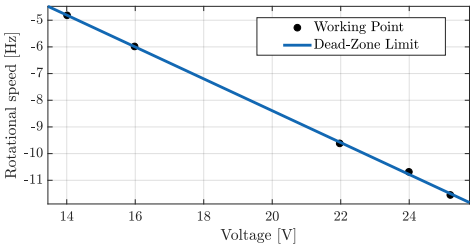

(b) Backward motion

Figure 4.15: Relation between the boundary values for the dead-zone and the supply voltage level.

In conclusion, Eq.4.3 becomes Eq.4.13.

$$T_i(\boldsymbol{\nu}, \hat{u}_{rpm_i}) = \\ = d(\hat{u}_{rpm_i}, \mathcal{V})[\text{sgn}(\hat{u}_{rpm_i})(k\hat{u}^2_{rpm_i} - \frac{k|\hat{u}_{rpm_i}|g(\text{sgn}(\hat{u}_{rpm_i})V_{a,i})}{p_p})], \tag{4.13}$$

where $\hat{u}_{rpm_i}$ is the reference value for the rotational speed of the $i-th$ motor,

Main propulsion model parameters	
Propeller pitch (p_p) [m/rev]	0.094
Forward bollard coefficient k^+ [Ns^2]	0.0128
Backward bollard coefficient k^- [Ns^2]	-0.008753
Forward dead-zone boundary limit u^+_{rpm} [Hz]	$4.8833 + 0.5866(\mathcal{V} - 14)$
Backward dead-zone boundary limit u^-_{rpm} [Hz]	$-4.8167 - 0.5974(\mathcal{V} - 14)$

Table 4.1: Main propulsion model parameters.

$\mathcal{V}$ is the voltage supply, and $d(x)$ is defined in Eq.4.14.

$$d(x, \mathcal{V}) = \begin{cases} 0 & \text{for } x \geq u^-_{rpm}(\mathcal{V}) \\ 0 & \text{for } x \leq u^+_{rpm}(\mathcal{V}) \\ 1 & \text{otherwise} \end{cases}, \tag{4.14}$$

where u^-_{rpm} (backward motion) and u^+_{rpm} (forward motion) are the boundary values for the dead-zone that depend upon the voltage supply level. If the reference value for the rotational speed falls within this interval, the exerted thrust is zero.

4.2.2 Online surge dynamic estimator

Regardless of the specific mission the underwater vehicle (ROV or AUV) is required to perform, the estimation of its dynamic parameters is of utmost importance: from Kalman-based state estimators to linear or nonlinear controllers, such as [Cristi et al., 1990], [Healey and Lienard, 1993], [Li and Yan, 2016], and [Rypkema et al., 2018].

Historically, the first solutions resorted to towing tank trials applied both to the involved underwater vehicle or to a scaled version [Caccia et al., 2000]. With the increasing computing power of modern computers, Computational Fluid Dynamics (CFD) methods have become more widespread throughout the years. Although they can provide a complete description of the vehicle in terms of model identification, the total cost and complexity are often strong disadvantages. In addition to this, with the increasing pres-

ence in the market of modular or reconfigurable vehicles ([Allotta et al., 2014], [Pettersen et al., 2018], [Manley et al., 2018], and [Pagliai, 2019]), a method able to cope the change in vehicle configuration or vehicle geometry (such as propeller and payload configuration) becomes necessary. To overcome these issues, identification methods that exploit onboard sensor readings have emerged as a strong and reliable alternative. The underlying idea is based on measuring the vehicle response under known excitactions. As suggested by [Eng et al., 2015], such solutions, which allow AUV dynamics to be identified more rapidly, are called onboard system identification or in-field identification.
For what concerns the world of underwater vehicle (both ROVs and AUVs), EKF estimators as [Marco et al., 2005] and [Luque et al., 2009], Least Squares (LS) or Recursive Least Squares (RLS) methods as in [Goheen and Jefferys, 1990], [Ziani-Cherif et al., 1997], [Caccia et al., 2000], [Martin and Whitcomb, 2013], [Eng et al., 2015], and [Allotta et al., 2018], or adaptive techniques as [Smallwood and Whitcomb, 2003] have been proposed.
Throughout the years, more complex solutions have been presented. Just to name a few, in [Xu et al., 2013] an hybrid solution based on LS and Support Vector Machines (SVM) is discussed. In [Sabet et al., 2017], the main hydrodynamic parameters of an AUV are estimated; in particular, Cubature Kalman Filter (CKF) and Transformed Unscented Kalman Filter (TUKF) methods are tested. In [Chou et al., 2017], the AUV poses are obtained using laser images captured by an onboard camera; a genetic algorithm is used to retrieve the hydrodynamic coefficients.
The approach followed in this thesis has always headed towards a solution able to maintain the computational burden as low as possible, keeping in mind a possible future online implementation on the vehicles of the UNIFI DIEF MDM Lab fleet.

As a consequence, in the following, a light-weight, online stand-alone technique able to estimate online the longitudinal drag (since most of the AUV dynamics take place in this direction) is presented. Differently from LS methods that intrinsically adapt some parameters over a complete data set, or RLS techniques that present in any event a computational complexity that is $O\left(N^2\right)$ (N is the size of the data window), the proposed solution instead, adapting the estimation to the current sensors readings, posses al-

ways the same computational complexity.
Given a vectored variable

$$\boldsymbol{t} = \boldsymbol{\zeta}(\boldsymbol{\xi}, \boldsymbol{\lambda}) + \boldsymbol{\epsilon}, \tag{4.15}$$

where $\boldsymbol{t} \in \mathbb{R}^t$ is called *target function*, $\boldsymbol{\zeta}(\boldsymbol{\xi}, \boldsymbol{\lambda})$ is deterministic function $\in \mathbb{R}^t$, $\boldsymbol{\xi} \in \mathbb{R}^x$ is a generic input variable, $\boldsymbol{\lambda} \in \mathbb{R}^{l \cdot t}$ is a set of parameters, and $\boldsymbol{\epsilon} \in \mathbb{R}^t$ is a zero mean Gaussian vectored random variable with $\sigma^2_{\mathcal{E}} \in \mathbb{R}^{t \times t}$ covariance matrix. Let us assume that $\boldsymbol{\zeta}(\boldsymbol{\xi}, \boldsymbol{\lambda})$ is a linear combinations of fixed nonlinear functions of the input variables $\boldsymbol{\xi}$, of the form

$$\boldsymbol{\zeta}(\boldsymbol{\xi}, \boldsymbol{\lambda}) = L(\boldsymbol{\lambda})^\top \boldsymbol{\phi}(\boldsymbol{\xi}), \tag{4.16}$$

where $\boldsymbol{\phi}(\boldsymbol{\xi})$ is a nonlinear map $\boldsymbol{\phi} : \mathbb{R}^x \to \mathbb{R}^l$ (ϕ_j are the elements of $\boldsymbol{\phi}$, called *basis function* with $\phi_0(\boldsymbol{\xi}) = 1$), and $L(\boldsymbol{\lambda})$ is a $\in \mathbb{R}^{l \times t}$ matrix that collects the parameters $\boldsymbol{\lambda}$.

Pure quadratic damping model

In Chapter 4, in light of Assumptions 1 - 4, it is shown how the complete dynamic model presented in Eq.3.10 can be simplified into Eq.4.1 with the drag description in Eq.4.2. Eq.4.17 can be rewritten in a more compact form as:

$$m\dot{\nu}_{1x} = m\dot{u} = \tau_{1x}(\boldsymbol{\nu}, \boldsymbol{u}) - \delta_{Qx}\nu^2_{1x}\,\mathrm{sgn}\,(\nu_{1x})\,, \tag{4.17}$$

where $\delta_{Qx} = \frac{A_f C_u \rho}{2}$ puts together all the parameters involved in the longitudinal drag and where the parameter to be estimated is δ_{Qx}.
The general treatment presented in Eq.4.15 and Eq.4.16 can be therefore strongly simplified to the scalar case. In particular, the problem can be defined as follows:

$$t = \zeta(\xi, \boldsymbol{\lambda}) + \epsilon, \tag{4.18}$$

where $t = \tau_{1x}(\boldsymbol{\nu}, \boldsymbol{u}) - m\dot{\nu}_{1x}$, $\xi = \nu_{1x}$, $\zeta = \lambda_0\phi_0 + \lambda_1\phi_1$ with $\boldsymbol{\phi}(\xi) = \begin{bmatrix} \phi_0 \\ \phi_1 \end{bmatrix} = \begin{bmatrix} 1 \\ \nu^2_{1x}\,\mathrm{sgn}\,(\nu_{1x}) \end{bmatrix}$ and $\boldsymbol{L}(\boldsymbol{\lambda}) = \begin{bmatrix} \lambda_0 \\ \lambda_1 \end{bmatrix} = \begin{bmatrix} 0 \\ \delta_{Qx} \end{bmatrix}$ and $\epsilon \in \mathbb{R}$ is a zero mean

Gaussian random variable with variance σ_ϵ^2.
Let us define an error metrics as:

$$\begin{aligned} E(\boldsymbol{\lambda}) &= \frac{1}{2}\left\{t - \boldsymbol{L}(\boldsymbol{\lambda})^\top \boldsymbol{\phi}\left(\boldsymbol{\xi}\right)\right\}^2 = \\ &= \frac{1}{2}\left\{\tau_{1x}(\boldsymbol{\nu}, \boldsymbol{u}) - m\dot{\nu}_{1x} - \delta_{Qx}\nu_{1x}^2 \operatorname{sgn}\left(\nu_{1x}\right)\right\}^2, \end{aligned} \tag{4.19}$$

where $E(\boldsymbol{\lambda}) \in \mathbb{R}^+$ is the L2-norm whose gradient is:

$$\nabla E(\boldsymbol{\lambda}) = \left\{t - \boldsymbol{L}(\boldsymbol{\lambda})^\top \boldsymbol{\phi}\left(\boldsymbol{\xi}\right)\right\} I(2)\boldsymbol{\phi}(\boldsymbol{\xi}), \tag{4.20}$$

where $I(2)$ is the 2D identity matrix. The second element of $\nabla E(\boldsymbol{\lambda})$ is therefore:

$$[\tau_{1x}(\boldsymbol{\nu}, \boldsymbol{u}) - m\dot{\nu}_{1x} - \delta_{Qx}\nu_{1x}^2 \operatorname{sgn}\left(\nu_{1x}\right)]\nu_{1x}^2 \operatorname{sgn}(\nu_{1x}). \tag{4.21}$$

By applying the technique of stochastic gradient descent [Bishop, 2006] to Eq.4.18 with the error defined as in Eq.4.19 a sequential estimation technique can be obtained, see Eq.4.22

$$\delta_{Qx}^{k+1} = \delta_{Qx}^k - \eta^k \nabla E(\boldsymbol{\lambda})^k, \tag{4.22}$$

where k denotes the iteration number, $\eta \in \mathbb{R}^+$ is a rate parameter and $\nabla E(\boldsymbol{\lambda})^k$ is the gradient of $E(\boldsymbol{\lambda})$ at the iteration k. The value of η needs to be chosen with care in order to have algorithm convergence, see [Bishop, 2006]. In the considered case, Eq.4.22 becomes Eq.4.23.

$$\delta_{Qx}^{k+1} = \delta_{Qx}^k - \eta^k \{[\tau_{1x}(\boldsymbol{\nu}, \boldsymbol{u}) - m\dot{\nu}_{1x} - \delta_{Qx}\nu_{1x}^2 \operatorname{sgn}(\nu_{1x})]\nu_{1x}^2 \operatorname{sgn}(\nu_{1x})\}^k. \tag{4.23}$$

ν_{1x} is obtained by means of devices able to measure the linear speed of the vehicle, such as the DVL and/or the FLS as explained in section 4.1, whereas $\dot{\nu}_{1x}$ is obtained through an IMU. Usually, acceleration measurements are too noisy to be used as the raw output of the instruments so, even if a filter is applied on accelerometer measurements (see [Fanelli, 2019]), it has been decided to give less importance to conditions where inertial contributions are not negligible. To do so, underwater missions at constant speed have been

performed, and situations, where the vehicle speed is too low with respect to the reference value, were not considered. Moreover, since the adopted model does not take into account for example added masses (see Eq.4.17), data at steady-state conditions better the description in Eq.4.17.
The proposed solution has been preliminarily validated in post-processing by means of data gathered during real underwater missions. In particular, simulations have been performed with data gathered during sea trials in La Spezia (Italy) at the NATO STO Centre for Maritime Research and Experimentation (CMRE) with FeelHippo AUV in 2018. The mission was executed at the desired depth of 2 m with a reference longitudinal cruise speed of 0.5 m/s for longer transects, and 0.3 m/s for shorter ones and it lasted 700 s covering approximately 220 m. With the aim of assessing the steady-state behavior of the proposed solution with respect to the initialization, δ_{Qx}^0 has been changed in a range from zero to the double of the final estimation value (with η fixed), and the final results are given in Fig.4.16 and Fig.4.17. In the former, the estimation is compared with the iterations of the tested algorithm. In contrast, in the latter, it is compared with the absolute time of the data gathered during the underwater mission. In Fig.4.17 intervals where the estimation remains fixed to a certain value are visible. This is because the proposed algorithm is made to work only when the vehicle moves at approximately constant speed (for example, turns are not considered). In addition to this, it can be noted that the proposed solution always converges to a value close to the one predicted by the LS estimator. To test the steady-state behavior of the proposed solution with respect to the rate parameter, η has been changed (with δ_{Qx}^0 fixed) and the final results are shown in Fig.4.18 and Fig.4.19. In the former, the estimation is compared with the iterations of the tested algorithm. In contrast, in the latter, it is compared with the absolute time of the data gathered during the underwater mission. It can be noted that, although the bigger the rate parameter is, the faster the convergence, an undesired oscillating behavior takes place.

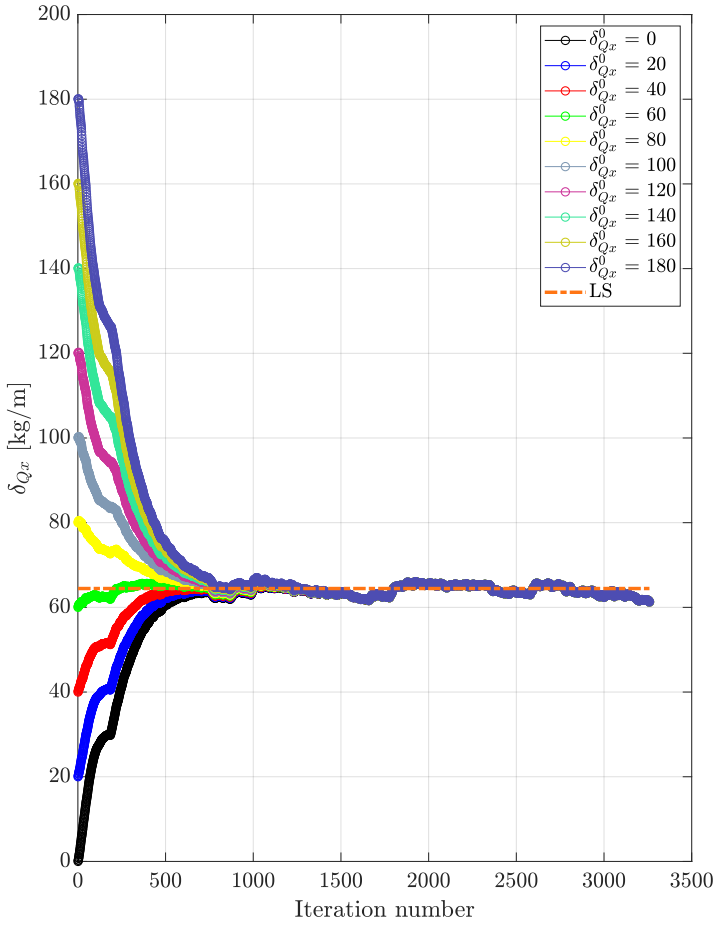

Figure 4.16: δ_{Qx} estimation compared with the iterations of the tested algorithm. By varying δ^0_{Qx}, the proposed solution converges to the same value, which is in accordance with the LS estimator. Data gathered at the NATO STO CMRE with FeelHippo AUV on the 18^{th} of July 2018. $\eta = 0.1$.

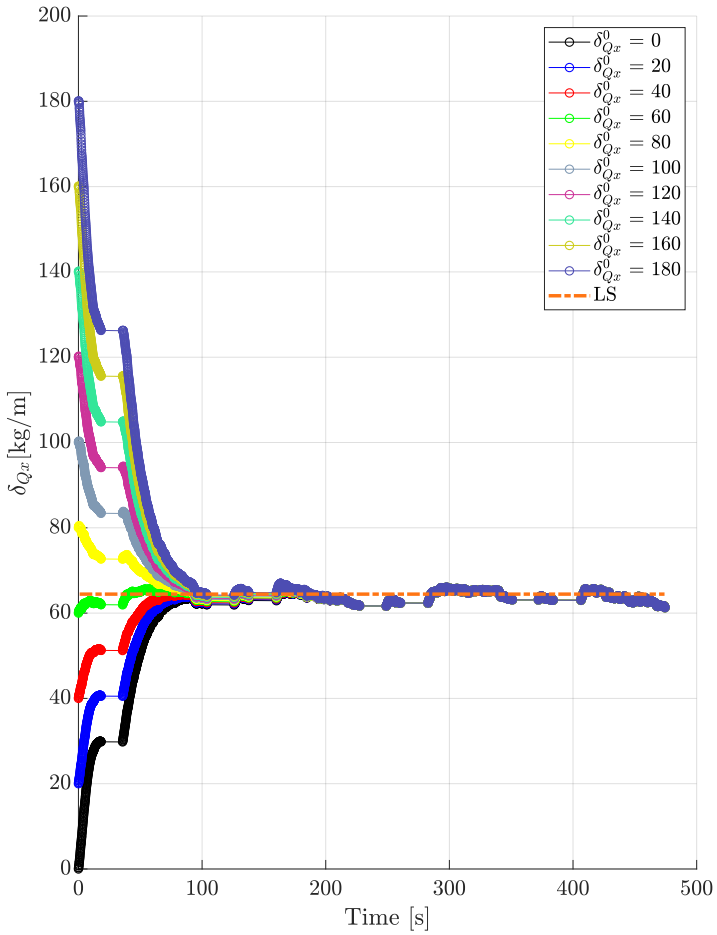

Figure 4.17: δ_{Qx} estimation compared with the absolute time of the data gathered. By varying δ^0_{Qx}, the proposed solution converges to the same value, which is in accordance with the LS estimator. The algorithm stops predicting when the vehicle does not move straight at approximately constant speed. Data gathered at the NATO STO CMRE with FeelHippo AUV on the 18^{th} of July 2018. $\eta = 0.1$.

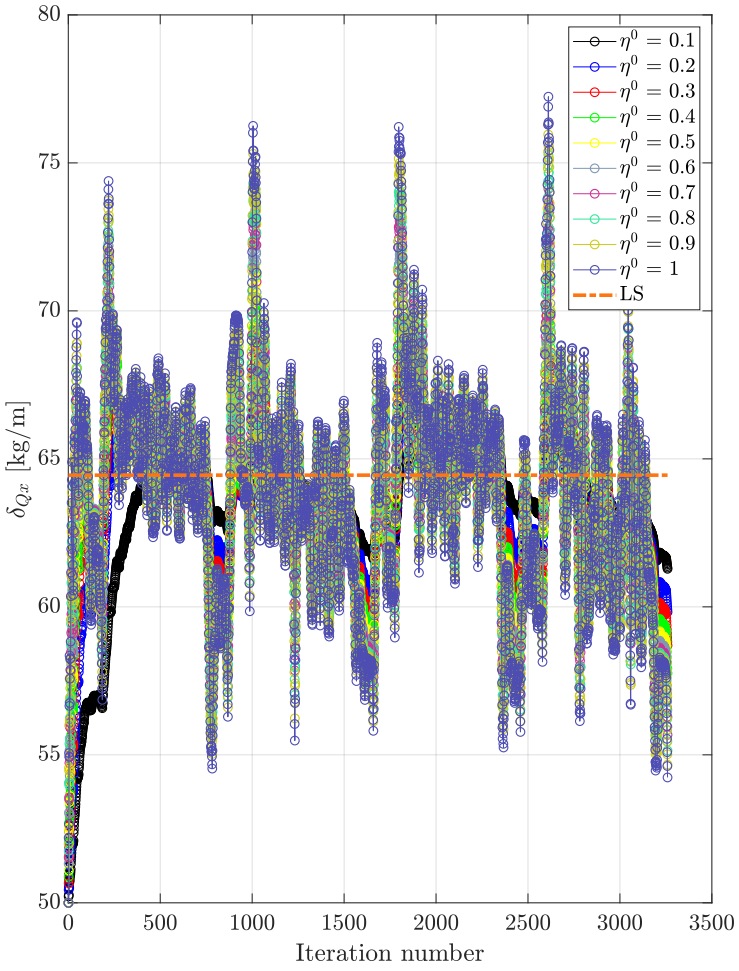

Figure 4.18: δ_{Qx} estimation compared with the iterations of the tested algorithm. For small values of η the proposed solution converges slower, but oscillating behaviors are prevented. Data gathered at the NATO STO CMRE with FeelHippo AUV on the 18^{th} of July 2018. $\delta^0_{Qx} = 50$.

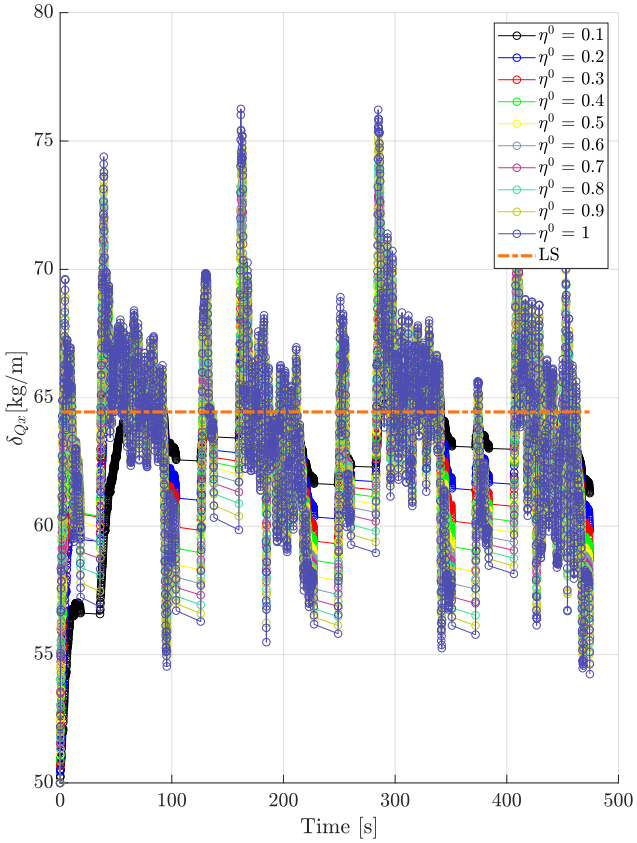

Figure 4.19: δ_{Qx} estimation compared with the iterations of the tested algorithm. For small values of η the proposed solution converges slower, but oscillating behaviors are prevented. The algorithm stops predicting when the vehicle does not move straight at approximately constant speed. Data gathered at the NATO STO CMRE with FeelHippo AUV on the 18^{th} of July 2018. $\delta^0_{Qx} = 50$.

Linear-quadratic damping model

According to [Fossen et al., 1994], a simple quadratic damping in the model may produce an oscillatory behavior at low speed; thus, both linear and quadratic damping terms should be included. To this end, a mixed linear-quadratic damping model for the longitudinal drag has been considered. In this case, the longitudinal motion model becomes:

$$m\dot{\nu}_{1x} = m\dot{u} = \tau_{1x}(\boldsymbol{\nu}, \boldsymbol{u}) - \delta_{Qx}\nu_{1x}^2 \operatorname{sgn}(\nu_{1x}) - \delta_{Lx}\nu_{1x}, \tag{4.24}$$

where δ_{Lx} is the coefficient that takes into account the linear damping and the other symbols have the same meaning of Eq.4.17. Moreover, the terms in Eq.4.18 now become $t = \tau_{1x}(\boldsymbol{\nu}, \boldsymbol{u}) - m\dot{\nu_{1x}}$, $\xi = \nu_{1x}$, $\zeta = \lambda_0\phi_0 + \lambda_1\phi_1 + \lambda_2\phi_2$ with $\boldsymbol{\phi}(\xi) = \begin{bmatrix} \phi_0 \\ \phi_1 \\ \phi_2 \end{bmatrix} = \begin{bmatrix} 1 \\ \nu_{1x}^2 \operatorname{sgn}(\nu_{1x}) \\ \nu_{1x} \end{bmatrix}$ and $\boldsymbol{L}(\boldsymbol{\lambda}) = \begin{bmatrix} \lambda_0 \\ \lambda_1 \\ \lambda_2 \end{bmatrix} = \begin{bmatrix} 0 \\ \delta_{Qx} \\ \delta_{Lx} \end{bmatrix}$. By applying the procedure explained in the previous paragraph, it is easy to find that the gradient in Eq.4.23 becomes:

$$\nabla E(\boldsymbol{\lambda}) = \left\{ t - \boldsymbol{L}(\boldsymbol{\lambda})^\top \boldsymbol{\phi}(\boldsymbol{\xi}) \right\} I(3)\boldsymbol{\phi}(\boldsymbol{\xi}), \tag{4.25}$$

where $I(3)$ is the 3D identity matrix. The second and third element of $\nabla E(\boldsymbol{\lambda})$ are:

$$\left[\tau_{1x}(\boldsymbol{\nu}, \boldsymbol{u}) - m\dot{\nu}_{1x} - \delta_{Qx}\nu_{1x}^2 \operatorname{sgn}(\nu_{1x}) - \delta_{Lx}\nu_{1x}\right] \nu_{1x}^2 \operatorname{sgn}(\nu_{1x}), \tag{4.26}$$

and

$$\left[\tau_{1x}(\boldsymbol{\nu}, \boldsymbol{u}) - m\dot{\nu}_{1x} - \delta_{Qx}\nu_{1x}^2 \operatorname{sgn}(\nu_{1x}) - \delta_{Lx}\nu_{1x}\right] \nu_{1x}^2 \nu_{1x}, \tag{4.27}$$

respectively. Therefore, the updated law is:

$$\delta_{Qx}^{k+1} = \delta_{Qx}^k - \eta^k \{[\tau_{1x}(\boldsymbol{\nu}, \boldsymbol{u}) - m\dot{\nu}_{1x} - \delta_{Qx}\nu_{1x}^2 \operatorname{sgn}(\nu_{1x}) - \delta_{Lx}\nu_{1x}]\nu_{1x}^2 \operatorname{sgn}(\nu_{1x})\}^k \tag{4.28}$$

$$\delta_{Lx}^{k+1} = \delta_{Lx}^k - \eta^k \{[\tau_{1x}(\boldsymbol{\nu}, \boldsymbol{u}) - m\dot{\nu}_{1x} - \delta_{Qx}\nu_{1x}^2 \operatorname{sgn}(\nu_{1x}) - \delta_{Lx}\nu_{1x}]\nu_{1x}\}^k \tag{4.29}$$

As in the previous case, the proposed solution has been preliminary validated with the same data, but here the situation is more complicated. Indeed, the steepest descendent method tries to locally minimize a convex functional ($E(\boldsymbol{\lambda}) = \frac{1}{2}\left\{t - \boldsymbol{L}(\boldsymbol{\lambda})^\top \boldsymbol{\phi}(\boldsymbol{\xi})\right\}^2$ in this case) by means of the gradient direction. For the mixed linear-quadratic damping model, Eq.4.19 becomes:

$$E(\boldsymbol{\lambda}) = \frac{1}{2}\left\{\tau_{1x}(\boldsymbol{\nu}, \boldsymbol{u}) - m\dot{\nu}_{1x} - \delta_{Qx}\nu_{1x}^2 \operatorname{sgn}(\nu_{1x}) - \delta_{Lx}\nu_{1x}\right\}^2. \tag{4.30}$$

Here, it is easy to understand that $\tau_{1x}(\boldsymbol{\nu}, \boldsymbol{u}) - m\dot{\nu}_{1x} - \delta_{Qx}\nu_{1x}^2 \operatorname{sgn}(\nu_{1x}) - \delta_{Lx}\nu_{1x} = 0$, given τ, $m\dot{\nu}_{1x}$, and ν_{1x}^2 presents infinite solutions for δ_{Qx}, δ_{Lx} (all the points that lie on the line), see Fig.4.20. Therefore, the algorithm

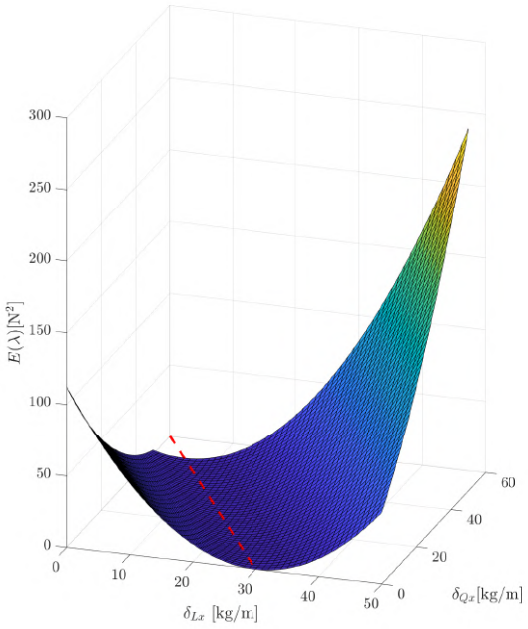

Figure 4.20: The functional $E(\boldsymbol{\lambda})$ defined in Eq.4.30 and the line $\tau_{1x}(\boldsymbol{\nu}, \boldsymbol{u}) - m\dot{\nu}_{1x}^2 - \delta_{Qx}\nu_{1x}^2 \operatorname{sgn}(\nu_{1x}) - \delta_{Lx}\nu_{1x} = 0$ in red.

leads to different estimates that depend upon, for example, the initial guesses δ_{Qx}^0, δ_{Lx}^0. This ambiguity is obviously not welcome. As a consequence, if any constraint is imposed for δ_{Qx}^0, δ_{Lx}^0, this modeling has decided not to be adopted. In the following, the pure quadratic damping model presented in the previous paragraph is employed.

4.3 Adaptive Unscented Kalman Filter

This section covers the proposed solution for what concerns Adaptive Kalman Filters (AKFs) with particular emphasis to AUKFs. After an overview of the problem, the proposed solution is presented.
Adaptive estimation under uncertain parameters comprises the system model $(\boldsymbol{f}(\bullet), \boldsymbol{h}(\bullet))$ or the statistical information through the matrices (R, Q). In the following, it is assumed that the description of the system through $\boldsymbol{f}(\bullet), \boldsymbol{h}(\bullet)$ is acceptable, and the adaptation is performed on the filter statistics R, Q. It is well known that the KF is an optimal estimator in the Minimum Mean Square Error (MMSE) sense under the assumption of linear models and white Gaussian properties for the initial state and all the noises [Bar-Shalom et al., 2004], and it has been widely used in many applications and fields; navigation, target tracking, and control are just a few examples. Generally speaking, the optimality of the estimation algorithm depends upon the quality of the a priori information about the noise statistics (process noise and measurement noise) and, unfortunately, in practical situations are either unknown or approximately known. A poor knowledge of the a priori filter statistics will either worsen the precision of the estimator [Obsharsky et al., 1969] or lead to unwanted estimation errors or filter divergence [Mehra, 1972]. To overcome the above-mentioned issues the most common method is the AKF (or its variants applied to EKFs or UKFs). Adaptive techniques intrinsically place less reliance on a priori information. On the one hand, the problem of unknown or approximately known noise statistics is solved by continuously exploiting the filter learning history. On the other hand, having a dynamic adaptation that evolves in a dynamic environment may lead to better performance [Mohamed and Schwarz, 1999].
As firstly suggested by [Mehra, 1972], AKF methods can be divided into four approaches:

- Bayesian methods;
- correlation;
- maximum likelihood;
- covariance matching.

Example of Bayesian methods are Multiple Model Adaptive Kalman Filter (MMAKF), where a bank of KFs with different models for R, Q run simultaneously in parallel [Li and Bar-Shalom, 1994], state augmentation-based methods [Wan and Nelson, 2001] or variational Bayesian approaches [Sarkka and Nummenmaa, 2009] and [Huang et al., 2017]. Correlation-based solutions try to estimate the noise covariance matrices by using, at different lags, the sample autocorrelation functions of the innovations [Bélanger, 1974], [Odelson et al., 2006], and [Åkesson et al., 2008]. Maximum Likelihood Estimation (MLE) techniques formulate the estimation problem as maximization of the likelihood function associated with the observed data and contributions can be found in [Bavdekar et al., 2011], [Zagrobelny and Rawlings, 2015], and [Mahmoudi et al., 2017]. The main drawback of this method is the computational cost that often forces towards simplified structures for the matrix R, Q. Lastly, covariance matching methods estimate R, Q, comparing online estimates of residual or innovation covariances (computed either over the entire data set or, more often, over a moving window) and their theoretical values. The main advantage is the low computational burden as well as flexibility, and more information will be provided in the following.

The above-mentioned methods are not limited to KFs, and they can be suitably applied to their nonlinear counterparts. For what concerns UKF, AUKF proposals can be found for example in [Zhou et al., 2010], [Sun et al., 2011], [Hajiyev and Soken, 2014], [Zagrobelny and Rawlings, 2015], [Gao et al., 2015], and [Zheng et al., 2018], whereas marine robotics applications are very limited and few contributions can be found in [Zhu et al., 2009] and [Liu et al., 2019], where only simulations are presented and [Liu et al., 2014] and [Mehrjouyan and Alfi, 2019], where data obtained during sea trials are post-processed. In addition to this, generally speaking, adaptive filtering in the marine field has not been completely tackled yet and, to the best author's knowledge, only one remarkable experimental contribution can be found in [Davari and Gholami, 2016]. In conclusion, adaptive filtering for underwater vehicle navigation is still a niche and open problem. Although the mathematical and theoretical foundations have been widely investigated since the '70s, applications to online underwater navigation are minimal.

4.3.1 Problem formulation and proposed solution

The proposed solution can be classified as a covariance matching-based method applied to UKFs. One of the first covariance matching approach can be attributed to [Sage and Husa, 1969] and afterward, relying on more solid assumptions to [Mehra, 1972] for KFs. Over the years different covariance-matching approaches have been proposed tailored for KF, EKF, and UKF estimators. In particular, generally speaking, results obtained under standard KF hypotheses are extended to the other estimators.
From Eq.3.28, assuming additive noise, Eq.4.31 can be obtained.

$$\begin{cases} \boldsymbol{x}_k = \boldsymbol{f}_{k-1}\left(\boldsymbol{x}_{k-1}, \boldsymbol{u}_{k-1}\right) + \boldsymbol{w}_{k-1} \\ \boldsymbol{y}_k = \boldsymbol{h}_k\left(\boldsymbol{x}_k\right) + \boldsymbol{v}_k \end{cases} \tag{4.31}$$

For the sake of clarity, the symbols in Eq.4.31 are here defined again. $\boldsymbol{w} \in \mathbb{R}^{n_a}$ and $\boldsymbol{v} \in \mathbb{R}^p$ are modeled as zero-mean stationary white noise (initial state and process and measurement noises are assumed to have zero cross-correlation), and $\boldsymbol{f}(\bullet)$ and $\boldsymbol{h}(\bullet)$ are two generic nonlinear, time-varying function. $\boldsymbol{u}(t) \in \mathbb{R}^m$ is a vector of controlled inputs, $\boldsymbol{x} \in \mathbb{R}^{n_a}$ is the state vector, $\boldsymbol{y} \in \mathbb{R}^p$ is the output vector, $E\left[\boldsymbol{w}_{k-1}\boldsymbol{w}_{k-1}^\top\right] = Q_{k-1} \in \mathbb{R}^{n_a \times n_a}$, and $E\left[\boldsymbol{v}_k\boldsymbol{v}_k^\top\right] = R_k \in \mathbb{R}^{p \times p}$.
The *residual* vector is defined as $\boldsymbol{\upsilon}_k = \boldsymbol{y}_k - \boldsymbol{h}_k(\boldsymbol{x}_{k|k}) \in \mathbb{R}^p$ and the *innovation* vector is $\boldsymbol{\mu}_k = \boldsymbol{y}_k - \boldsymbol{h}_k(\boldsymbol{x}_{k|k-1}) \in \mathbb{R}^{p \times p}$.

Adaptive estimation of R

For what concerns the estimation of the matrix R, from the equation of the standard UKF, one can obtain

$$S_k = \sum_{i=0}^{2n_a} W_i^{(c)} (\boldsymbol{\mathcal{H}}_i - \hat{\boldsymbol{y}}_{k|k-1})(\boldsymbol{\mathcal{H}}_i - \hat{\boldsymbol{y}}_{k|k-1})^\top + R_k \tag{4.32}$$

and thus

$$R_k = S_k - \sum_{i=0}^{2n_a} W_i^{(c)} (\boldsymbol{\mathcal{H}}_i - \hat{\boldsymbol{y}}_{k|k-1})(\boldsymbol{\mathcal{H}}_i - \hat{\boldsymbol{y}}_{k|k-1})^\top \tag{4.33}$$

where $S_k = E[\boldsymbol{\mu}_k\boldsymbol{\mu}_k^\top]$ can be estimated by averaging it sequence over a moving window. Unfortunately, innovation-based approaches cannot guarantee to generate a positive definite solution for R_k, as it can be seen in Eq.4.33.

As a consequence, residual-based methods are usually employed. Under the hypotheses of the classic linear KF, [Mohamed and Schwarz, 1999] shown that an estimate of R_k can be obtained, exploiting the residual $\boldsymbol{\upsilon}_k$

$$\hat{R}_k = \frac{1}{N_{R_w}} \sum_{i=i_0}^{k} \boldsymbol{\upsilon}_i \boldsymbol{\upsilon}_i^\top + H_k P_{k|k} H_k^\top, \tag{4.34}$$

where H_k is the measurement matrix at the instant k and $E[\boldsymbol{\upsilon}_k \boldsymbol{\upsilon}_k^\top]$ is here approximated (at the instant k) with an average through a moving window of size N_{R_w}. By adopting the EKF approximation, some authors such as, for example, [Jetto et al., 1999] and [Meng et al., 2000] tried to apply the adaptive filtering theory developed for the linear case to the linearized system. Moreover, other authors extended these equations to the UKF estimator; see for example [Zhou et al., 2010] and [Zheng et al., 2018]. In conclusion, Eq.4.34 (with the symbols defined above) becomes:

$$\hat{R}_k = \frac{1}{N_{R_w}} \sum_{i=i_0}^{k} \boldsymbol{\upsilon}_i \boldsymbol{\upsilon}_i^\top + \sum_{i=0}^{2n_a} W_i^{(c)} (\boldsymbol{\mathcal{H}}_i - \hat{\boldsymbol{y}}_{k|k})(\boldsymbol{\mathcal{H}}_i - \hat{\boldsymbol{y}}_{k|k})^\top. \tag{4.35}$$

It is easy to understand that the estimated $\hat{R}_k$ matrix is now positive definite.

Adaptive estimation of Q

For what concerns the estimation of the matrix Q, from Eq.4.31, $\boldsymbol{w}_{k-1} = \boldsymbol{x}_k - \boldsymbol{f}_{k-1}(\boldsymbol{x}_{k-1}, \boldsymbol{u}_{k-1})$ can be obtained. Here, the estimation of $\boldsymbol{w}_{k-1}$, $\hat{\boldsymbol{w}}_{k-1}$ can be approximated with

$$\begin{aligned} \hat{\boldsymbol{w}}_{k-1} = \hat{\boldsymbol{x}}_{k|k} - \boldsymbol{f}_{k-1}(\hat{\boldsymbol{x}}_{k-1|k-1}) \approx \hat{\boldsymbol{x}}_{k|k} - \hat{\boldsymbol{x}}_{k|k-1} = \\ L_k(\boldsymbol{y}_k - \hat{\boldsymbol{y}}_{k|k-1}) \approx L_k \boldsymbol{\mu}_k. \end{aligned} \tag{4.36}$$

The above equations make use of linearization approximations and thus second order terms (and higher) are neglected:

$$\begin{aligned} \hat{\boldsymbol{x}}_{k|k-1} = \boldsymbol{f}_{k-1}(\hat{\boldsymbol{x}}_{k-1|k-1}) + \frac{1}{2} \sum_{i=1}^{n} e_i \,\mathrm{trace} \left[\frac{\partial^2 f_{k-1}^i}{\partial x^2} P_{k-1|k-1} \right] + HOT \approx \\ \boldsymbol{f}_{k-1}(\hat{\boldsymbol{x}}_{k-1|k-1}), \end{aligned} \tag{4.37}$$

where HOT stands for Higher-Order Terms, $\frac{\partial^2 f_{k-1}^i}{\partial x^2}$ is the Hessian of the i-th component of $\boldsymbol{f}_{k-1}$, trace[$\bullet$] is the trace operator, and e_i is the dimensional Cartesian basis vector ($i-th$ component is 1, the others are 0).

$$\hat{\boldsymbol{y}}_{k|k-1} = \boldsymbol{h}_k(\hat{\boldsymbol{x}}_{k|k-1}) + \frac{1}{2}\sum_{i=1}^{n} e_i \,\mathrm{trace}\left[\frac{\partial^2 h_k^i}{\partial x^2} P_{k|k-1}\right] + HOT \approx \boldsymbol{h}_k(\hat{\boldsymbol{x}}_{k|k-1}), \tag{4.38}$$

where HOT stands for Higher-Order Terms, $\frac{\partial^2 h_k^i}{\partial x^2}$ is the Hessian of the i-th component of $\boldsymbol{h}_k$, trace[$\bullet$] is the trace operator, and e_i is the dimensional Cartesian basis vector ($i-th$ component is 1, the others are 0).
Therefore, $Q_{k-1} = E[\boldsymbol{w}_{k-1}\boldsymbol{w}_{k-1}^\top]$ is approximated with

$$Q_{k-1} \approx L_k E[\boldsymbol{\mu}_k \boldsymbol{\mu}_k^\top] L_k^\top \tag{4.39}$$

$E[\boldsymbol{\mu}_k \boldsymbol{\mu}_k^\top]$ is calculated (at the instant k) with an average through a moving window of size N_{Q_w}.

$$\frac{1}{N_{Q_w}} \sum_{i=i_0}^{k} \boldsymbol{\mu}_i \boldsymbol{\mu}_i^\top, \tag{4.40}$$

where $i_0 = k - N_{Q_w} + 1$.
In conclusion, exploiting the above assumptions, an estimate of Q_{k-1} is:

$$\hat{Q}_{k-1} = L_k \frac{1}{N_{Q_w}} \sum_{i=i_0}^{k} \boldsymbol{\mu}_i \boldsymbol{\mu}_i^\top L_k^\top \tag{4.41}$$

It is easy to understand that the estimated $\hat{Q}_{k-1}$ matrix is positive definite.

Proposed solution

The behavior of the AUV is described with the following state variables:

$$\boldsymbol{x} = [\ {}^N\boldsymbol{\eta}_1^T \quad {}^b\boldsymbol{\nu}_1^T\ ]^T, \tag{4.42}$$

with $\boldsymbol{x} \in \mathbb{R}^6$. The model employed for the evolution of the state is strictly causal and a mixture of kinematics and dynamics, where the longitudinal dynamic only is taken into account. In light of Assumptions 1-6, Eq.4.43

can be obtained.

$$\begin{bmatrix} {}^{N}\boldsymbol{\eta}_1 \\ {}^{b}\boldsymbol{\nu}_1 \end{bmatrix}_k = \begin{bmatrix} {}^{N}\boldsymbol{\eta}_1 \\ {}^{b}\boldsymbol{\nu}_1 \end{bmatrix}_{k-1} + \Delta T \begin{bmatrix} {}^{N}R_B^N\left((\boldsymbol{\eta}_2)_{k-1}\right)\left({}^{\boldsymbol{b}}\boldsymbol{\nu}_1\right)_{k-1} \\ \frac{\tau_{1,x}(\boldsymbol{\nu}_{k-1},\mathbf{u}_{k-1})}{m} - \frac{(\delta_x)_{k-1}\nu_{1x}^2\,\mathrm{sgn}(\nu_{1x})}{m} \\ 0 \\ 0 \end{bmatrix} + \boldsymbol{w}_{k-1}, \tag{4.43}$$

where the propulsion model is reported in Eq.4.13, thrusts are linked with the generalized forces $\boldsymbol{\tau}$ with Eq.3.6, ΔT is the (fixed) sampling time of the filter, and δ_x have been already defined in Eq.4.17.

For what concerns longitudinal dynamics, in light of Assumptions 1-6, the damping coefficient $(\delta_x)_{k-1}$ is computed according to the method proposed in Section 4.2.2 and the estimated value can be employed online during an underwater mission, or it can be estimated beforehand using suitable tests.

For what concerns the available measurements and thus the measurement model, the navigation filter can use position measurements either GPS fixes, employed by the vehicle when on the sea's surface in order to initialize the filter or position fixes from a dedicated underwater acoustic localization system (such as an USBL system). In addition to this, depth measurements as well as velocity ones either from the DVL or the FLS as explained in Section 2 can be exploited. During the experimental tests in Section 5, the USBL has never been used, so its presence will be omitted in the rest of the work.

As a consequence, the measurement vector at the k-th time instant is:

$$\boldsymbol{y}_k = \left[\left({}^{N}\boldsymbol{P}_{GPS}\right)^{\top} d_{DS}^{N} \left({}^{b}\boldsymbol{v}_{DVL}\right)^{\top} \vee \left({}^{b}\boldsymbol{v}_{FLS}\right)^{\top} \right]_k^{\top}, \tag{4.44}$$

$\boldsymbol{y} \in \mathbb{R}^6$, and $\vee$ denotes the OR logical operator. As already stated, the navigation filter works at a fixed sampling time of $\Delta T = 0,1$ s (in other words, the operative frequency of the filter is 10 Hz). During a given time interval, more than one instrument could provide a measurement that affects the same physical quantity. In other words, for example, during $t \in [t_{k-2}, t_{k-1})$ both the DVL and the FLS might produce speed measurements. In such a situation, how to select which instrument to favor becomes necessary. The answer to this problem is not unique since both the more accurate device or the most reliable measurement could be rewarded. The proposed solution

is to promote the temporally closest information.
From Eq.4.44, it is easy to understand that direct measurements of the components state vector $\boldsymbol{x}$ are present. As a consequence, the measurement equation is affine with respect to $\boldsymbol{x}$; in particular, it can be expressed as:

$$\boldsymbol{y}_k = H_k \boldsymbol{x}_k + \boldsymbol{v}_k, \tag{4.45}$$

where matrix H_k is time-variant, and it contains only 1 or 0 elements according to the presence of the corresponding measurement. Here, the measurement noise is a zero-mean stationary white noise. Moreover, zero cross-correlation is assumed among the initial state and process and measurement noises. Lastly, it is worth noting that the model present in Eq.4.43 with the thrust defined in Eq.4.13 and Eq.3.6 is nonlinear and non-differentiable (note for example the presence of the sign functions and the piecewise function $g(\bullet)$ defined in Eq.4.4), so the adoption of the UKF, which is known to be a derivative-free estimation algorithm, is proposed. More information concerning the UKF, already adopted by the UNIFI DIEF in the last years, can be found in [Allotta et al., 2015a], [Allotta et al., 2016b], [Costanzi et al., 2019], and [Fanelli, 2019]. The initial expression of R, namely R_1, is supposed as diagonal of the form:

$$R_1 = \text{diag}([R_{GPS}; R_{DS}; R_{DVL} \vee R_{FLS}]_1), \tag{4.46}$$

where $diag(\bullet)$ denotes the diagonal operator, and each term represents the measurement noise of each device and where each single noise matrix is assumed as diagonal, thus neglecting the coupling terms. It is worth noting that in absence of an adaptive strategy as in the AUKF solution, Eq.4.47 holds:

$$R_k = \text{diag}([R_{GPS}; R_{DS}; R_{DVL} \vee R_{FLS}]_k), \tag{4.47}$$

The same reasoning can be made for Q. It can be demonstrated that, assuming an acceleration white noise with zero mean and covariance:

$$Q_{acc} = \begin{bmatrix} q & 0 & 0 \\ 0 & q & 0 \\ 0 & 0 & q_z \end{bmatrix} \text{ with } q_{ii} \in \mathbb{R}^+, i = 0, 1, 2. \tag{4.48}$$

and neglecting roll and pitch angle (approximating them with zero), the general expression of Q (given the state representation in Eq.4.43) becomes:

$$Q_k = \begin{bmatrix} \frac{\Delta T^4}{4}q & 0 & 0 & \frac{\Delta T^3}{2}qcos(\phi) & -\frac{\Delta T^3}{2}qsin(\phi) & 0 \\ 0 & \frac{\Delta T^4}{4}q & 0 & \frac{\Delta T^3}{2}qsin(\phi) & \frac{\Delta T^3}{2}qcos(\phi) & 0 \\ 0 & 0 & \frac{\Delta T^4}{4}q_z & 0 & 0 & \frac{\Delta T^3}{2}q_z \\ \frac{\Delta T^3}{2}qcos(\phi) & \frac{\Delta T^3}{2}qsin(\phi) & 0 & \Delta T^2 q & 0 & 0 \\ -\frac{\Delta T^3}{2}qsin(\phi) & \frac{\Delta T^3}{2}qcos(\phi) & 0 & 0 & \Delta T^2 q & 0 \\ 0 & 0 & \frac{\Delta T^3}{2}q_z & 0 & 0 & \Delta T^2 q_z \end{bmatrix}, \tag{4.49}$$

where ϕ is the yaw angle, and ΔT is the fixed sampling time. It is worth noting that in the absence of an adaptive strategy as in the AUKF solution, the same expression for Q_k holds.

Given the treatment about adaptive filtering, the followed approach is to test if, effectively, the filter is consistent and afterward apply a suitable adaptation to prior filter statistics. By analogy with Kalman filtering theory in the linear case, the innovation process $\boldsymbol{\mu}_k$ is hypothesized to be well described by a zero-mean white sequence. A similar assumption, exploited in a nonlinear scenario (even if applied to a EKF-based estimator) can be found in [Jetto et al., 1999]. Therefore, in such a condition, Eq.4.50 provides a measure of the consistency of the filter, which is necessary for its optimality.

$$(\varphi_\chi)_k = \boldsymbol{\mu}_k^\top S_k^{-1} \boldsymbol{\mu}_k, \tag{4.50}$$

with $(\varphi_\chi)_k \in \mathbb{R}$ with a χ^2_ς distribution where ς denotes the degrees of freedom (equal to the dimension of the vector $\boldsymbol{\mu}_k$). The following test is well known in the literature as Normalized Innovation Squared (NIS) test (see [Bar-Shalom et al., 2004] for more information).
As a consequence, the hypothesis H_0: "innovation $\boldsymbol{\mu}$ with magnitude commensurate with the covariance delivered by the filter" is investigated. In particular, if a mismatching is willed to be detected with a reliability level of ϱ, where ϱ is a parameter chosen by the designer, then there is a value $\overline{\chi}^2_{\varsigma,\varrho}$ (given ς and ϱ), such that, if:

$$(\varphi_\chi)_k > \overline{\chi}^2_{\varsigma,\varrho}, \tag{4.51}$$

then a failure is present. A similar approach can be found, for example, in [Hajiyev and Soken, 2014]. In conclusion, if Eq.4.51 holds, an adaptation of the prior statistics R and/or Q is pursued.

During standard operations, because of various sampling rates of the available sensors, the structure of the matrix H_k might change at each iteration. Furthermore, during real tests at sea, the sampling rate of an instrument may vary according to the state of the sea bottom, being not able to produce reliable measurements. This fact, widely known in the literature for the DVL (see [Miller et al., 2010]) it is even more true for the FLS. Indeed, as already shown in Section 4.1, if the sea bottom presents poor informative content FLS can be hardly used in navigation aiding.
The proposed AUKF solution (see Eq.4.35, Eq.4.41) tacitly assumes that all the measurements are available at each iteration. In [Davari and Gholami, 2016], when measurements are not available at the iteration k, the corresponding quantities of the innovation vector $\boldsymbol{\mu}_k$ are replaced with their previous values. Even if proven to be satisfying reliable, showing good results, it does not seem adequate for our situation, being not able to know in advance, for example, the rate of FLS-based linear speed estimations. Hence, a different approach is pursued.
If one or more measurements are not available at the iteration k, the corresponding rows of the innovation vectors $\boldsymbol{\mu}_k$ and $\boldsymbol{\upsilon}_k$ are replaced with zero. This way, only current measurements give contributions. On the other hand, consequently, the arithmetic mean has to be modified in order to account for the actual measurements story inside the moving window.
In conclusion, Eq.4.35 is substituted with Eq.4.52:

$$\hat{R}_k = [\sum_{i=i_0}^{k} \hat{\boldsymbol{\upsilon}}_i \hat{\boldsymbol{\upsilon}}_i{}^{\top}] \div [N^{\star}_{R_w}] + \sum_{i=0}^{2n_a} W_i^{(c)} (\boldsymbol{\mathcal{H}}_i - \hat{\boldsymbol{y}}_{k|k})(\boldsymbol{\mathcal{H}}_i - \hat{\boldsymbol{y}}_{k|k})^{\top}, \tag{4.52}$$

where $\div$ represents the element-wise division,

$$\upsilon_i^{j\star} = \begin{cases} \upsilon_i^j & H_i^j \neq 0_{1\times n_a} \\ 0 & H_i^j = 0_{1\times n_a} \end{cases} \tag{4.53}$$

with the superscript is denoted the $j-th$ row.

$$N^{\star}_{R_w} = \sum_{i=i_0}^{k} \boldsymbol{I}_{yi} \boldsymbol{I}_{yi}^{T}, \tag{4.54}$$

where $\boldsymbol{I}_{yi}$ at the instant i is a column vector whose rows are 1 if the corresponding measurement has arrived or 0 otherwise and $k = N_{R_w} + i_0 - 1$.

The same modifications are applied to Eq.4.41, leading to Eq.4.55.

$$\hat{Q}_{k-1} = L_k \sum_{i=i_0}^{k} [\boldsymbol{\mu}^{\star}_i \boldsymbol{\mu}^{\star^{\top}} \div N^{\star}_{Q_w}] L_k^{\top}, \tag{4.55}$$

where $\div$ represents the element-wise division,

$$\mu_i^{j^{\star}} = \begin{cases} y_i^j - H_i^j \boldsymbol{x}_{i|i-1} & H_i^j \neq 0_{1\times 6} \\ 0 & H_i^j = 0_{1\times 6} \end{cases} \tag{4.56}$$

with the superscript is denoted the $j-th$ row.

$$N^{\star}_{Q_w} = \sum_{i=i_0}^{k} \boldsymbol{I}_{yi} \boldsymbol{I}_{yi}^{T}, \tag{4.57}$$

where $\boldsymbol{I}_{yi}$ at the instant i is a column vector whose rows are 1 if the corresponding measurement has arrived or 0 otherwise and $k = N_{Q_w} + i_0 - 1$. In conclusion, the proposed AUKF-based solution is summarized in Fig.4.21 and its complete pseudo-code is reported in Algorithm 2 ($\wedge$ denotes the AND logical operator)

Algorithm 2 AUKF Algorithm

Algorithm:

Function `AUKF() /* Algorithm implementation */`

Step `Prediction() /* Prediction step */`

Input : $\hat{\boldsymbol{x}}_{k-1|k-1}, P_{k-1|k-1}, \boldsymbol{f}(\bullet)_{k-1}$

Output: $\hat{\boldsymbol{x}}_{k|k-1}, P_{k|k-1}$

$(\hat{\boldsymbol{x}}_{k|k-1}, \overline{P}_{k|k-1}) = UT(\hat{\boldsymbol{x}}_{k-1|k-1}, P_{k-1|k-1}, \boldsymbol{f}(\bullet)_{k-1})$

$P_{k|k-1} = \overline{P}_{k|k-1} + Q_{k-1}$

end

Step `Correction() /* Correction step */`

Input : $\hat{\boldsymbol{x}}_{k|k-1}, P_{k|k-1}, \boldsymbol{h}(\bullet)_k$

Output: $\hat{\boldsymbol{x}}_{k|k}, P_{k|k}$

$(\hat{\boldsymbol{y}}_{k|k-1}, \overline{S}_k, P_k^{xy}) = UT(\hat{\boldsymbol{x}}_{k|k-1}, P_{k|k-1}, \boldsymbol{h}(\bullet)_k)$

$S_k = \overline{S}_k + R_k$

$L_k = P_k^{xy} S_k^{-1}$

$\boldsymbol{\mu}_k = \boldsymbol{y}_k - \hat{\boldsymbol{y}}_{k|k-1}$

$\hat{\boldsymbol{x}}_{k|k} = \hat{\boldsymbol{x}}_{k|k-1} + L_k \boldsymbol{e}_k$

$P_{k|k} = P_{k|k-1} - L_k S_k L_k^\top$

end

Step `Consistency Check() /* Consistency Check (NIS test) */`

Input : $\boldsymbol{\mu}_k, S_k$

Output: $\mathcal{C}_{status_k}$

if $(\varphi_\chi)_k = \boldsymbol{\mu}_k S_k \boldsymbol{\mu}_k^\top > \overline{\chi}^2_{\varsigma,\varrho}$ **then**

$\mathcal{C}_{status_k} = false$

end

else

$\mathcal{C}_{status_k} = true$ **return**

end

end

Step `Q Adjustment() /* Q Adjustment */`

Input : $\mathcal{C}_{status_k}, N_{Q_w}, N^\star_{Q_w}, \boldsymbol{\mu}_i^\star|_{i=i_0,\ldots,k}, \boldsymbol{y}_{k|k}$

Output: Q_k

if $\mathcal{C}_{status_k} = false \wedge k \geq N_{Q_w}$ **then**

$\hat{Q}_k = L_k \sum_{i=i_0}^{k} [\boldsymbol{\mu}_i^\star \boldsymbol{\mu}^{\star\top} \div N^\star_{Q_w}] L_k^\top$

end

else

$Q_k = Q_{k-1}$ **return**

end

end

Step `R Adjustment() /* R Adjustment */`

Input : $\mathcal{C}_{status_k}, N_{R_w}, N^\star_{R_w}, \boldsymbol{\upsilon}_i^\star|_{i=i_0,\ldots,k}, \boldsymbol{y}_{k|k}$

Output: $\hat{R}_{k+1}$

if $\mathcal{C}_{status_k} = false \wedge k \geq N_{R_w}$ **then**

$\hat{R}_{k+1} = [\sum_{i=i_0}^{k} \boldsymbol{\upsilon}_i^\star \boldsymbol{\upsilon}_i^{\star\top}] \div [N^\star_{R_w}] + \sum_{i=0}^{2n_a} W_i^{(c)} (\boldsymbol{\mathcal{H}}_i - \hat{\boldsymbol{y}}_{k|k})(\boldsymbol{\mathcal{H}}_i - \hat{\boldsymbol{y}}_{k|k})^\top$

end

else

$R_{k+1} = R_k$ **return**

end

end

end

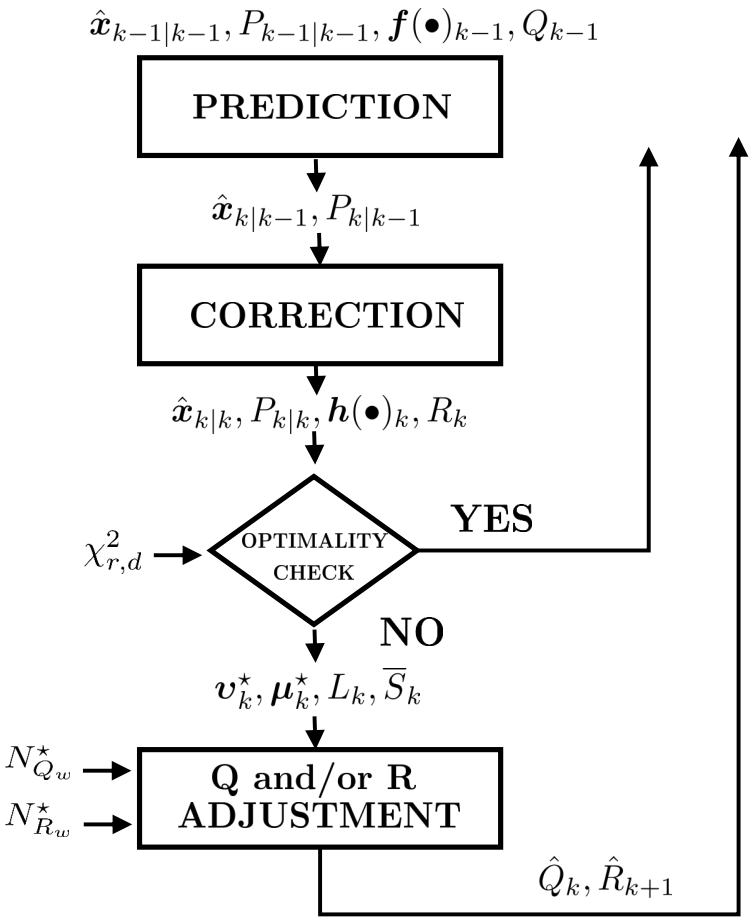

Figure 4.21: The proposed AUKF-based solution workflow.

Chapter 5

Results

This chapter is divided in two parts. First, the navigation solution presented in Chapter 4 is validated offline through the use of navigational data obtained during sea trials undertook in La Spezia (Italy) at the NATO STO CMRE in July 2018; thus, all the results are obtained in post-processing. Second, real and online autonomous underwater missions (described in Section 5.2) were performed in La Spezia (Italy) in May 2019 within the activities of the SEALab, the joint research laboratory between the CSSN of the Italian Navy and ISME, and at Vulcano Island, Messina (Italy) in June 2019 (both in the framework of the European project EUMR).

5.1 Offline validation

The results reported in this section refer to the navigation data retrieved during an underwater mission performed at the ERL SAUC-E competition held in La Spezia (Italy) in July 2018. The mission was executed at the desired depth of 2 m with a reference longitudinal cruise speed of 0.5 m/s, lasting 960 s and covering approximately 220 m. Besides, the FLS range was set to 10 m. The altitude was approximately constant and equal (more or less) to 2 m. Water current measurements were not available during the day of the trial, but, on the other hand, the test site described here is a small basin at the NATO STO CMRE, where water currents are usually of low intensity and thus negligible.
The area of interest was a rectangle with the approximate dimensions 36×20 m (see Fig.5.2). The underwater scenario presented both areas where the

sea bottom contained a high informative content (two underwater structures, each approximately 2.2×3.2×1.2 m composed of underwater plastic pipes, were positioned on the sea bottom by the competition organizers, see Fig. 5.1, with some metallic chains also present), and regions where the seafloor was unaltered and flat. The same data set has been employed by the author in [Franchi et al., 2019a].

Figure 5.1: One of the two underwater structures placed on the sea bottom by the competition organizers.

FeelHippo AUV relied on the sensors and the payload described in Section 2.2 for the extent of the mission, and it performed the required navigation tasks by exploiting a DVL-based DR strategy. Moreover, GPS fixes were acquired before diving and after resurfacing. The DVL-based underwater navigation strategy as well as the GPS fixes were used as high-resolution position data, to validate the proposed FLS-based solution. It is useful to highlight that although the used benchmark does not provide an absolute positioning system (except from GPS fixes before diving and after surfacing), the navigation appears reliable because of the small error after resurfacing (around 3.5 m, see Fig.5.3, Fig.5.4, Fig.5.5, Fig.5.6, Fig.5.7), and Fig.5.8 where the relative value is less than 2% after about 16 minutes of autonomous navigation.
To highlight the different peculiarities of the following navigation approaches, the next part of the section is divided into units and each one emphasizes a different navigation strategy. In particular, first of all (Section 5.1.1), a simple model-based technique is proposed, where the dynamics of the vehicle is described in Eq.4.1 and Eq.4.2 and two different propulsion models are considered: the one described in Eq.4.3 and its modified version, where

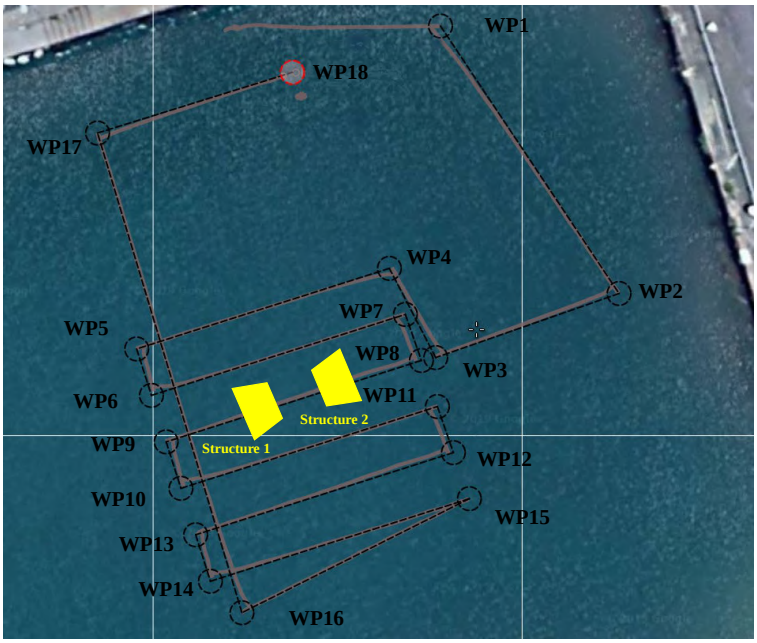

Figure 5.2: Google Earth image of the NATO STO CMRE basin (La Spezia, Italy). The two underwater structures placed on the sea bottom by the competition organizers are schematically depicted in yellow, whereas the waypoints of the underwater mission are indicated with WP.

the effects of the dead-zone are taken into account, see Eq.4.13. Second of all, an FLS-based DR strategy, with speed estimation computed as reported in Section 4.1, is described in Section 5.1.2. Finally, an FLS-based UKF strategy, together with its adaptive version AUKF is shown in Section 5.1.3. FLS-based linear speed estimations are computed as in Section 4.1 and the estimators are described in Section 4.3.
Finally, in Section 5.1.4 all the above-mentioned solutions are quantitatively compared (all together) with a high-resolution position data used as benchmark.

5.1.1 Model-based navigation strategy

In this section the aim is to show how a simple model-based navigation, even in a scenario with reduced sea currents (indeed the test site described here is a small basin at the NATO STO CMRE where water currents are usually of low intensity), cannot adequately describe the motion of an AUV, leading to undesired position-error drifts. In addition to this, the author wants to

FeelHippo AUV main parameters involved in the dynamic model	
δ_x [N/s^{2}m^2]	65
Propeller pitch (p_p) [m/rev]	0.094
Forward bollard coefficient k^+ [Ns^2]	0.0128
Backward bollard coefficient k^- [Ns^2]	-0.008753
Forward dead-zone boundary limit u^+_{rpm} [Hz]	$4.8833 + 0.5866(\mathcal{V} - 14)$
Backward dead-zone boundary limit u^-_{rpm} [Hz]	$-4.8167 - 0.5974(\mathcal{V} - 14)$

Table 5.1: Main parameters involved in the dynamics of FeelHippo AUV.

emphasize how a propulsion model that takes into account the presence of dead-zone can improve navigation performance in case of the unavailability of direct rotational speed measurements for the thrusters. In Tab.5.1 the main parameters involved in the dynamics of AUV are summarized , whereas the navigation results are given in Fig.5.3 and Fig.5.4.

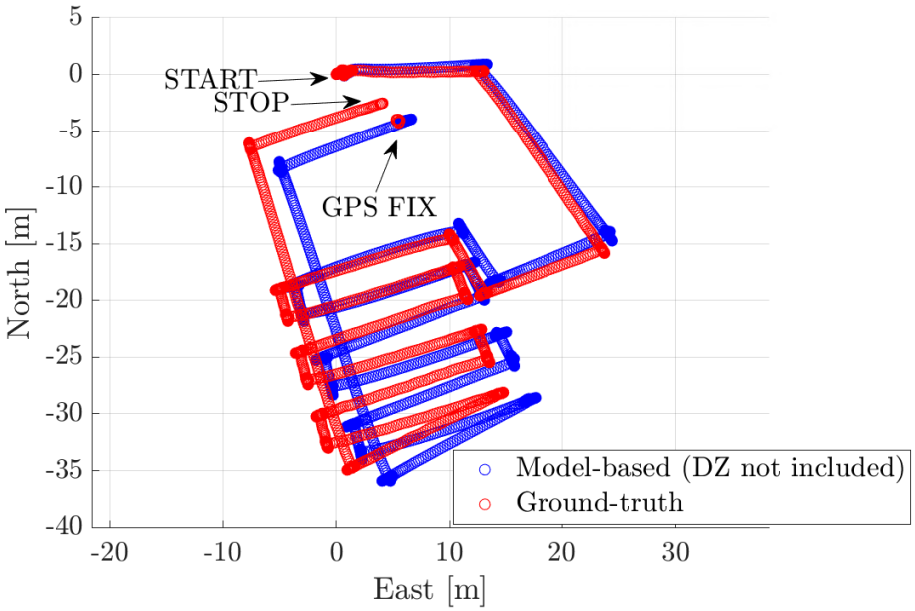

Figure 5.3: Navigation results exploiting solely model-based speed estimations. The high-resolution position data path is in red, and the proposed solution is in blue. "START" and "STOP" indicate the first and last (underwater) point of the high-resolution position data path, respectively, whereas "GPS FIX" stands for the position obtained after resurfacing and "DZ" means dead-zone. For the sake of brevity high-resolution position data is indicated with "Ground-truth".

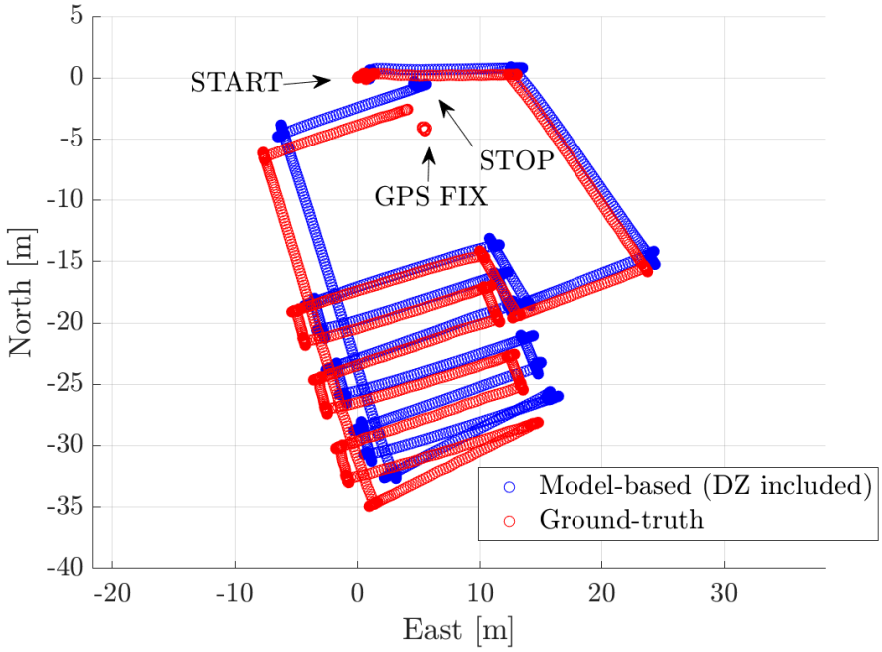

Figure 5.4: Navigation results exploiting solely model-based speed estimations. The high-resolution position data path is in red, and the proposed solution is in blue. "START" and "STOP" indicate the first and last (underwater) point of the high-resolution position data path, respectively, whereas "GPS FIX" stands for the position obtained after resurfacing and "DZ" means dead-zone. For the sake of brevity high-resolution position data is indicated with "Ground-truth".

5.1.2 DR strategy

In this section are reported the results when the vehicle uses an FLS-based DR strategy (see Fig.5.5), whereas the main parameters involved in speed estimation by means of the FLS are outlined in Tab.5.2. Here, the presented technique tries to exploit (primarly) FLS measurements and model-based estimations only possess a complementary role in case of unavailability of linear speed measurements from the FLS. For what concerns the dynamic model, please refer to Tab.5.1. By observing Tab.5.2, it can be noted how

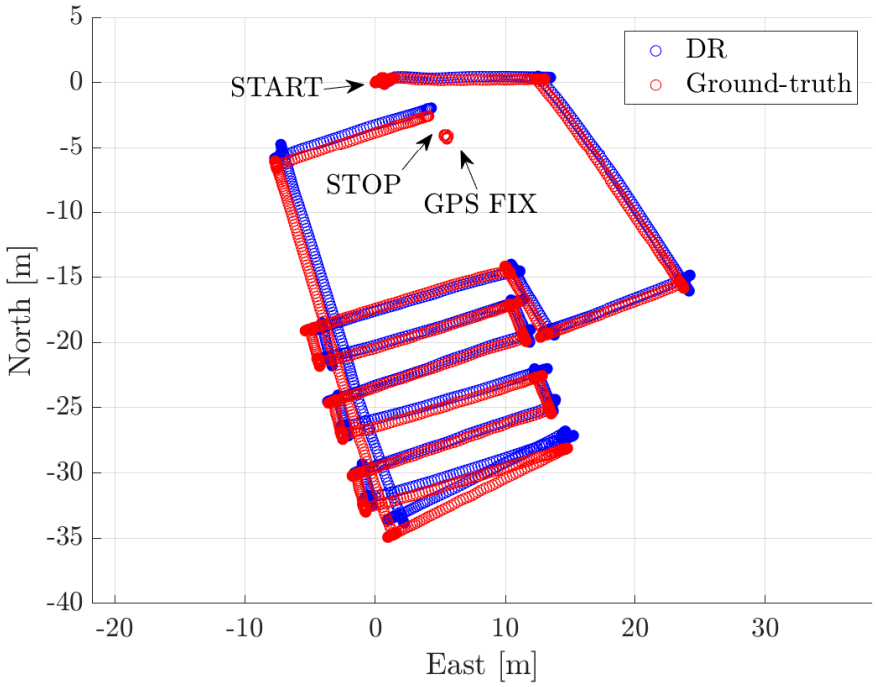

Figure 5.5: Navigation results for the FLS-based DR solution. The high-resolution position data path is in red, and the proposed solution is in blue. "START" and "STOP" indicate the first and last (underwater) point of the high-resolution position data path, respectively, whereas "GPS FIX" stands for the position obtained after resurfacing. For the sake of brevity high-resolution position data is indicated with "Ground-truth".

the coefficient c_r (see Eq.4.9) presents a value very close to 1. Indeed, a simple DR strategy weights in the same way every FLS measurement as well as every model prediction and thus no probabilistic description is included. In order to prevent the inclusion of unreliable FLS-based linear speed mea-

FLS-based linear speed estimation	
Acceptance threshold c_r	0.95
LP filter cut-off frequency(D_0) [pixel]	60
LP filter order l	3
$\frac{R_{\rightarrow MAX}}{h}$ [pixel/m]	470.6 (range at 10 m)

Table 5.2: Main parameters involved in linear speed estimation by means of the FLS.

surements, the coefficient c_r needs to be maintained at high values. In conclusion, the navigation filter needs to possess the most reliable (according to Eq.4.9) measurements only. On the other hand, this approach (especially in underwater scenario with low informative content) could discard too many FLS contributions.

5.1.3 UKF and AUKF strategy

The main goal of this section is to highlight how an adaptive description can improve the overall navigational performance. If, on the one hand, a probabilistic description of the problem (by means, in this case, of an UKF estimator) permits to weight in a different way measurements and model predictions, on the other hand, how to define a prior statistics for FLS-based contribution arises. Some authors, such as [Pfingsthorn et al., 2010] and [Hurtós et al., 2015], proposed heuristic methods where the underlying idea is that the surrounding of the main peak of the matrix $c(x, y)$ (see Eq.3.46) can represent the accuracy of the phase correlation method. Nevertheless, this way of thinking is purely heuristic, and it is prone to provide, according to the definition of "the surrounding of the main peak", different results. The navigation results are reported in Fig.5.6 and Fig.5.8 for two UKF solutions and the AUKF estimator respectively. In the first one (henceforth called "UKF 1"), the matrix R and Q are initialized as for the AUKF and the goal is to highlight how a "wrong" prior statistics can worsen the overall performance and how an AUKF strategy can overcome this issue. In the second one (henceforth called "UKF 2"), the UKF is finely tuned (using a trial-and-error procedure), but it is shown that anyway the AUKF strategy

outperforms it. Indeed, a static approach for the prior statistics is not able to adapt the filter behavior to a mutable underwater scenario.

UKF 1

In this test the matrix R as well the matrix Q are static and equal to their initial value (see Tab.5.3). The navigation results are reported in Fig.5.6, whereas the parameters involved for the UKF are summarized in Tab.5.3.

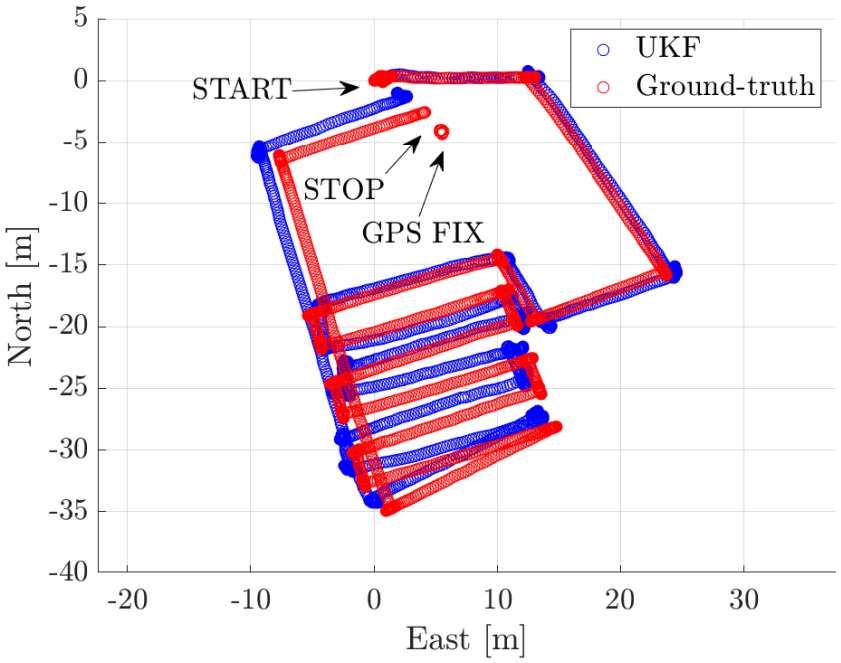

Figure 5.6: Navigation results for the UKF 1 estimator. The high - position data path is in red, and the proposed solution is in blue. “START” and “STOP” indicate the first and last (underwater) point of the high-resolution position data path, respectively,l whereas “GPS FIX” stands for the position obtained after resurfacing. For the sake of brevity high-resolution position data is indicated with “Ground-truth”.

UKF 1 simulation main parameters	
q [m^2/s^4]	0.001
q_z [m^2/s^4]	0.1
R	$\begin{bmatrix} 0.1 & 0 & 0 & 0 & 0 \\ 0 & 0.1 & 0 & 0 & 0 \\ 0 & 0 & 0.01 & 0 & 0 \\ 0 & 0 & 0 & 0.00001 & 0 \\ 0 & 0 & 0 & 0 & 0.00001 \end{bmatrix}$
Acceptance threshold c_r	0.80
LP filter cut-off frequency (D_0) [pixel]	60
LP filter order l	3
$\frac{R_{\rightarrow MAX}}{h}$ [pixel/m]	470.6 (range at 10 m)

Table 5.3: Main parameters involved in the UKF 1 simulation.

UKF 2

In this test, the matrix Q is not modified with respect to the previous one, whereas the matrix R has been changed (according to a trial-and-error procedure) to find an acceptable tuning. The navigation results are reported in Fig.5.7, whereas the parameters involved for the UKF are summarized in Tab.5.4.

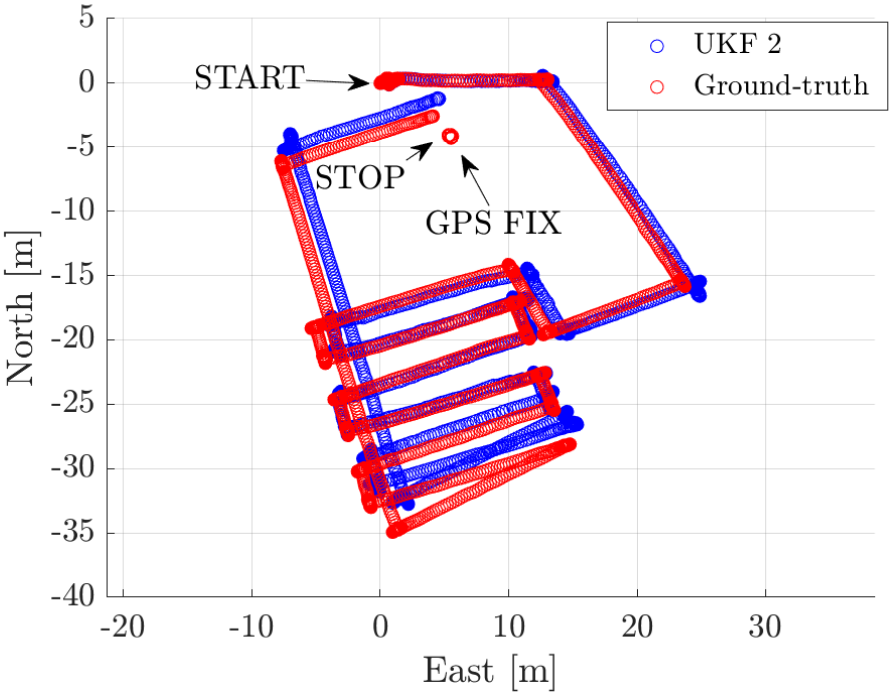

Figure 5.7: Navigation results for the UKF 2 estimator. The high-resolution position data path is in red, and the proposed solution is in blue. "START" and "STOP" indicate the first and last (underwater) point of the high-resolution position data path, respectively, whereas "GPS FIX" stands for the position obtained after resurfacing. For the sake of brevity high-resolution position data is indicated with "Ground-truth".

UKF 2 simulation main parameters	
q [m^2/s^4]	0.001
q_z [m^2/s^4]	0.1
R	$\begin{bmatrix} 0.1 & 0 & 0 & 0 & 0 \\ 0 & 0.1 & 0 & 0 & 0 \\ 0 & 0 & 0.01 & 0 & 0 \\ 0 & 0 & 0 & 0.00004 & 0 \\ 0 & 0 & 0 & 0 & 0.00006 \end{bmatrix}$
Acceptance threshold c_r	0.80
LP filter cut-off frequency (D_0) [pixel]	60
LP filter order l	3
$\frac{R \rightarrow_{MAX}}{h}$ [pixel/m]	470.6 (range at 10 m)

Table 5.4: Main parameters involved in the UKF 2 simulation.

AUKF

For what concerns the AUKF approach, the adaptive law presented in Eq.4.41 has often produced poor performance. In particular, it has shown to be very sensitive to the particular measurement history on the moving window of size N_{Q_w}, leading to sharp trends in the system state. As a consequence, an adaptation for what concerns matrix R only is presented in the following, whereas matrix Q is constrained to the structure given in Eq.4.49. Besides, for what concerns the value of N_{R_w}, the chosen value represents a trade-off between two different situations. Indeed, a large estimation window lessens the ability of the algorithm to sense high-frequency aspects, and since FLS estimations may present temporal gaps, too distant (in time) measurements could be considered together. On the other hand, the larger the estimation window, the more the average moving window approximation (see Eq.4.34 and Eq.4.41) holds. The parameters involved for the AUKF are summarized in Tab.5.5.

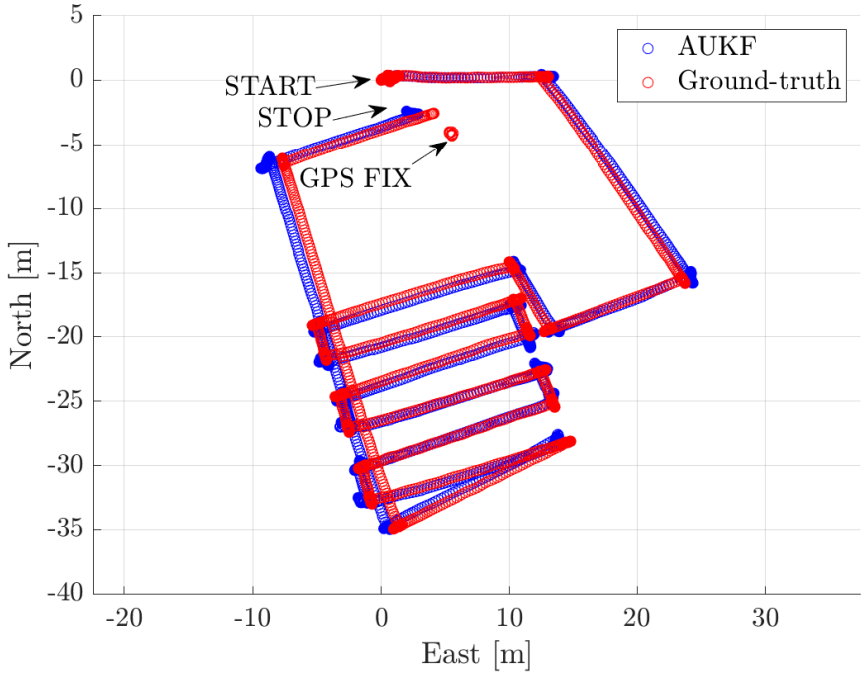

Figure 5.8: Navigation results for the AUKF estimator. The high-resolution position data path is in red, and the proposed solution is in blue. "START" and "STOP" indicate the first and last (underwater) point of the high-resolution position data path, respectively, whereas "GPS FIX" stands for the position obtained after resurfacing. For the sake of brevity high-resolution position data is indicated with "Ground-truth".

AUKF simulation main parameters	
Reliability level fault detection ϱ	0.75
q [m^2/s^4]	0.001
q_z [m^2/s^4]	0.1
N_{R_w}	15
R_1	$\begin{bmatrix} 0.1 & 0 & 0 & 0 & 0 \\ 0 & 0.1 & 0 & 0 & 0 \\ 0 & 0 & 0.01 & 0 & 0 \\ 0 & 0 & 0 & 0.00001 & 0 \\ 0 & 0 & 0 & 0 & 0.00001 \end{bmatrix}$
Acceptance threshold c_r	0.60
LP filter cut-off frequency (D_0) [pixel]	60
LP filter order l	3
$\frac{R_{\rightarrow MAX}}{h}$ [pixel/m]	470.6 (range at 10 m)

Table 5.5: Main parameters involved in the AUKF simulation.

5.1.4 All against all comparison

With the aim of giving a more quantitative contribution, the high-resolution position data reference has been compared, by means of the metrics defined in Eq.5.1 and Eq.5.2, with each solution presented in Section 5.1. The final results are depicted in Fig.5.9 and Fig.5.10, where it can be easily noted how FLS-based speed measurements improve the overall performance.

$$e_k = \left\| \boldsymbol{\eta}_{1_{HR_k}} - \boldsymbol{\eta}_{1_{TS_k}} \right\| \tag{5.1}$$

$$\bar{e}_k = \frac{\sum_{i=0}^{i=k} e_i}{k}, \tag{5.2}$$

where $e_k \in \mathbb{R}^+$ denotes the navigation error at the instant $k \in \mathbb{N}$, $\boldsymbol{\eta}_{1_{HR_k}}$ and $\boldsymbol{\eta}_{1_{TS_k}}$ indicate the position of the AUV at the instant k with respect to a $\{O^N x^N y^N z^N\}$ NED frame, according to (respectively) the high-resolution position data reference and to the current tested solution, and $\bar{e}_k \in \mathbb{R}^+$ is the mean of all the computed errors e_k.

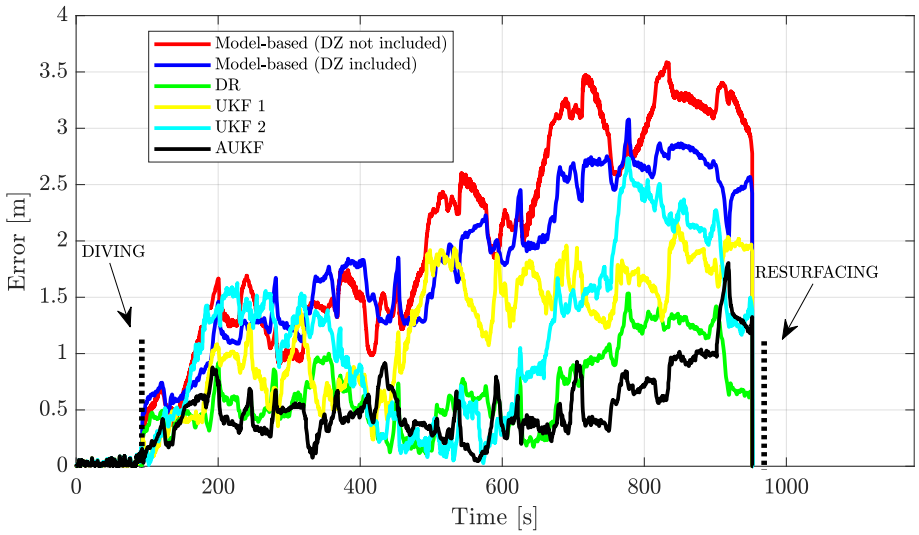

Figure 5.9: Current error for the tested solutions as defined in Eq.5.1. During the first (more or less) 100 s, the error is zero because FeelHippo AUV is on surface, and the GPS signal is used.

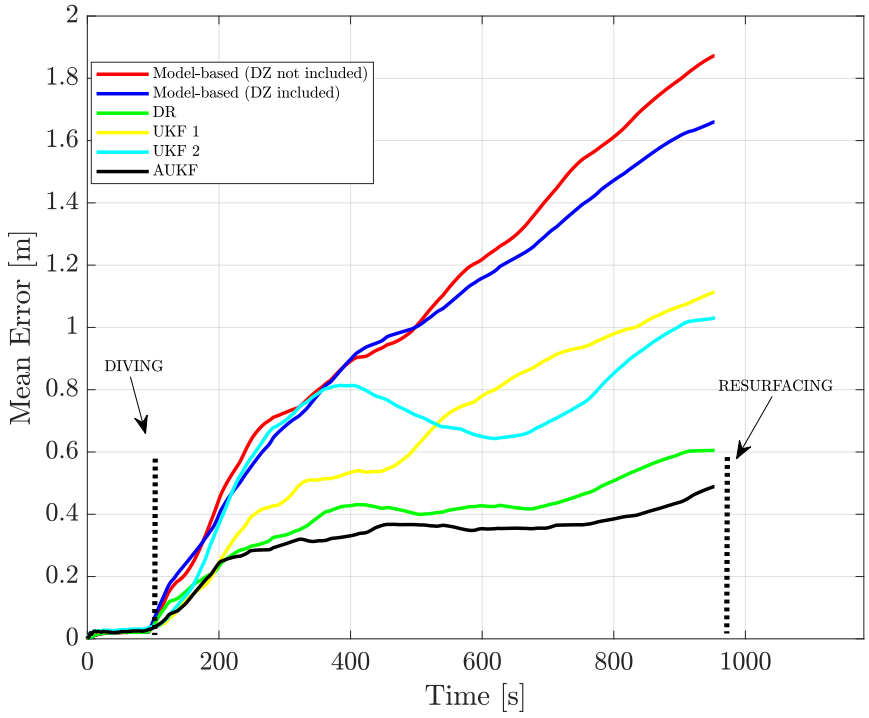

Figure 5.10: Mean error over time for the tested solutions, as defined in Eq.5.2. It can be easily noticed how the presence of FLS measurements bounds the error drift and how the AUKF solution outperforms all the others.

5.2 Online underwater tests

The results reported in this section present two autonomous underwater missions performed at sea in the framework of the European project EUMR. The first one was conducted in La Spezia (Italy) within the activities of the SEALab, the joint research laboratory between the CSSN of the Italian Navy and ISME, and the second one at Vulcano Island, Messina (Italy). The following tests involved FeelHippo AUV but, on the other hand, since the proposed solution is not tailored to a particular vehicle, its results can be deemed as general, and future developments will involve the testing of the navigation strategy on the other members of the UNIFI DIEF MDM Lab fleet (see Chapter 2).

5.2.1 CSSN basin

The first experiment is an underwater mission performed during EUMR tests in La Spezia (Italy) within the activities of the SEALab, the joint research laboratory between the CSSN of the Italian Navy and ISME, on the 30^{th} of May 2019. The mission was executed at the desired depth of 1.5 m with a reference longitudinal cruise speed of 0.5 m/s, and it lasted 250 s covering approximately 100 m. Besides, the FLS range was set to 10 m. The altitude ranged from 1 m to 3 m during the underwater mission. The planned underwater mission at the test site is visible in Fig.5.11. The navigation path

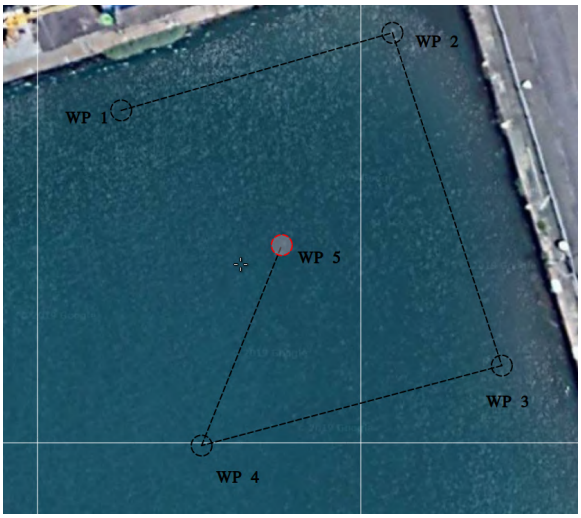

Figure 5.11: Google Earth image of the CSSN basin, La Spezia (Italy) overlaid with the planned autonomous underwater mission. The waypoints are indicated with WP.

of the AUKF solution (compared with a DVL-based DR high-resolution position data reference) is in Fig.5.12, whereas a quantitative comparison, by means of the metrics defined in Eq.5.1, is depicted in Fig.5.13. The parameters involved for the AUKF are summarized in Tab.5.6.

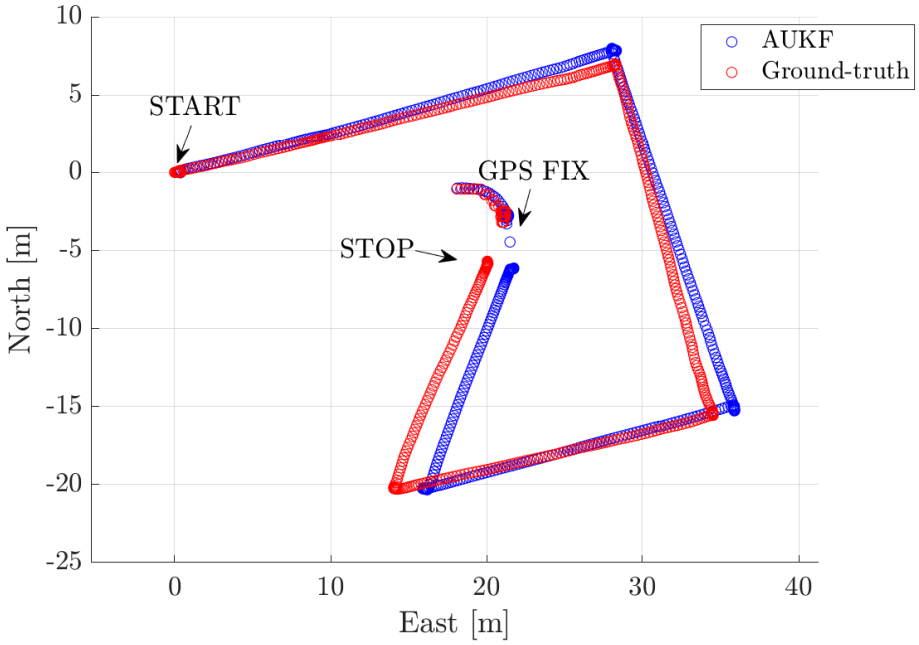

Figure 5.12: Navigation results for the AUKF estimator at the CSSN basin La Spezia (Italy). The high-resolution position data path is in red and the proposed solution in blue. "START" and "STOP" indicate the first and last (underwater) point of the high-resolution position data path, respectively, whereas "GPS FIX" stands for the position obtained after resurfacing. The resurfacing error is around 3 m. For the sake of brevity high-resolution position data is indicated with "Ground-truth".

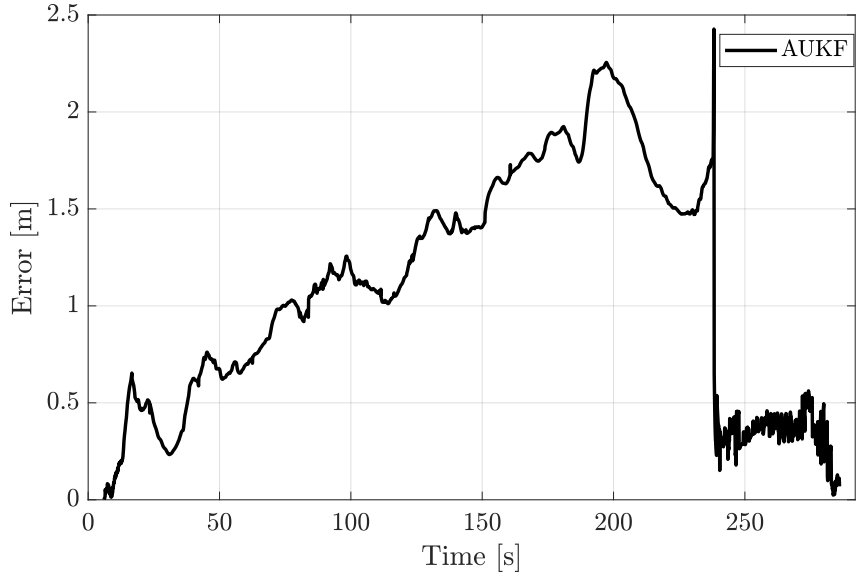

Figure 5.13: Error for the AUKF solution as defined in Eq.5.1. After resurfacing, which is around 240 s, a difference between the high-resolution position data reference and the AUKF solution is present. The former is the raw GPS signal, whereas the latter is the positional output of the AUKF proposal, where the dynamic model and the GPS signal are fused.

AUKF simulation main parameters	
Reliability level fault detection ϱ	0.75
q [m^2/s^4]	0.001
q_z [m^2/s^4]	0.1
N_{R_w}	15
R_1	$\begin{bmatrix} 0.1 & 0 & 0 & 0 & 0 \\ 0 & 0.1 & 0 & 0 & 0 \\ 0 & 0 & 0.01 & 0 & 0 \\ 0 & 0 & 0 & 0.00001 & 0 \\ 0 & 0 & 0 & 0 & 0.00001 \end{bmatrix}$
Acceptance threshold c_r	0.60
LP filter cut-off frequency (D_0) [pixel]	60
LP filter order l	3
$\frac{R \rightarrow_{MAX}}{h}$ [pixel/m]	470.6 (range at 10 m)

Table 5.6: Main parameters involved in the autonomous underwater mission at the CSSN basin La Spezia (Italy).

5.2.2 Vulcano Island Bay

The second experiment is an underwater mission performed during EUMR tests at Negro Bay, Vulcano Island (Italy) on the 11^{th} of June 2019. The mission was executed at the desired depth of 0.5 m with a reference longitudinal cruise speed of 0.5 m/s, and it lasted around 350 s covering approximately 150 m. Besides, the FLS range was set to 10 m. The altitude ranged (approximately) from 0.5 m to 1.5 m. The planned underwater mission at the test site is visible in Fig.5.14. The navigation path of the AUKF solution

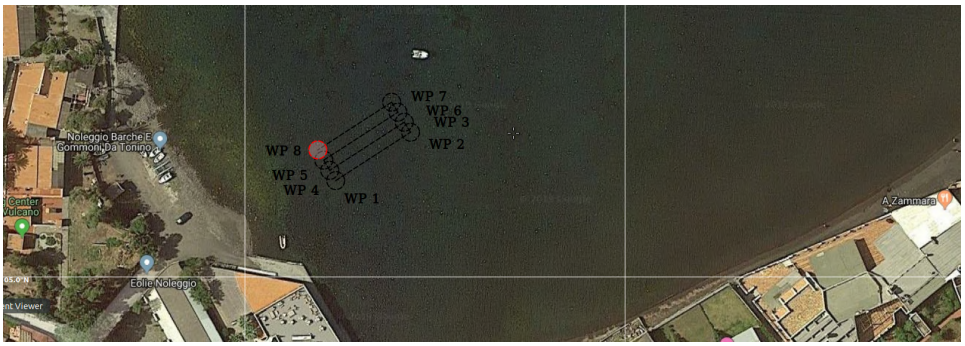

Figure 5.14: Google Earth image of the Negro Bay, Vulcano Island (Italy) overlaid with the planned autonomous underwater mission. The waypoints are indicated with WP.

(compared with a DVL-based DR high-resolution position data reference) is in Fig.5.12, whereas a quantitative comparison, by means of the metrics defined in Eq.5.1, is depicted in Fig.5.16. The parameters involved for the AUKF are summarized in Tab.5.7.

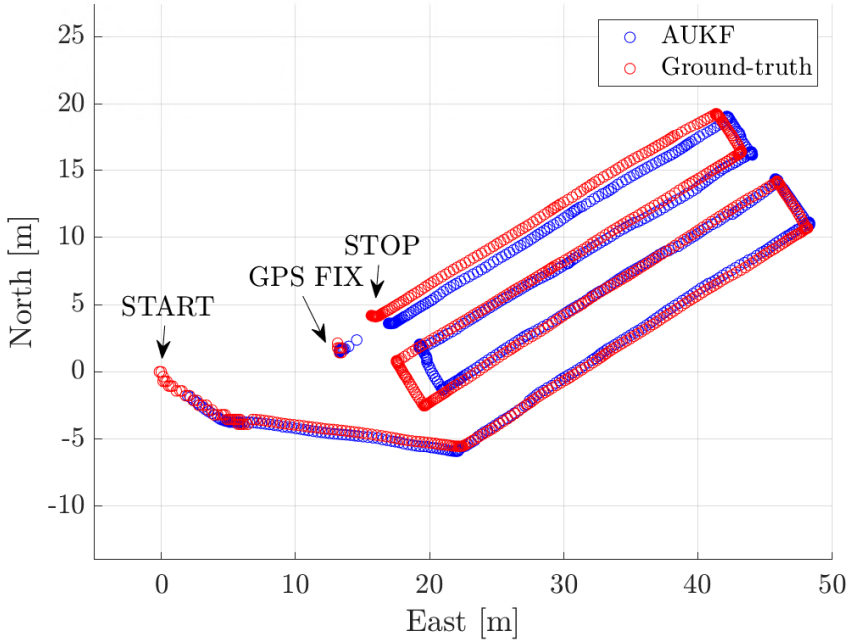

Figure 5.15: Navigation results for the AUKF estimator. The high-resolution position data path is in red and the proposed solution in blue. "START" and "STOP" indicate the first and last (underwater) point of the high-resolution position data path, respectively, whereas "GPS FIX" stands for the position obtained after resurfacing. The resurfacing error is around 4 m. For the sake of brevity high-resolution position data is indicated with "Ground-truth".

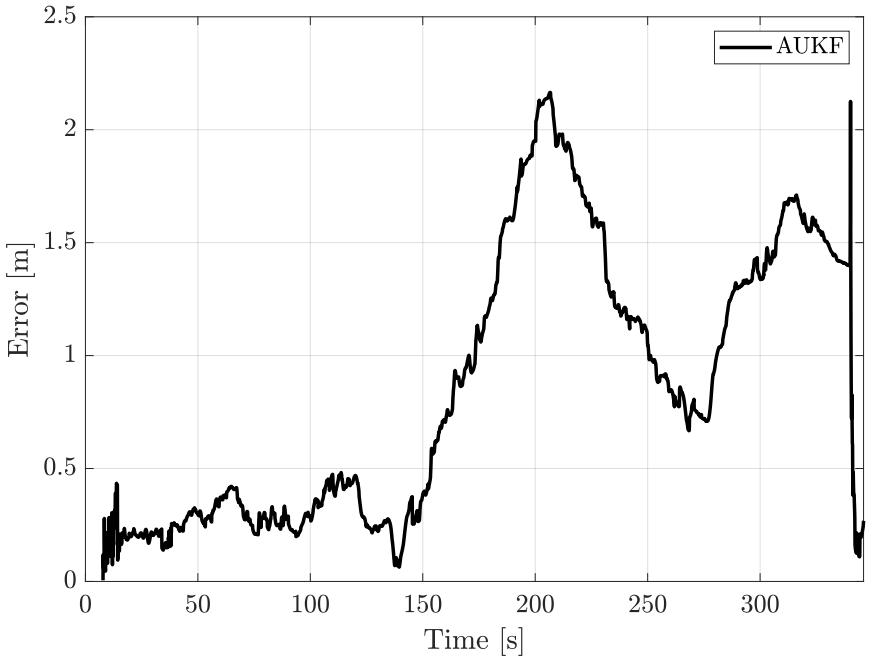

Figure 5.16: Error for the AUKF solution as defined in Eq.5.1. The resurfacing, which is around 340 s, a difference between the high-resolution position data and the AUKF solution is present. The former is the raw GPS signal, whereas the latter is the positional output of the AUKF proposal, where the dynamic model and the GPS signal are fused.

AUKF main parameters	
Reliability level fault detection ϱ	0.75
q [m^2/s^4]	0.001
q_z [m^2/s^4]	0.1
N_{R_w}	15
R_1	$\begin{bmatrix} 0.1 & 0 & 0 & 0 & 0 \\ 0 & 0.1 & 0 & 0 & 0 \\ 0 & 0 & 0.01 & 0 & 0 \\ 0 & 0 & 0 & 0.00001 & 0 \\ 0 & 0 & 0 & 0 & 0.00001 \end{bmatrix}$
Acceptance threshold c_r	0.60
LP filter cut-off frequency (D_0) [pixel]	60
LP filter order l	3
$\frac{R_{\rightarrow MAX}}{h}$ [pixel/m]	470.6 (range at 10 m)

Table 5.7: Main parameters involved in the autonomous underwater mission at the Negro Bay, Vulcano Island (Italy).

The results presented in Section 5.2.1 and Section 5.2.2 are promising and are shown to be comparable with those obtained with a DVL-based navigation system. As already discussed in Section 1.4, using an FLS to aid navigation could potentially outline advantages in terms of redundancy and compactness. The author wishes to point out that even if the tests were conducted without exploiting any DVL measurement, cooperation with the DVL is possible. This way, more linear speed measurements could be obtained, and a better performance is likely to be achieved. More online underwater tests will be implemented shortly.

Chapter 6

Conclusion

This work summarizes the results carried out at the MDM Lab of the UNIFI DIEF during the years 2016-2019, *i.e.* during the Ph.D. period, for what concerns the research activity on underwater robotics. The main goal was to enhance and improve the UNIFI DIEF previously-developed navigation algorithms as well as propose and implement new novel solutions. More in detail, including payload sensors, in particular one FLS, as aid for navigation has been arisen as the major development guideline.
Starting from the analysis of the state-of-the-art of such device, a first attempt to deal with it was to produce consistent acoustic mosaics of the seabed that did not exclusively rely on an FLS as "a mere equipment to obtain acoustic images". Indeed the developed solution aimed at merging both the information provided by the standard onboard navigation algorithms and the information retrieved by the images themselves. This task was satisfyingly addressed, and an online framework for underwater mosaicing tailored to the characteristics of FLS imagery was proposed, see Appendix B and the author's references therein. Afterward, how to suitably fuse the research background of the UNIFI DIEF in underwater navigation with the usage of an FLS was pursued. In this sense, the outcomes and the expertise in acoustic underwater mosaicing, where the FLS was not merely employed as a "passive" element in the framework, were exploited. Eventually, estimating the translation motions and thus linear velocities, by using the raw acoustic images delivered by such device, resulted as the optimal adopted solution. Subsequently, the established and reliable navigation structure developed over the past years at the UNIFI DIEF was used as reference to be

enhanced both in order to deal with information from an FLS and in terms of dynamic description. In particular, on the one hand, the dynamic model of the vehicle was further investigated (damping modeling and estimation, propulsion modeling), whereas, on the other hand, an AUKF estimator was proposed. The main goal was to better the performance of a simple UKF-based solution and to adapt the navigation algorithm to the usage of an FLS.

A preliminary laboratory research and testing phase were performed, where different data sets were tested and validated (see Section 5.1 and the author's reference therein). Then, an experimental activity at sea (two underwater missions, at La Spezia (Italy) and at Negro Bay, Vulcano Island (Italy), were planned) allowed verifying the goodness of the proposed strategy during real underwater missions and identifying the pros and cons, see Section 5.2. As far as a quantitative analysis is concerned, the presented AUKF solution is shown to achieve performance, in terms of navigation accuracy, comparable with those obtained with a high-resolution underwater architecture constituted of, among other devices, a DVL. The position error (instant-by-instant) maintained below 2.5 m for the extent of the mission and, in addition to this, the resurfacing error (with respect GPS fixes) was always below 5% of the total length of the path. During the experimental campaign FeelHippo AUV was the only vehicle involved; nevertheless, since the proposed solution is not tailored to a particular vehicle, its outcomes can be deemed as general, and future developments will involve the testing of the navigation strategy on the other members of the UNIFI DIEF MDM Lab fleet (see Chapter 2). Furthermore, it is worth noting that the complete navigation strategy was tested and evaluated in the worst-case scenario, without relying on DVL measurements during real autonomous underwater missions. The achieved significant results, presented in Chapter 5, highlight the goodness of the proposed strategy, which may shed light on safe autonomous navigation with FLS as a prominent resource.

Nonetheless, progress still needs to be made: reliable rotation estimation via FLS images is a subject worth to be further investigated, a more elaborate dynamics description of the AUV introduced in Section 4.3.1 could better the filter accuracy and, in addition, a more intense research on the adaptive filtering might improve the overall behavior and the capability of adapting to mutable scenarios. Lastly, a SLAM framework tailored to acoustic FLS

images would push forward the performance of the navigation filter, paving the way to a drift-free solution. In this sense, the intrinsic characteristic of FLS images (low resolution, FLS response change when the same object is insonified from different viewpoints) poses relevant issues to face, whose resolution could represent a coherent continuation of the research activity carried out so far.

Appendix A

Sensor modeling

A brief treatment on the mathematical modeling of sensors and devices that are usually used in marine robotics for autonomous navigation is presented and, in addition to this, as described in Section 2, they are mounted by UNIFI DIEF on its vehicles. More information can be found in [Fanelli, 2019].

Global Positioning System

Although the GPS signal cannot be used in underwater scenarios [Barclay, 2003], it is usually mounted on almost all AUVs for initialization and/or periodic position resets. A GPS measurement can be modeled as in Eq.A.1.

$$^{N}\boldsymbol{P}_{GPS} = \boldsymbol{f}_{GPS}(\boldsymbol{P}_{GPS} + \boldsymbol{\epsilon}_P, \boldsymbol{O}) = ^{N} \boldsymbol{\eta_1} + \tilde{\boldsymbol{\epsilon}}_P, \tag{A.1}$$

where $^{N}\boldsymbol{P}_{GPS}$ is the position in the NED frame obtained after the use of $\boldsymbol{f}_{GPS}$, the function to convert geodetic coordinates to local NED ones, $\boldsymbol{P}_{GPS}$ is the position obtained with the GPS, $\boldsymbol{\epsilon}_P$ is the error introduced to model accuracy, which is mapped into $\tilde{\boldsymbol{\epsilon}}_P$ after the NED conversion, and O are the geodetic coordinates of the point assumed as origin of the NED frame (usually the temporally first GPS fix).

Depth Sensor

Depth sensors are simple, light-weight and cheap devices that, by means of pressure measurements, can estimate depth. According to Eq.A.2, a

stochastic representation of a pressure measurement can be obtained:

$$p_{DS} = p + b_p + \epsilon_p, \tag{A.2}$$

where p_{DS} is the actual measured pressure, which can be modeled as the sum of the real pressure p, the sensor bias b_p, and the measurement noise ϵ_p. By applying a simple hydrostatic relation, the depth measurement becomes:

$$p_{DS} - p_0 = \rho g^N d_{DS}, \tag{A.3}$$

where being p_0 is the pressure measured during the initialization phase, ρ is the water density, g is the gravitational acceleration and d_{DS} is the measured depth, which can be thus modeled as:

$$^N d_{DS} = z + \epsilon d, \tag{A.4}$$

being z the real depth and ϵd is the noise. It is worth noting that the above-mentioned discussion permits to obtain a relative depth with respect to an initialization measurement (usually performed when the vehicle is on sea surface). As a consequence, the bias term b_p cancels out.

Doppler Velocity Log

A DVL is a device able to measure, by exploiting the Doppler effect, a 3D linear velocity of the vehicle either with respect the sea bottom (*bottom lock*) or the water column (*surface lock*). In the development of this thesis, it is assumed that the device works in bottom lock modality. As a consequence, the following mathematical model has been used:

$$^b\boldsymbol{v}_{DVL} =^b \boldsymbol{\nu}_1 + \boldsymbol{b}_v + \boldsymbol{\epsilon}_v, \tag{A.5}$$

where the measured velocity $^b\boldsymbol{v}_{DVL}$ is assumed to be the sum of a true value $^b\boldsymbol{\nu}_1$, the bias $\boldsymbol{b}_v$, and the measurement noise $\boldsymbol{\epsilon}_v$.

Inertial Measurement Unit

Usually, the term IMU stands for an instrument with accelerometers and gyroscopes. Nonetheless, sometimes IMUs also presents a triaxial magne-

tometer. For the sake of clarity, in the rest of the thesis, the term IMU will be used to denote an instrument that encompasses accelerometers and gyroscopes. However, the vehicles of the UNIFI DIEF MDM Lab fleet are equipped with triaxial accelerometers, gyroscopes, and magnetometers within the same device. For what concerns the accelerometers, where $\boldsymbol{\epsilon}_a$ represents measurement noise and $\boldsymbol{b}_a$ is the accelerometer bias (assuming the accelerometer properly calibrated this term is usually neglected).

$$ {}^{b}\mathbf{a}_{IMU} = \left({}^{N}R_{B}^{N}\right)^{T}\left(\ddot{\boldsymbol{\eta}}_1 - \mathbf{g}\right) + \boldsymbol{b}_a + \boldsymbol{\epsilon}_a, \tag{A.6} $$

For what concerns the gyroscopes,

$$ {}^{b}\boldsymbol{\omega}_{IMU} = {}^{b}\boldsymbol{\nu}_2 + \boldsymbol{b}_g + \boldsymbol{\epsilon}_g, \tag{A.7} $$

where the sum of true angular velocity ${}^{b}\boldsymbol{\nu}_2$, the bias $\boldsymbol{b}_g$, and the noise $\boldsymbol{\epsilon}_g$ produces the sensed quantity ${}^{b}\boldsymbol{\omega}_{IMU}$.

Magnetometer

A widely employed model is:

$$ {}^{b}\boldsymbol{m} = W({}^{N}R_{b}^{N})^{T}({}^{N}\boldsymbol{H}) + \boldsymbol{H}_m + \boldsymbol{\epsilon}_m, \tag{A.8} $$

where ${}^{N}\boldsymbol{H}$ is the Earth's magnetic field expressed in the fixed frame, W and $\boldsymbol{H}_m$ are the disturbances and $\boldsymbol{\epsilon}_m$ is the measurement noise. Since this treatment goes beyond the scope of this work, the interested reader can refer to [Vasconcelos et al., 2011], [Fanelli, 2019], and the references therein.

Fiber Optic Gyroscope

A FOG is a device able to measure, by exploiting the Sagnac effect, the angular rate. For what concerns a single-axis device, the following model can be adopted:

$$ {}^{m}\omega_{FOG} = \omega_{FOG} + b_e + b_f + \epsilon_f, \tag{A.9} $$

where ${}^{m}\omega_{FOG}$ is the measured quantity, ω_{FOG} is the true value, b_e is the component of Earth's rotation sensed by the gyro, b_f is an additional bias term, and ϵ_f is the measurement noise.

Forward Looking Sonar

It is well known that a 2D FLS consists of a series of azimuth α and ranges $R_{\rightarrow}$ measurements with a scalar value that represents the intensity of the returned echo. Considering a duple of azimuth and range α and $R_{\rightarrow}$ and the imaging geometry model presented in Section 3.3, the noisy description in Eq.A.10 can be obtained:

$$\begin{bmatrix} {}^{m}R_{\rightarrow} \\ {}^{m}\alpha \end{bmatrix} = \begin{bmatrix} R_{\rightarrow} \\ \alpha \end{bmatrix} + \boldsymbol{b}_s + \boldsymbol{\epsilon}_s = \begin{bmatrix} \sqrt{X^2+Y^2+Z^2} \\ \arctan\left(\frac{Y}{X}\right) \end{bmatrix} + \boldsymbol{b}_{s1} + \boldsymbol{\epsilon}_{s1}, \quad \text{(A.10)}$$

where ${}^{m}R_{\rightarrow}$ is the measured range, $R_{\rightarrow}$ its true value, ${}^{m}\alpha$ is the measured azimuth angle, α its true value, $\boldsymbol{b}_{s1}$ and $\boldsymbol{\epsilon}_{s1}$ are respectively an additional bias term and the measurement noise for both the range and the azimuth angle. A similar approach can be found in [Yang and Huang, 2017].
On the other hand, in this work, the FLS is used to obtain linear speed estimations or, generally speaking, translational motions after applying the solution described in Section 4.1. As a consequence, from Eq.A.10, it is not easy to predict the final noise statistics. Indeed, the estimation will possess different spectral properties than those of the noise affecting range and elevation angle. Nevertheless, a model with a true value that is the sum of a measured one, a bias term and a noise can be adopted:

$${}^{b}\boldsymbol{v}_{FLS} = {}^{b}\boldsymbol{\nu}_1 + \tilde{\boldsymbol{b}}_{s1} + \tilde{\boldsymbol{\epsilon}}_{s1}, \quad \text{(A.11)}$$

where the measured velocity ${}^{b}\boldsymbol{v}_{FLS}$ is assumed to be the sum of a true value ${}^{b}\boldsymbol{\nu}_1$, the bias $\tilde{\boldsymbol{b}}_{s1}$, and the measurement noise $\tilde{\boldsymbol{\epsilon}}_{s1}$.

Some authors, such as [Pfingsthorn et al., 2010], and [Hurtós et al., 2015], proposed heuristic methods where the underlying idea is that the surrounding of the main peak of the matrix $c(x, y)$ can represent the accuracy of the phase correlation method. Nevertheless, the adaptive filtering technique proposed in Section 4.3 can adapt the measurement noise on its own.

Appendix B

Online acoustic underwater mosaicing

Mapping is a common problem in the underwater environment, and studies on this topic, which is fundamental for underwater vehicles to enhance the knowledge of the environment around them, have been actively carried out by several researchers. An online acoustic underwater mosaicing structure that suites the peculiarities of FLS images was satisfyingly addressed during the first part of the Ph.D. period [Franchi et al., 2018].
The technique is composed of three steps that will be explained as follows:

- registration;
- global alignment;
- mosaic blending.

Registration

As explained in Section 1.3, registration is the process through which a pair of overlapped images collected from different viewpoints are associated into one coordinate system. The proposed approach resorts to two solutions that run in parallel: the first one involves the use of the raw FLS images, whereas the second one exploits information obtained from the navigation filter, which can employ (or not) a FLS. For what concerns the former, the algorithm is thoroughly explained in Section 3.3 and Section 4.1. Here, linear translation between two subsequent FLS images is already sufficient,

and linear speed estimation is not computed. In conclusion, given a GPS initialization (which is necessary to geo-localize the underwater mosaic), FLS images can be registered by using the following logic, henceforth called "FLS images win". If, basing on phase correlation goodness index c_r (defined in Section 4.1.2), the phase correlation process is deemed as sufficiently good, its output is employed in favor of information from the navigation filter. By

Algorithm "FLS images win"

input : c_r
output: Condition Check
if *($c_r > \overline{c_r}$)* **then**
| *registration exploiting acoustic images*
end
registration exploiting navigation filter

applying this approach, the underwater mosaic works continuously, and it is thus not limited by the particular sea bottom scenario, which could not carry any informative content.

Global alignment

Global alignment is the process through which all the collected images are associated into a common reference frame. The currently implemented approach, which can be deemed as the most straight forward one, is to concatenate the successive transformations to the final mosaic. Although the authors are aware that this method is prone to cumulative errors over time, the proposed solution appears a good trade-off, being less computationally burden with respect to more sophisticated techniques such as is [Kim et al., 2006] and [Hurtós et al., 2015]. This is especially sensed in the case of AUVs, where different and complex processes need to be carried out onboard in real-time.

Mosaic blending

The final goal is to improve the appearance of the final artifact. Before the actual blending takes place, the single acoustic images need to be improved in terms of quality. To do so, three steps are considered:

1. the first one involves the use of all the available image data set (within a preset window) with the aim of estimating, by averaging all the frames, the underlying acoustic pattern (see Fig. B.1). The systematic error in the insonification pattern, which is likely to affect the acoustic images [Negahdaripour et al., 2005] and [Hurtós et al., 2015], is thus detected and removed. Hence, a moving real-time updated window with a fixed size is used, where the oldest acoustic images are gradually removed.

$$i_{post}(x, y) = i_{pre}(x, y) - i_{mean}(x, y), \tag{B.1}$$

where $i_{pre}(x, y)$ and $i_{post}(x, y)$ are the images before and after mean subtraction, respectively, and $i_{mean}(x, y)$ is the underlying acoustic pattern. Because of the mean subtraction operation makes the image darker, an adaptive law that tries to maintain the overall illumination is introduced, Eq.B.2, and Eq.B.3.

$$i_{post}(x, y) = i_{pre}(x, y) - i_{mean}(x, y) + i_{adding}(x, y), \tag{B.2}$$

with

$$i_{adding}(x, y) = k_{mean}\overline{i_{mean}(x, y)}, \tag{B.3}$$

where $i_{adding}(x, y)$ is the image obtained from the adaptive law and k_{mean} is a constant $\in (0, 1]$. If $k_{mean} = 1$ the average brightness is preserved, whereas if $k_{mean} < 1$ this is no more true, but image saturation can be prevented.

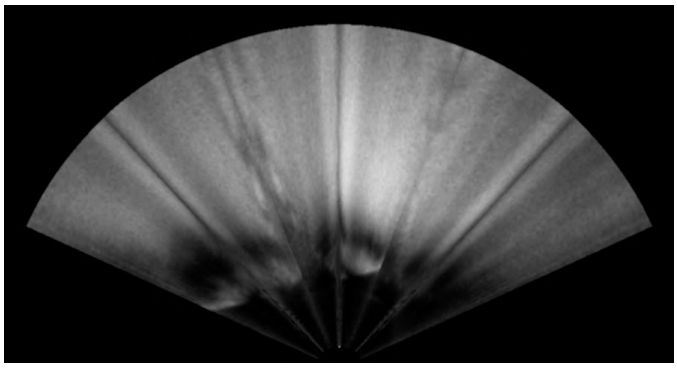

Figure B.1: Typical insonification pattern in FLS images.

2. The second one concerns the use of the Contrast Limited Adaptive

Histogram Equalization (CLAHE) technique with the aim of modifying the intensity histograms of the acoustic frames [Pizer et al., 1987]. As already pointed out by [Hurtós et al., 2013a], FLS imagery usually presents inhomogeneous illumination that might depend, for example, upon terrain shape and illumination direction. Therefore, a more uniform image distribution can be achieved lessening the intensity offsets.

3. The last one involves the removal of areas that show poor information. In particular, homogeneous image parts with low response, so with low local variance and low local mean respectively, are blinded. In addition, the closest area to the FLS center, which is likely to present noise or poor information, is blinded as well.

The actual mosaic blending is performed by summing the images on an image with greater depth, henceforth called "tank", and by creating a map of the overlapped areas, henceforth called "map". In other words, a function that manages how many times a given pixel is occupied is defined. By simply dividing pixel-by-pixel the "tank" with the "map", the final artifact takes place. Other blending techniques are proposed by [Ferreira et al., 2015] and [Hurtós et al., 2013a].
Some of the results obtained during the robotics competition ERL SAUC-E 2018, held in La Spezia (Italy) at the NATO STO CMRE in July 2018, are presented. In particular, a 2D geo-localized underwater reconstruction of the competition arena is reported in Fig. B.2. The mosaic is composed of around 700 acoustic images combined together, and the registration process was performed exploiting both navigation information from a DVL-based DR strategy and from raw FLS images with the already mentioned logic "FLS images win". In particular, 356 registrations using FLS images, whereas the others using the navigation filter. Looking at Fig. B.2, two underwater structures composed of assembled pipes can be noted in the middle. In addition, the good matching between the wharf contour obtained from Google Earth and the acoustic reconstruction can be observed as well.

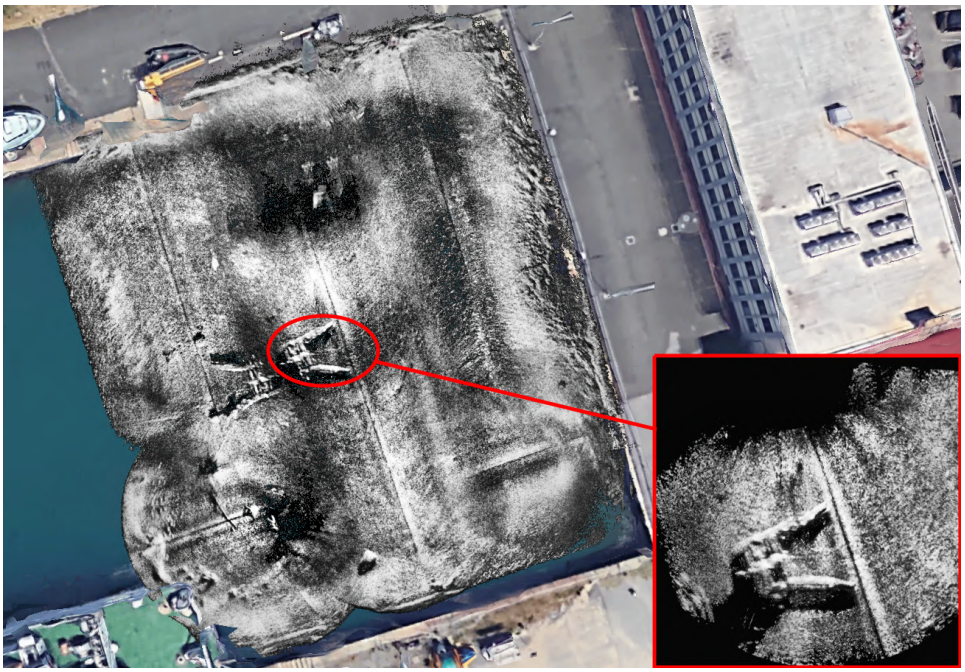

Figure B.2: Google Earth image of the competition arena at the NATO STO CMRE (La Spezia, Italy) overlaid with the underwater acoustic mosaic. The covered area is about 2000 m^2. In the bottom-right corner, a detail of one of the two underwater structures is presented.

Appendix C

Observability analysis

The method described in Section 4.1 is not able to obtain linear speed measurement along the z-axis of the body-fixed frame, thus, in order to justify the AUKF or a generic UKF estimation strategy in the absence of a DVL device, the observability of the system needs to be proven. While in [Hermann and Krener, 1977] nonlinear observability for continuous-time systems is studied, in the discrete-time context contributions can be found in [Nijmeijer, 1982] and [Albertini and D'Alessandro, 2002]. In particular, the latter is used as a reference for the following discussion.
First of all, for the sake of clarity, the basic (classical) definitions of *indistinguishability*, *observability*, *local weak observability* and *local strong observability* are provided. Afterward, sufficient conditions to guarantee both the local strong and weak observability of the system are furnished. Lastly, the dynamical system described in Section 4.3 in the absence of the DVL contribution is proven to be locally strongly observable. For the interested reader, more information can be found in [Albertini and D'Alessandro, 2002] and the references therein. In the rest of this section, the observability of nonlinear discrete-time models of the form

$$\begin{cases} \boldsymbol{x}_k = \boldsymbol{f}\left(\boldsymbol{x}_{k-1}, \boldsymbol{u}_{k-1}\right) \\ \boldsymbol{y}_k = \boldsymbol{h}\left(\boldsymbol{x}_k\right) \end{cases} \tag{C.1}$$

is presented. Where

$$\boldsymbol{x} \in N \subset \mathbb{R}^n, \boldsymbol{y} \in P \subset \mathbb{R}^p, \boldsymbol{u} \in M \subset \mathbb{R}^m, \boldsymbol{f} : N \times P \to N, \boldsymbol{h} : N \to P, \tag{C.2}$$

where $\boldsymbol{f}(\bullet)$ and $\boldsymbol{h}(\bullet)$ are of class C^∞ and it is assumed that N and P are connected, second countable, Hausdorff, differentiable manifolds and M is an open interval of $\mathbb{R}$.

Definition C.0.1. Two states $\tilde{\boldsymbol{x}}$ and $\bar{\boldsymbol{x}}$ are said *indistinguishable*, with symbol $\tilde{\boldsymbol{x}}\boldsymbol{I}\bar{\boldsymbol{x}}$, for each $j > 0$ and for each sequence of controls $\{u_1, \ldots, u_j\} \in M^j$ if:

$$\boldsymbol{h}\left(\boldsymbol{f}_{u_j} \circ \cdots \circ \boldsymbol{f}_{u_1}(\tilde{\boldsymbol{x}})\right) = \boldsymbol{h}\left(\boldsymbol{f}_{u_j} \circ \cdots \circ \boldsymbol{f}_{u_1}(\bar{\boldsymbol{x}})\right), \tag{C.3}$$

where $\circ$ stands for the composition of functions.

Definition C.0.2. A state $\tilde{\boldsymbol{x}} \in N \subset \mathbb{R}^n$ is said to be *observable* if $\tilde{\boldsymbol{x}}\boldsymbol{I}\boldsymbol{x} \implies \tilde{\boldsymbol{x}} = \boldsymbol{x}$.

Definition C.0.3. A state $\tilde{\boldsymbol{x}} \in N \subset \mathbb{R}^n$ is said to be *locally weakly observable* if there exists a neighborhood of $\tilde{\boldsymbol{x}}$ such that, for each $\boldsymbol{x}$ in the neighborhood, $\tilde{\boldsymbol{x}}\boldsymbol{I}\boldsymbol{x} \implies \tilde{\boldsymbol{x}} = \boldsymbol{x}$.

Definition C.0.4. A state $\tilde{\boldsymbol{x}} \in N \subset \mathbb{R}^n$ is said to be *locally strongly observable* if there exists a neighborhood of $\tilde{\boldsymbol{x}}$ such that, for each $\bar{\boldsymbol{x}}$, $\hat{\boldsymbol{x}}$ in the neighborhood, $\bar{\boldsymbol{x}}\boldsymbol{I}\hat{\boldsymbol{x}} \implies \bar{\boldsymbol{x}} = \hat{\boldsymbol{x}}$.

Definition C.0.5. A system is said to be locally weakly or locally strongly observable if this property is true for each state $\boldsymbol{x} \in N$.

It can be shown ([Albertini and D'Alessandro, 2002]) that for a system of the type C.1 with properties in C.2, fixed a state $\tilde{\boldsymbol{x}} \in N$ if $\dim d\mathcal{O}(\tilde{\boldsymbol{x}}) = n$, then $\tilde{\boldsymbol{x}}$ is a locally strongly observable state for system C.1, where $\dim d\mathcal{O}$ is the dimension of the codistribution $d\mathcal{O}$, and where $d\mathcal{O}$ is the codistribution spanned by all the differentials of these functions.
In the absence of DVL measurement, the system described in Section 4.3 becomes:

$$\boldsymbol{x} = [\ {}^N\boldsymbol{\eta}_1^T \quad {}^b\boldsymbol{\nu}_1^T\ ]^T, \boldsymbol{x} \in \mathbb{R}^6, \tag{C.4}$$

$$\begin{bmatrix} {}^N\boldsymbol{\eta}_1 \\ {}^b\boldsymbol{\nu}_1 \end{bmatrix}_k = \begin{bmatrix} {}^N\boldsymbol{\eta}_1 \\ {}^b\boldsymbol{\nu}_1 \end{bmatrix}_{k-1} + \Delta T \begin{bmatrix} {}^N R_B^N\left((\boldsymbol{\eta}_2)_{k-1}\right)\left({}^b\boldsymbol{\nu}_1\right)_{k-1} \\ \frac{\tau_{1,x}(\boldsymbol{\nu}_{k-1}, \mathbf{u}_{k-1})}{m} - \frac{(\delta_x)_{k-1}\nu_{1x}^2 \operatorname{sgn}(\nu_{1x})}{m} \\ 0 \\ 0 \end{bmatrix}, \tag{C.5}$$

$$\boldsymbol{y} = \begin{bmatrix} {}^{N}\boldsymbol{P}_{GPS}^{T} & d_{DS}^{N} & {}^{b}\boldsymbol{v}_{FLS}^{T} \end{bmatrix}^{T}, \boldsymbol{y} \in \mathbb{R}^{5} \tag{C.6}$$

In the rest the following assumption will be made:

Assumption 9. *N and P are connected, second countable, Hausdorff, differentiable manifolds and M is an open interval of $\mathbb{R}$. This hypothesis holds since the state of the system is indeed $\mathbb{R} \times \mathbb{R} \times \mathbb{R}^{+} \times \mathbb{R} \times \mathbb{R} \times \mathbb{R}$, whereas the output is $\mathbb{R} \times \mathbb{R} \times \mathbb{R}^{+} \times \mathbb{R} \times \mathbb{R}$.*

Assumption 10. *The propulsion model in Eq.4.13 and Eq.4.14 is supposed not to depend upon $\boldsymbol{\nu}$. Therefore, the influence of the vehicle motion to the actual exerted thrust is neglected.*

$d\mathcal{O}$, defined as in C.7, can be limited (as it will be shown in the following) to $d\mathcal{O}1$ and $d\mathcal{O}2$.

$$\begin{aligned} &\mathcal{O}_1 = \{\boldsymbol{h}(\bullet)\} \\ &\mathcal{O}_k = \left\{ \boldsymbol{h}\left(\boldsymbol{f}_{u_j} \circ \cdots \circ \boldsymbol{f}_{u_1}(\bullet) \right) | \forall i = 1, \cdots, j, u_i \in M, \text{ and } 1 \leq j \leq k-1 \right\} . \\ &\mathcal{O} = \cup_{k \geq 1} \mathcal{O}_k \end{aligned} \tag{C.7}$$

$$d\mathcal{O}_1 = \begin{bmatrix} 1 & 0 & 0 & 0 & 0 & 0 \\ 0 & 1 & 0 & 0 & 0 & 0 \\ 0 & 0 & 1 & 0 & 0 & 0 \\ 0 & 0 & 0 & 1 & 0 & 0 \\ 0 & 0 & 0 & 0 & 1 & 0 \end{bmatrix}, \tag{C.8}$$

$$d\mathcal{O}_2 = \begin{bmatrix} 1 & 0 & 0 & c(\psi)c(\theta) & c(\psi)s(\theta)s(\phi) - s(\psi)c(\phi) & c(\psi)c(\theta)c(\phi) + s(\psi)s(\phi) \\ 0 & 1 & 0 & s(\psi)c(\theta) & s(\psi)s(\theta)s(\phi) + c(\psi)c(\phi) & s(\psi)s(\theta)c(\phi) - c(\psi)s(\phi) \\ 0 & 0 & 1 & -s(\theta) & c(\theta)s(\phi) & c(\theta)c(\phi) \\ 0 & 0 & 0 & 1 - 2\frac{(\delta_x)_{k-1}\nu_{1x}\,\mathrm{sgn}(\nu_{1x})}{m} & 0 & 0 \\ 0 & 0 & 0 & 0 & 1 & 0 \end{bmatrix}, \tag{C.9}$$

By observing Eq.C.8 and Eq.C.9, it can be easily noted that the matrix $[d\mathcal{O}_1, d\mathcal{O}_2]$ presents six linearly independent rows. Indeed the first three rows of Eq.C.9 include the elements of the rotation matrix ${}^{N}R_{B}^{N}$ whose rows cannot be (by rotation matrix definition) null. In conclusion, $\dim d\mathcal{O} = 6$ $\forall \boldsymbol{x} \in \mathbb{R}^{6}$ and, in light of Assumption 9, Assumption 10, Definition C.0.5, and

the work of [Albertini and D'Alessandro, 2002], the system is locally strongly observable (and thus locally weak observable). To clarify, let us assume that roll (ϕ) and pitch (θ) in the rotation matrix ${}^{N}R_{B}^{N}$ are approximately zero, which is reasonable for the most AUV, so $cos(\bullet) \approx 1$ and $sin(\bullet) \approx 0$.

$$[d\mathcal{O}_1, d\mathcal{O}_2] = \begin{bmatrix} 1 & 0 & 0 & 0 & 0 & 0 \\ 0 & 1 & 0 & 0 & 0 & 0 \\ 0 & 0 & 1 & 0 & 0 & 0 \\ 0 & 0 & 0 & 1 & 0 & 0 \\ 0 & 0 & 0 & 0 & 1 & 0 \\ 1 & 0 & 0 & c(\psi) & -s(\psi) & 0 \\ 0 & 1 & 0 & s(\psi) & c(\psi) & 0 \\ 0 & 0 & 1 & 0 & 0 & 1 \\ 0 & 0 & 0 & 1 - 2\frac{(\delta_x)_{k-1}\nu_{1x}\,\mathrm{sgn}(\nu_{1x})}{m} & 0 & 0 \\ 0 & 0 & 0 & 0 & 1 & 0 \end{bmatrix}, \qquad \text{(C.10)}$$

It is easy to understand that the matrix in Eq.C.10 possesses six linearly independent rows (first, second, third, fourth, fifth and eighth).

References

[Åkesson et al., 2008] Åkesson, B. M., Jørgensen, J. B., Poulsen, N. K., and Jørgensen, S. B. (2008). A generalized autocovariance least-squares method for Kalman filter tuning. *Journal of Process Control*, 18(7-8):769–779.

[Alba et al., 2015] Alba, A., Vigueras-Gomez, J. F., Arce-Santana, E. R., and Aguilar-Ponce, R. M. (2015). Phase correlation with sub-pixel accuracy: A comparative study in 1D and 2D. *Computer Vision and Image Understanding*, 137:76–87.

[Albertini and D'Alessandro, 2002] Albertini, F. and D'Alessandro, D. (2002). Observability and forward–backward observability of discrete-time nonlinear systems. *Mathematics of Control, Signals and Systems*, 15(4):275–290.

[Allotta et al., 2014] Allotta, B., Bartolini, F., Conti, R., Costanzi, R., Gelli, J., Monni, N., Natalini, M., Pugi, L., and Ridolfi, A. (2014). MARTA: an AUV for underwater cultural heritage. In *Proceeding of the UA2014 International Conference and Exhibition, Island of Rhodes (GK)*.

[Allotta et al., 2016a] Allotta, B., Caiti, A., Chisci, L., Costanzi, R., Di Corato, F., Fantacci, C., Fenucci, D., Meli, E., and Ridolfi, A. (2016a). An Unscented Kalman Filter based navigation algorithm for Autonomous Underwater Vehicles. *Mechatronics*, 39:185–195.

[Allotta et al., 2016b] Allotta, B., Caiti, A., Costanzi, R., Fanelli, F., Fenucci, D., Meli, E., and Ridolfi, A. (2016b). A new auv navigation system exploiting Unscented Kalman Filter. *Ocean Engineering*, 113:121–132.

[Allotta et al., 2016c] Allotta, B., Caiti, A., Costanzi, R., Fanelli, F., Fenucci, D., Meli, E., and Ridolfi, A. (2016c). A new AUV navigation system exploiting Unscented Kalman Filter. *Ocean Engineering*, 113:121–132.

[Allotta et al., 2015a] Allotta, B., Chisci, L., Costanzi, R., Fanelli, F., Fantacci, C., Meli, E., Ridolfi, A., Caiti, A., Di Corato, F., and Fenucci, D. (2015a). A comparison between EKF-based and UKF-based navigation algorithms for AUVs localization. In *Proceedings of OCEANS'15 MTS/IEEE GENOVA, Genova (IT)*. IEEE.

[Allotta et al., 2017] Allotta, B., Costanzi, R., Fanelli, F., Monni, N., Paolucci, L., and Ridolfi, A. (2017). Sea currents estimation during AUV navigation using Unscented Kalman Filter. *IFAC-PapersOnLine*, 50(1):13668–13673.

[Allotta et al., 2015b] Allotta, B., Costanzi, R., Gelli, J., Pugi, L., and Ridolfi, A. (2015b). Design of a modular propulsion system for MARTA AUV. In *Proceedings of OCEANS'15 MTS/IEEE GENOVA, Genova (IT)*. IEEE.

[Allotta et al., 2018] Allotta, B., Costanzi, R., Pugi, L., and Ridolfi, A. (2018). Identification of the main hydrodynamic parameters of Typhoon AUV from a reduced experimental dataset. *Ocean Engineering*, 147:77–88.

[Allotta et al., 2013] Allotta, B., Pugi, L., Bartolini, F., Costanzi, R., Ridolfi, A., Monni, N., Gelli, J., Vettori, G., Gualdesi, L., and Natalini, M. (2013). The THESAURUS project, a long range AUV for extended exploration, surveilance and monitoring of archeological sites. In *V International Conference on Computational Methods in Marine Engineering ECCOMAS MARINE*.

[ARCHEOSUb, 2019] ARCHEOSUb (2019). Official website of the ARCHEOSUb project:. www.archeosub.eu. [Online; accessed July 2019].

[ARROWS, 2019] ARROWS (2019). Official website of the ARROWS project:. www.arrowsproject.eu. [Online; accessed July 2019].

[Averbuch et al., 2006] Averbuch, A., Coifman, R. R., Donoho, D. L., Elad, M., and Israeli, M. (2006). Fast and accurate polar Fourier transform. *Applied and Computational Harmonic Analysis*, 21(2):145–167.

[Aykin and Negahdaripour, 2012] Aykin, M. and Negahdaripour, S. (2012). On feature extraction and region matching for Forward Scan SONAR imaging. In *Proceedings of OCEANS'12 MTS/IEEE HAMPTON ROADS, Hampton Roads, VA (USA)*. IEEE.

[Aykin and Negahdaripour, 2013] Aykin, M. D. and Negahdaripour, S. (2013). On feature matching and image registration for two-dimensional Forward-Scan SONAR imaging. *Journal of Field Robotics*, 30(4):602–623.

[Bahr et al., 2009] Bahr, A., Leonard, J. J., and Fallon, M. F. (2009). Cooperative localization for Autonomous Underwater Vehicles. *The International Journal of Robotics Research*, 28(6):714–728.

[Bar-Shalom et al., 2004] Bar-Shalom, Y., Li, X. R., and Kirubarajan, T. (2004). *Estimation with applications to tracking and navigation: theory algorithms and software*. John Wiley & Sons.

[Barclay, 2003] Barclay, L. (2003). *Propagation of radiowaves*. IET.

[Bavdekar et al., 2011] Bavdekar, V. A., Deshpande, A. P., and Patwardhan, S. C. (2011). Identification of process and measurement noise covariance for state and parameter estimation using Extended Kalman Filter. *Journal of Process Control*, 21(4):585–601.

[Bélanger, 1974] Bélanger, P. R. (1974). Estimation of noise covariance matrices for a linear time-varying stochastic process. *Automatica*, 10(3):267–275.

[Bishop et al., 2010] Bishop, A. N., Fidan, B., Anderson, B. D., Doğançay, K., and Pathirana, P. N. (2010). Optimality analysis of sensor-target localization geometries. *Automatica*, 46(3):479–492.

[Bishop, 2006] Bishop, C. M. (2006). *Pattern Recognition and Machine Learning*. springer.

[Blue Robotics Inc., 2019] Blue Robotics Inc. (2019). Official website of Blue Robotics Inc.:. https://www.bluerobotics.com/. [Online; accessed April 2019].

[Bulow et al., 2009] Bulow, H., Birk, A., and Unnithan, V. (2009). Online generation of an underwater photo map with improved Fourier Mellin based registration. In *Proceedings of OCEANS 2009-EUROPE, Bremen (DE)*. IEEE.

[Bülow et al., 2010] Bülow, H., Pfingsthorn, M., and Birk, A. (2010). Using robust spectral registration for scan matching of SONAR range data. *IFAC Proceedings Volumes*, 43(16):611–616.

[Caccia et al., 2000] Caccia, M., Indiveri, G., and Veruggio, G. (2000). Modeling and identification of open-frame variable configuration Unmanned Underwater Vehicles. *IEEE Journal of Oceanic Engineering*, 25(2):227–240.

[Carlton, 2012] Carlton, J. (2012). *Marine propellers and propulsion*. Butterworth-Heinemann.

[Chen et al., 1994] Chen, Q.-s., Defrise, M., and Deconinck, F. (1994). Symmetric phase-only matched filtering of Fourier-Mellin transforms for image registration and recognition. *IEEE Transactions on Pattern Analysis & Machine Intelligence*, (12):1156–1168.

[Chou et al., 2017] Chou, Y.-C., Nakajima, M., Wang, C.-C., and Chen, H.-H. (2017). Identification of hydrodynamic coefficients for underwater vehicles using laser line scanning and genetic algorithm. In *Proceedings of OCEANS'17 MTS/IEEE ABERDEEN, Aberdeen (UK)*, pages 1–6. IEEE.

[Costanzi et al., 2019] Costanzi, R., Fanelli, F., Meli, E., Ridolfi, A., Caiti, A., and Allotta, B. (2019). UKF-based navigation system for AUVs: Online experimental validation. *IEEE Journal of Oceanic Engineering*, 44(3):633–641.

[Costanzi et al., 2016] Costanzi, R., Fanelli, F., Monni, N., Ridolfi, A., and Allotta, B. (2016). An attitude estimation algorithm for mobile robots under unknown magnetic disturbances. *IEEE/ASME Transactions on Mechatronics*, 21(4):1900–1911.

[Cristi et al., 1990] Cristi, R., Papoulias, F. A., and Healey, A. J. (1990). Adaptive sliding mode control of Autonomous Underwater Vehicles in the dive plane. *IEEE journal of Oceanic Engineering*, 15(3):152–160.

[Curcio et al., 2005] Curcio, J., Leonard, J., Vaganay, J., Patrikalakis, A., Bahr, A., Battle, D., Schmidt, H., and Grund, M. (2005). Experiments in Moving BaseLine navigation using autonomous surface craft. In *Proceedings of OCEANS'05 MTS/IEEE WASHINGTON, Washington, DC (USA)*, pages 730–735. IEEE.

[Daniamant A/S, 2019] Daniamant A/S (2019). Official website of Daniamant A/S:. https://www.daniamant.com. [Online; accessed April 2019].

[Davari and Gholami, 2016] Davari, N. and Gholami, A. (2016). An Asynchronous Adaptive Direct Kalman Filter algorithm to improve underwater navigation system performance. *IEEE Sensors Journal*, 17(4):1061–1068.

[De Castro and Morandi, 1987] De Castro, E. and Morandi, C. (1987). Registration of translated and rotated images using finite Fourier transforms. *IEEE Transactions on Pattern Analysis and Machine Intelligence*, PAMI-9(5):700–703.

[Dissanayake et al., 2000] Dissanayake, G., Durrant-Whyte, H., and Bailey, T. (2000). A computationally efficient solution to the simultaneous localisation and map building (SLAM) problem. In *2000 IEEE International Conference on Robotics and Automation (ICRA) (Cat. No. 00CH37065), San Francisco, CA (USA)*, volume 2, pages 1009–1014. IEEE.

[Dos Santos et al., 2017] Dos Santos, M., Ribeiro, P., Núñez, P., Drews-Jr, P., and Botelho, S. (2017). Object classification in semi structured enviroment using Forward-Looking SONAR. *Sensors*, 17(10):2235.

[Durrant-Whyte and Bailey, 2006] Durrant-Whyte, H. and Bailey, T. (2006). Simultaneous Localization And Mapping: part i. *IEEE Robotics & Automation Magazine*, 13(2):99–110.

[EchoPilot, 2019] EchoPilot (2019). Official website of EchoPilot:. https://echopilot.com. [Online; accessed April 2019].

[Eng et al., 2015] Eng, Y. H., Teo, K. M., Chitre, M., and Ng, K. M. (2015). Online system identification of an Autonomous Underwater Vehicle via in-field experiments. *IEEE Journal of Oceanic Engineering*, 41(1):5–17.

[EUMR, 2019] EUMR (2019). Official website of the EUMR project:. www.eumarinerobots.eu. [Online; accessed July 2019].

[Eustice et al., 2002] Eustice, R., Pizarro, O., Singh, H., and Howland, J. (2002). UWIT: Underwater image toolbox for optical image processing and mosaicking in MATLAB. In *Proceedings of the 2002 Interntional Symposium on Underwater Technology (Cat. No.02EX556), Tokyo (JP)*, pages 141–145. IEEE.

[Fallon et al., 2013] Fallon, M. F., Folkesson, J., McClelland, H., and Leonard, J. J. (2013). Relocating underwater features autonomously using SONAR-based SLAM. *IEEE Journal of Oceanic Engineering*, 38(3):500–513.

[Fanelli, 2019] Fanelli, F. (2019). *Development and Testing of Navigation Algorithms for Autonomous Underwater Vehicles*. Springer.

[Ferreira et al., 2014] Ferreira, F., Djapic, V., Micheli, M., and Caccia, M. (2014). Improving automatic target recognition with Forward Looking SONAR mosaics. *IFAC Proceedings Volumes*, 47(3):3382–3387.

[Ferreira et al., 2015] Ferreira, F., Djapic, V., Micheli, M., and Caccia, M. (2015). Forward Looking SONAR mosaicing for mine countermeasures. *Annual Reviews in Control*, 40:212–226.

[Ferri et al., 2015] Ferri, G., Ferreira, F., and Djapic, V. (2015). Boosting the talent of new generations of marine engineers through robotics competitions in realistic environments: The SAUC-E and euRathlon experience. In *Proceedings of OCEANS'15 MTS/IEEE GENOVA, Genova (IT)*. IEEE.

[Ferri et al., 2017] Ferri, G., Ferreira, F., and Djapic, V. (2017). Multi-domain robotics competitions: The CMRE experience from SAUC-E to the European Robotics League Emergency Robots. In *Proceedings of OCEANS'17 MTS/IEEE ABERDEEN, Aberdeen (UK)*. IEEE.

[Foroosh et al., 2002] Foroosh, H., Zerubia, J. B., and Berthod, M. (2002). Extension of phase correlation to subpixel registration. *IEEE Transactions on Image Processing*, 11(3):188–200.

[Fossen et al., 1994] Fossen, T. I. et al. (1994). *Guidance and control of ocean vehicles*. John Wiley & Sons.

[Franchi et al., 2019a] Franchi, M., Ridolfi, A., and Pagliai, M. (2019a). A Forward-Looking SONAR and dynamic model-based AUV navigation strategy: Preliminary validation with FeelHippo AUV. *Ocean Engineering*. (in press).

[Franchi et al., 2018] Franchi, M., Ridolfi, A., and Zacchini, L. (2018). A Forward-Looking SONAR-based system for underwater mosaicing and acoustic odometry. In *2018 IEEE/OES Autonomous Underwater Vehicle Workshop (AUV), Porto (P)*. IEEE.

[Franchi et al., 2019b] Franchi, M., Ridolfi, A., Zacchini, L., and Allotta, B. (2019b). Experimental evaluation of a Forward-Looking SONAR-based system for acoustic odometry. In *Proceedings of OCEANS'19 MTS/IEEE MARSEILLE, Marseille (FR)*. IEEE.

[Galceran et al., 2012] Galceran, E., Djapic, V., Carreras, M., and Williams, D. P. (2012). A real-time underwater object detection algorithm for Multi-Beam Forward-Looking SONAR. *IFAC Proceedings Volumes*, 45(5):306–311.

[Gao et al., 2015] Gao, S., Hu, G., and Zhong, Y. (2015). Windowing and random weighting-based Adaptive Unscented Kalman Filter. *International Journal of Adaptive Control and Signal Processing*, 29(2):201–223.

[Goheen and Jefferys, 1990] Goheen, K. and Jefferys, E. (1990). The application of alternative modelling techniques to ROV dynamics. In *Proceedings., IEEE International Conference on Robotics and Automation*, pages 1302–1309. IEEE.

[Groves, 2015] Groves, P. D. (2015). Principles of GNSS, inertial, and multisensor integrated navigation systems, [book review]. *IEEE Aerospace and Electronic Systems Magazine*, 30(2):26–27.

[Gu et al., 2015] Gu, J., Pyo, J., Joe, H., Kim, B., Kim, J., Cho, H., and Yu, S.-C. (2015). A method for automatic detection of underwater objects using Forward-Looking SONAR. In *Proceedings of OCEANS'05 MTS/IEEE WASHINGTON, Washington, DC (USA)*. IEEE.

[Hajiyev and Soken, 2014] Hajiyev, C. and Soken, H. E. (2014). Robust adaptive Unscented Kalman Filter for attitude estimation of pico satel-

lites. *International Journal of Adaptive Control and Signal Processing*, 28(2):107–120.

[Harris, 1978] Harris, F. J. (1978). On the use of windows for harmonic analysis with the discrete Fourier transform. *Proceedings of the IEEE*, 66(1):51–83.

[Healey and Lienard, 1993] Healey, A. J. and Lienard, D. (1993). Multivariable sliding mode control for autonomous diving and steering of unmanned underwater vehicles. *IEEE Journal of Oceanic Engineering*, 18(3):327–339.

[Henson and Zakharov, 2018] Henson, B. T. and Zakharov, Y. V. (2018). Attitude-trajectory estimation for Forward-Looking Multibeam SONAR based on acoustic image registration. *IEEE Journal of Oceanic Engineering*.

[Hermann and Krener, 1977] Hermann, R. and Krener, A. (1977). Nonlinear controllability and observability. *IEEE Transactions on Automatic Control*, 22(5):728–740.

[Hidalgo and Bräunl, 2015] Hidalgo, F. and Bräunl, T. (2015). Review of underwater SLAM techniques. In *2015 6th International Conference on Automation, Robotics and Applications (ICARA), Queenstown (NZ)*, pages 306–311. IEEE.

[Hong et al., 1996] Hong, H., Lee, J. G., Park, C. G., and Han, H. S. (1996). A leveling algorithm for an underwater vehicle using Extended Kalman Filter. In *IEEE 1998 Position Location and Navigation Symposium (Cat. No. 98CH36153), Palm Springs, CA (USA)*, pages 280–285. IEEE.

[Hover et al., 2012] Hover, F. S., Eustice, R. M., Kim, A., Englot, B., Johannsson, H., Kaess, M., and Leonard, J. J. (2012). Advanced perception, navigation and planning for autonomous in-water ship hull inspection. *The International Journal of Robotics Research*, 31(12):1445–1464.

[HT Sensor Technology CO.,LTD, 2019] HT Sensor Technology CO.,LTD (2019). Official website of HT Sensor Technology CO.,LTD:. http://www.htc-sensor.com/products/156.html. [Online; accessed April 2019].

[Huang and Kaess, 2015] Huang, T. A. and Kaess, M. (2015). Towards acoustic structure from motion for imaging SONAR. In *2015 IEEE/RSJ International Conference on Intelligent Robots and Systems (IROS), Hamburg (DE)*, pages 758–765. IEEE.

[Huang et al., 2017] Huang, Y., Zhang, Y., Wu, Z., Li, N., and Chambers, J. (2017). A novel adaptive Kalman filter with inaccurate process and measurement noise covariance matrices. *IEEE Transactions on Automatic Control*, 63(2):594–601.

[Hurtós et al., 2013a] Hurtós, N., Cufí, X., and Salvi, J. (2013a). A novel blending technique for two-dimensional Forward-Looking SONAR mosaicing. In *Proceedings of OCEANS'13 MTS/IEEE SAN DIEGO, CA (USA)*, pages 1–7. IEEE.

[Hurtós et al., 2013b] Hurtós, N., Nagappa, S., Cufí, X., Petillot, Y., and Salvi, J. (2013b). Evaluation of registration methods on two-dimensional Forward-Looking SONAR imagery. In *Proceedings of OCEANS'13 MTS/IEEE BERGEN, Bergen (NO)*, pages 1–8. IEEE.

[Hurtos et al., 2014] Hurtos, N., Palomeras, N., Carrera, A., Carreras, M., Bechlioulis, C. P., Karras, G. C., Hesmati-alamdari, S., and Kyriakopoulos, K. (2014). SONAR-based chain following using an Autonomous Underwater Vehicle. In *2014 IEEE/RSJ International Conference on Intelligent Robots and Systems (IROS), Chicago, IL (USA)*, pages 1978–1983. IEEE.

[Hurtós et al., 2015] Hurtós, N., Ribas, D., Cufí, X., Petillot, Y., and Salvi, J. (2015). Fourier-based registration for robust Forward-Looking SONAR mosaicing in low-visibility underwater environments. *Journal of Field Robotics*, 32(1):123–151.

[Hurtós Vilarnau, 2014] Hurtós Vilarnau, N. (2014). *Forward-Looking SONAR mosaicing for underwater environments*. PhD dissertation, Universitat de Girona.

[ISME, 2019] ISME (2019). Official ISME website:. www.isme.unige.it. [Online; accessed July 2019].

[Jetto et al., 1999] Jetto, L., Longhi, S., and Venturini, G. (1999). Development and experimental validation of an Adaptive Extended Kalman Filter for the localization of mobile robots. *IEEE Transactions on Robotics and Automation*, 15(2):219–229.

[Johannsson et al., 2010a] Johannsson, H., Kaess, M., Englot, B., Hover, F., and Leonard, J. (2010a). Imaging SONAR-aided navigation for autonomous underwater harbor surveillance. In *2010 IEEE/RSJ International Conference on Intelligent Robots and Systems (IROS), Taipei (TW)*, pages 4396–4403. IEEE.

[Johannsson et al., 2010b] Johannsson, H., Kaess, M., Englot, B., Hover, F., and Leonard, J. (2010b). Imaging SONAR-aided navigation for autonomous underwater harbor surveillance. In *2010 IEEE/RSJ International Conference on Intelligent Robots and Systems (IROS), Hamburg (DE)*, pages 4396–4403. IEEE.

[Julier and Uhlmann, 2004] Julier, S. J. and Uhlmann, J. K. (2004). Unscented filtering and nonlinear estimation. *Proceedings of the IEEE*, 92(3):401–422.

[Julier et al., 1995] Julier, S. J., Uhlmann, J. K., and Durrant-Whyte, H. F. (1995). A new approach for filtering nonlinear systems. In *Proceedings of 1995 American Control Conference-ACC'95, Seattle, WA (USA)*, volume 3, pages 1628–1632. IEEE.

[Kalman, 1960] Kalman, R. E. (1960). A new approach to linear filtering and prediction problems. *Journal of Basic Engineering*, 82(1):35–45.

[Karoui et al., 2015] Karoui, I., Quidu, I., and Legris, M. (2015). Automatic sea-surface obstacle detection and tracking in Forward Looking SONAR image sequences. *IEEE Transactions on Geoscience and Remote Sensing*, 53(8):4661–4669.

[Kim et al., 2016] Kim, J., Cho, H., Pyo, J., Kim, B., and Yu, S.-C. (2016). The convolution neural network based agent vehicle detection using Forward-Looking SONAR image. In *Proceedings of OCEANS'16 MTS/IEEE MONTEREY, Monterey, CA (USA)*. IEEE.

[Kim and Yu, 2016] Kim, J. and Yu, S.-C. (2016). Convolutional neural network-based real-time ROV detection using Forward-Looking SONAR image. In *2016 IEEE/OES Autonomous Underwater Vehicles (AUV), Tokyo (JP)*, pages 396–400. IEEE.

[Kim et al., 2005] Kim, K., Neretti, N., and Intrator, N. (2005). Mosaicing of acoustic camera images. *IEEE Proceedings-Radar, Sonar and Navigation*, 152(4):263–270.

[Kim et al., 2006] Kim, K., Neretti, N., and Intrator, N. (2006). Video enhancement for underwater exploration using Forward-Looking SONAR. In *International Conference on Advanced Concepts for Intelligent Vision Systems*, pages 554–563. Springer.

[Kullander, 1989] Kullander, L. (1989). Development of a terrain navigation system for AUVs. In *Proceedings of the 6th International Symposium on Unmanned Untethered Submersible Technology, Durham, (USA)*, pages 494–501. IEEE.

[Leonard and Bahr, 2016] Leonard, J. J. and Bahr, A. (2016). Autonomous Underwater Vehicle navigation. In *Springer Handbook of Ocean Engineering*, pages 341–358. Springer.

[Li et al., 2014] Li, H., Dong, Y., He, X., Xie, S., and Luo, J. (2014). A SONAR image mosaicing algorithm based on improved SIFT for USV. In *2014 IEEE International Conference on Mechatronics and Automation*, pages 1839–1843. IEEE.

[Li and Yan, 2016] Li, H. and Yan, W. (2016). Model predictive stabilization of constrained underactuated Autonomous Underwater Vehicles with guaranteed feasibility and stability. *IEEE/Asme Transactions On Mechatronics*, 22(3):1185–1194.

[Li et al., 2018] Li, J., Kaess, M., Eustice, R. M., and Johnson-Roberson, M. (2018). Pose-graph SLAM using Forward-Looking SONAR. *IEEE Robotics and Automation Letters*, 3(3):2330–2337.

[Li et al., 2007] Li, L., Qu, Z., Zeng, Q., and Meng, F. (2007). A novel approach to image roto-translation estimation. In *2007 IEEE International*

Conference on Automation and Logistics, Jinan (CHN), pages 2612–2616. IEEE.

[Li and Bar-Shalom, 1994] Li, X. R. and Bar-Shalom, Y. (1994). A recursive multiple model approach to noise identification. *IEEE Transactions on Aerospace and Electronic Systems*, 30(3):671–684.

[Liu et al., 2019] Liu, H., He, B., Feng, C., Guo, S., Yin, F., Zhang, X., Mu, X., Li, T., and Yan, T. (2019). Navigation algorithm based on PSO-BP UKF of Autonomous Underwater Vehicle. In *2019 IEEE Underwater Technology (UT), Kaohsiung, (TW)*, pages 1–4. IEEE.

[Liu et al., 2014] Liu, K.-z., Li, J., Guo, W., Zhu, P.-q., and Wang, X.-h. (2014). Navigation system of a class of underwater vehicle based on Adaptive Unscented Kalman Filter algorithm. *Journal of Central South University*, 21(2):550–557.

[Luque et al., 2009] Luque, J. C. C., Donha, D. C., and de Barros, E. A. (2009). AUV parameter identification. *IFAC Proceedings Volumes*, 42(18):72–77.

[Mahmoudi et al., 2017] Mahmoudi, Z., Poulsen, N. K., Madsen, H., and Jørgensen, J. B. (2017). Adaptive Unscented Kalman Filter using Maximum Likelihood Estimation. *IFAC-PapersOnLine*, 50(1):3859–3864.

[Mahon and Williams, 2004] Mahon, I. and Williams, S. (2004). SLAM using natural features in an underwater environment. In *ICARCV 2004 8th Control, Automation, Robotics and Vision Conference, Kunming (CHN)*, volume 3, pages 2076–2081. IEEE.

[Mallios et al., 2010] Mallios, A., Ridao, P., Ribas, D., Maurelli, F., and Petillot, Y. (2010). EKF-SLAM for AUV navigation under probabilistic SONAR scan-matching. In *2010 IEEE/RSJ International Conference on Intelligent Robots and Systems (IROS), Taipei (TW)*, pages 4404–4411. IEEE.

[Manley et al., 2018] Manley, J. E., Halpin, S., Radford, N., and Ondler, M. (2018). Aquanaut: A new tool for subsea inspection and intervention. In *Proceedings of OCEANS'18 MTS/IEEE CHARLESTON, Charleston, SC (USA)*. IEEE.

[Marco et al., 2005] Marco, D. B., Martins, A., and Healy, A. J. (2005). Surge motion parameter identification for the NPS Phoenix AUV. Technical report, Naval Postgraduate School.

[Martin and Whitcomb, 2013] Martin, S. C. and Whitcomb, L. L. (2013). Experimental identification of six-degree-of-freedom coupled dynamic plant models for underwater robot vehicles. *IEEE Journal of Oceanic Engineering*, 39(4):662–671.

[Mehra, 1972] Mehra, R. (1972). Approaches to adaptive filtering. *IEEE Transactions on Automatic Control*, 17(5):693–698.

[Mehrjouyan and Alfi, 2019] Mehrjouyan, A. and Alfi, A. (2019). Robust Adaptive Unscented Kalman Filter for bearings-only tracking in three dimensional case. *Applied Ocean Research*, 87:223–232.

[Melo and Matos, 2017] Melo, J. and Matos, A. (2017). Survey on advances on terrain based navigation for Autonomous Underwater Vehicles. *Ocean Engineering*, 139:250–264.

[Meng et al., 2000] Meng, Q.-h., Sun, Y.-c., and Cao, Z.-l. (2000). Adaptive Extended Kalman Filter (AEKF)-based mobile robot localization using SONAR. *Robotica*, 18(5):459–473.

[Miller et al., 2010] Miller, P. A., Farrell, J. A., Zhao, Y., and Djapic, V. (2010). Autonomous Underwater Vehicle navigation. *IEEE Journal of Oceanic Engineering*, 35(3):663–678.

[Mohamed and Schwarz, 1999] Mohamed, A. and Schwarz, K. (1999). Adaptive Kalman filtering for INS/GPS. *Journal of Geodesy*, 73(4):193–203.

[Negaharipour, 2012] Negaharipour, S. (2012). On 3-D scene interpretation from FS SONAR imagery. In *Proceedings of OCEANS'12 MTS/IEEE HAMPTON ROADS, Hampton Roads, VA (USA)*, pages 1–9. IEEE.

[Negahdaripour et al., 2011] Negahdaripour, S., Aykin, M., and Sinnarajah, S. (2011). Dynamic scene analysis and mosaicing of benthic habitats by FS SONAR imaging-issues and complexities. In *Proceedings of OCEANS'11 MTS/IEEE WAIKOLOA, Waikoloa, HI (USA)*. IEEE.

[Negahdaripour et al., 2005] Negahdaripour, S., Firoozfam, P., and Sabzmeydani, P. (2005). On processing and registration of Forward-Scan acoustic video imagery. In *The 2nd Canadian Conference on Computer and Robot Vision (CRV'05), Victoria, BC (CA)*, pages 452–459. IEEE.

[Newman, 2018] Newman, J. N. (2018). *Marine hydrodynamics*. MIT press.

[Nicosevici et al., 2009] Nicosevici, T., Gracias, N., Negahdaripour, S., and Garcia, R. (2009). Efficient three-dimensional scene modeling and mosaicing. *Journal of Field Robotics*, 26(10):759–788.

[Nijmeijer, 1982] Nijmeijer, H. (1982). Observability of autonomous discrete time non-linear systems: a geometric approach. *International Journal of Control*, 36(5):867–874.

[Norgren and Skjetne, 2018] Norgren, P. and Skjetne, R. (2018). A multibeam-based SLAM algorithm for iceberg mapping using AUVs. *IEEE Access*, 6.

[Nygren and Jansson, 2004] Nygren, I. and Jansson, M. (2004). Terrain navigation for underwater vehicles using the correlator method. *IEEE Journal of Oceanic Engineering*, 29(3):906–915.

[Obsharsky et al., 1969] Obsharsky, P., Schlee, F., and Toda, N. (1969). Region of Kalman filter convergence for several autonomous navigation modes. *AIAA Journal*, 7(4):622–627.

[Odelson et al., 2006] Odelson, B. J., Rajamani, M. R., and Rawlings, J. B. (2006). A new autocovariance least-squares method for estimating noise covariances. *Automatica*, 42(2):303–308.

[Ojansivu and Heikkila, 2007] Ojansivu, V. and Heikkila, J. (2007). Image registration using blur-invariant phase correlation. *IEEE Signal Processing Letters*, 14(7):449–452.

[ONO SOKKI CO.,LTD, 2019] ONO SOKKI CO.,LTD (2019). Official website of ONO SOKKI CO.,LTD:. https://www.onosokki.co.jp/English/english.htm. [Online; accessed April 2019].

[Ozog et al., 2015] Ozog, P., Troni, G., Kaess, M., Eustice, R. M., and Johnson-Roberson, M. (2015). Building 3D mosaics from an Autonomous

Underwater Vehicle, Doppler Velocity Log, and 2D imaging SONAR. In *2015 IEEE International Conference on Robotics and Automation (ICRA), Seattle, WA (USA)*, pages 1137–1143. IEEE.

[Pagliai, 2019] Pagliai, M. (2019). *Design and testing of innovative thrusters and their integration in the design of a reconfigurable underwater vehicle.* PhD dissertation, University of Florence.

[Paull et al., 2014] Paull, L., Saeedi, S., Seto, M., and Li, H. (2014). AUV navigation and localization: A review. *IEEE Journal of Oceanic Engineering*, 39(1):131–149.

[Petillot et al., 2001] Petillot, Y., Ruiz, I. T., and Lane, D. M. (2001). Underwater vehicle obstacle avoidance and path planning using a Multi-Beam Forward Looking SONAR. *IEEE Journal of Oceanic Engineering*, 26(2):240–251.

[Pettersen et al., 2018] Pettersen, K. Y., Liljebäck, P., Sørensen, A. J., Stavdahl, Ø., Lund, F., Transeth, A. A., and Gravdahl, J. T. (2018). Underwater manipulator arm robot. US Patent App. 15/546,820.

[Pfingsthorn et al., 2010] Pfingsthorn, M., Birk, A., Schwertfeger, S., Bülow, H., and Pathak, K. (2010). Maximum likelihood mapping with spectral image registration. In *2010 IEEE International Conference on Robotics and Automation*, pages 4282–4287. IEEE.

[Pivano et al., 2009] Pivano, L., Johansen, T. A., and Smogeli, Ø. N. (2009). A four-quadrant thrust estimation scheme for marine propellers: Theory and experiments. *IEEE Transactions on Control Systems Technology*, 17(1):215–226.

[Pizer et al., 1987] Pizer, S. M., Amburn, E. P., Austin, J. D., Cromartie, R., Geselowitz, A., Greer, T., ter Haar Romeny, B., Zimmerman, J. B., and Zuiderveld, K. (1987). Adaptive histogram equalization and its variations. *Computer Vision, Graphics, and Image Processing*, 39(3):355–368.

[Reddy and Chatterji, 1996] Reddy, B. S. and Chatterji, B. N. (1996). An FFT-based technique for translation, rotation, and scale-invariant image registration. *IEEE Transactions on Image Processing*, 5(8):1266–1271.

[Ribas et al., 2010] Ribas, D., Ridao, P., and Neira, J. (2010). *Underwater SLAM for structured environments using an imaging SONAR*. Springer.

[Ridolfi et al., 2020] Ridolfi, A., Franchi, M., Fanelli, F., Bianchi, M., and Allotta, B. (2020). Underwater robotics competitions: the European Robotics League Emergency Robots experience with Feelhippo AUV. *Frontiers in Robotics and AI*, 7:3.

[Ridolfi et al., 2018] Ridolfi, A., Spaccini, D., Fanelli, F., Franchi, M., Monni, N., Picari, L., Petrioli, C., and Allotta, B. (2018). An Autonomous Underwater Vehicle and SUNSET to bridge underwater networks composed of multi-vendor modems. *Annual Reviews in Control*, 46:295–303.

[Rixon Fuchs et al., 2018] Rixon Fuchs, L., Gällström, A., and Folkesson, J. (2018). Object recognition in Forward-Looking SONAR images using transfer learning. In *2018 IEEE/OES Autonomous Underwater Vehicles (AUV) Symposium, Porto (P)*.

[Rypkema et al., 2018] Rypkema, N. R., Fischell, E. M., Forrest, A. L., Benjamin, M. R., and Schmidt, H. (2018). Implementation of a hydrodynamic model-based navigation system for a low-cost AUV fleet. In *2018 IEEE/OES Autonomous Underwater Vehicle Workshop (AUV), Porto (P)*. IEEE.

[Sabet et al., 2017] Sabet, M. T., Daniali, H. M., Fathi, A., and Alizadeh, E. (2017). Identification of an Autonomous Underwater Vehicle hydrodynamic model using the Extended, Cubature, and Transformed Unscented Kalman Filter. *IEEE Journal of Oceanic Engineering*, 43(2):457–467.

[Sage and Husa, 1969] Sage, A. P. and Husa, G. W. (1969). Adaptive filtering with unknown prior statistics. In *Joint Automatic Control Conference, Boulder, CO (USA)*, number 7, pages 760–769.

[Sarkka and Nummenmaa, 2009] Sarkka, S. and Nummenmaa, A. (2009). Recursive noise adaptive Kalman filtering by variational Bayesian approximations. *IEEE Transactions on Automatic control*, 54(3):596–600.

[Shin et al., 2015] Shin, Y.-S., Lee, Y., Choi, H.-T., and Kim, A. (2015). Bundle adjustment from SONAR images and SLAM application for

seafloor mapping. In *Proceedings of OCEANS'05 MTS/IEEE WASHINGTON, Washington, DC (USA)*. IEEE.

[Smallwood and Whitcomb, 2003] Smallwood, D. A. and Whitcomb, L. L. (2003). Adaptive identification of dynamically positioned underwater robotic vehicles. *IEEE Transactions on Control Systems Technology*, 11(4):505–515.

[Song et al., 2018] Song, S., Kim, B., Kim, J., and Yu, S.-C. (2018). Real-time reliability evaluation of optical and acoustic images for feature-based localization of AUV. In *Proceedings of OCEANS'18 MTS/IEEE KOBE, Kone (JP)*, pages 1–6. IEEE.

[Sun et al., 2011] Sun, F., Hu, X., Zou, Y., and Li, S. (2011). Adaptive Unscented Kalman filtering for state of charge estimation of a Lithium-Ion battery for electric vehicles. *Energy*, 36(5):3531–3540.

[SUNRISE, 2019] SUNRISE (2019). Official website of the SUNRISE project:. www.fp7-sunrise.eu. [Online; accessed July 2019].

[Tan et al., 2014] Tan, Y. T., Gao, R., and Chitre, M. (2014). Cooperative path planning for range-only localization using a single moving beacon. *IEEE Journal of Oceanic Engineering*, 39(2):371–385.

[THESAURUS, 2019] THESAURUS (2019). Official website of the THESAURUS project:. si.isti.cnr.it/index.php/hid-project-category-list/28-project-thesaurus-page. [Online; accessed July 2019].

[Triggs et al., 1999] Triggs, B., McLauchlan, P. F., Hartley, R. I., and Fitzgibbon, A. W. (1999). Bundle adjustment-a modern synthesis. In *International Workshop on Vision Agorithms (IWVA), Corfu (GK)*, pages 298–372. Springer.

[Tzimiropoulos et al., 2010] Tzimiropoulos, G., Argyriou, V., Zafeiriou, S., and Stathaki, T. (2010). Robust FFT-based scale-invariant image registration with image gradients. *IEEE Transactions on Pattern Analysis and Machine Intelligence*, 32(10):1899–1906.

[Uhlmann, 1994] Uhlmann, J. K. (1994). Simultaneous map building and localization for real time applications. Technical report, University of Oxford, 1994. Transfer thesis.

[Valdenegro-Toro, 2016] Valdenegro-Toro, M. (2016). Object recognition in Forward-Looking SONAR images with convolutional neural networks. In *Proceedings of OCEANS'16 MTS/IEEE MONTEREY, Monterey, CA (USA)*. IEEE.

[Valdenegro-Toro, 2017] Valdenegro-Toro, M. (2017). Best practices in convolutional networks for Forward-Looking SONAR image recognition. In *Proceedings of OCEANS'16 MTS/IEEE ABERDEEN, Aberdeen (UK)*. IEEE.

[Valencia and Andrade-Cetto, 2018] Valencia, R. and Andrade-Cetto, J. (2018). *Mapping, planning and exploration with Pose SLAM*. Springer.

[Vasconcelos et al., 2011] Vasconcelos, J. F., Elkaim, G., Silvestre, C., Oliveira, P., and Cardeira, B. (2011). Geometric approach to strapdown magnetometer calibration in sensor frame. *IEEE Transactions on Aerospace and Electronic systems*, 47(2):1293–1306.

[Walter et al., 2008] Walter, M., Hover, F., and Leonard, J. (2008). SLAM for ship hull inspection using exactly sparse extended information filters. In *2008 IEEE International Conference on Robotics and Automation (ICRA), Pasadena, CA (USA)*, pages 1463–1470. IEEE.

[Walter, 2008] Walter, M. R. (2008). *Sparse Bayesian information filters for localization and mapping*. PhD dissertation, Massachusetts Institute of Technology and Woods Hole Oceanographic Institution.

[Wan and Nelson, 2001] Wan, E. A. and Nelson, A. T. (2001). Dual Extended Kalman filter methods. *Kalman Filtering and Neural Networks*, 123.

[Wan et al., 2001] Wan, E. A., Van Der Merwe, R., et al. (2001). The Unscented Kalman Filter. *Kalman filtering and Neural Networks*, 5(2007):221–280.

[Webster et al., 2013] Webster, S. E., Walls, J. M., Whitcomb, L. L., and Eustice, R. M. (2013). Decentralized Extended Information Filter for single-beacon cooperative acoustic navigation: Theory and experiments. *IEEE Transactions on Robotics*, 29(4):957–974.

[Weeks, 1996] Weeks, A. R. (1996). *Fundamentals of electronic image processing*. SPIE Optical Engineering Press Bellingham.

[Wenwu et al., 2017] Wenwu, W., Binbin, C., and Yao, C. (2017). A real-time object recognition for Forward-Looking SONAR. In *2017 2nd International Conference on Image, Vision and Computing (ICIVC), Chengdu (CHN)*, pages 58–61. IEEE.

[White et al., 2010] White, C., Hiranandani, D., Olstad, C. S., Buhagiar, K., Gambin, T., and Clark, C. M. (2010). The Malta cistern mapping project: Underwater robot mapping and localization within ancient tunnel systems. *Journal of Field Robotics*, 27(4):399–411.

[Williams et al., 2000] Williams, S. B., Newman, P., Dissanayake, G., and Durrant-Whyte, H. (2000). Autonomous underwater simultaneous localisation and map building. In *2000 IEEE International Conference on Robotics and Automation (ICRA) (Cat. No. 00CH37065), San Francisco, CA (USA)*, volume 2, pages 1793–1798. IEEE.

[Xu et al., 2013] Xu, F., Zou, Z.-J., Yin, J.-C., and Cao, J. (2013). Identification modeling of underwater vehicles' nonlinear dynamics based on support vector machines. *Ocean Engineering*, 67:68–76.

[Yan et al., 2015] Yan, W., Chen, W., and Cui, R. (2015). Moving Long BaseLine positioning algorithm with uncertain sound speed. *Journal of Mechanical Science and Technology*, 29(9):3995–4002.

[Yang and Huang, 2017] Yang, Y. and Huang, G. (2017). Acoustic-inertial underwater navigation. In *2017 IEEE International Conference on Robotics and Automation (ICRA), Singapore (SG)*, pages 4927–4933.

[Yoerger et al., 2007] Yoerger, D. R., Jakuba, M., Bradley, A. M., and Bingham, B. (2007). Techniques for deep sea near bottom survey using an Autonomous Underwater Vehicle. *The International Journal of Robotics Research*, 26(1):41–54.

[Zagrobelny and Rawlings, 2015] Zagrobelny, M. A. and Rawlings, J. B. (2015). Identifying the uncertainty structure using Maximum Likelihood Estimation. In *2015 American Control Conference (ACC), Chicago, IL (USA)*, pages 422–427. IEEE.

[Zhang et al., 2016] Zhang, J., Sohel, F., Bian, H., Bennamoun, M., and An, S. (2016). Forward-Looking SONAR image registration using polar transform. In *Proceedings of OCEANS'16 MTS/IEEE MONTEREY, Monterey, CA (USA)*. IEEE.

[Zheng et al., 2018] Zheng, B., Fu, P., Li, B., and Yuan, X. (2018). A robust Adaptive Unscented Kalman Filter for nonlinear estimation with uncertain noise covariance. *Sensors*, 18(3):808.

[Zhou et al., 2010] Zhou, J., Knedlik, S., and Loffeld, O. (2010). INS/GPS tightly-coupled integration using Adaptive Unscented Particle Filter. *The Journal of Navigation*, 63(3):491–511.

[Zhu et al., 2009] Zhu, H., Hu, H., and Gui, W. (2009). Adaptive Unscented Kalman Filter for deep-sea tracked vehicle localization. In *2009 International Conference on Information and Automation*, pages 1056–1061. IEEE.

[Ziani-Cherif et al., 1997] Ziani-Cherif, S., Lebret, G., and Perrier, M. (1997). Identification and control of a submarine vehicle. *IFAC Proceedings Volumes*, 30(20):307–312.